CHEMICAL AND STRUCTURAL CHARACTERIZATION OF SELENIUM-INCORPORATED HYDROXYAPATITE

A THESIS SUBMITTED TO
THE GRADUATE SCHOOL OF NATURAL AND APPLIED SCIENCES
OF
MIDDLE EAST TECHNICAL UNIVERSITY

BY

BARIŞ ALKAN

IN PARTIAL FULFILLMENT OF THE REQUIREMENTS
FOR
THE DEGREE OF MASTER OF SCIENCE
IN
METALLURGICAL AND MATERIALS ENGINEERING

JULY 2015

Approval of the Thesis:

CHEMICAL AND STRUCTURAL CHARACTERIZATION OF SELENIUM-INCORPORATED HYDROXYAPATITE

submitted by **BARIŞ ALKAN** in partial fulfillment of the requirements for the degree of **Master of Science in Metallurgical and Materials Engineering Department, Middle East Technical University** by,

Prof. Dr. Gülbin Dural Ünver ________________
Dean, Graduate School **of Natural and Applied Sciences**

Prof. Dr. C. Hakan Gür ________________
Head of Department, **Metallurgical and Materials Eng.**
Prof. Dr. Caner Durucan ________________
Supervisor, **Metallurgical and Materials Eng. Dept., METU**

Examining Committee Members:

Assoc. Prof. Dr. Arcan Dericioğlu ________________
Metallurgical and Materials Eng. Dept., METU

Prof. Dr. Caner Durucan ________________
Metallurgical and Materials Eng. Dept., METU

Assoc. Prof. Dr. Y. Eren Kalay ________________
Metallurgical and Materials Eng. Dept., METU

Assoc. Prof. Dr. H. Emrah Ünalan ________________
Metallurgical and Materials Eng. Dept., METU

Assoc. Prof. Dr. Ziya Esen ________________
Materials Science and Eng. Dept., Çankaya University

Date: 21/07/2015

I hereby declare that all information in this document has been obtained and presented in accordance with academic rules and ethical conduct. I also declare that, as required by these rules and conduct, I have fully cited and referenced all material and results that are not original to this work.

Name, Lastname : Barış ALKAN

Signature :

ABSTRACT

CHEMICAL AND STRUCTURAL CHARACTERIZATION OF SELENIUM-INCORPORATED HYDROXYAPATITE

Alkan, Barış
M. S., Metallurgical and Materials Engineering
Supervisor: Prof. Dr. Caner Durucan

July 2015, 82 pages

In case of severe bone damage or fracture, synthetic bone grafts have long been applied for replacing natural bone tissue. Recent advances in this area have led to development of dual-functional synthetic hard tissue analogs exhibiting high biocompability/osteoconductivity together with therapeutic effect. Metallic ions are promising therapeutic agents in treatment of bone tumors due to their high physiological stability and availability compared to other alternative therapeutic agents such as recombinant proteins, therapeutic nucleic acids and anti-cancer drugs. Selenium, in that respect, is effective therapeutic agent with promising anti-oxidant and anti-carcinogenic effect when used in proper doses. In this study, selenium-incorporated hydroxyapatite (HAp:Se) particles have been synthesized by modified aqueous precipitation method using calcium ($Ca(NO_3)_2 \cdot 4H_2O$) and phosphate ($(NH_4)_2HPO_4$) salts with sodium selenite (Na_2SeO_3). The effect of Se incorporation in different amounts on the physical, chemical properties and crystal structure of resultant HAp powders have been explored. Complete chemical identification was performed with spectroscopical chemical analyses including Fourier transform infrared and x-ray photoelectron spectroscopy to elucidate the mechanism and chemical nature of Se incorporation in HAp. Meanwhile, transmission electron microscopy and x-ray diffraction studies by Rietveld refinement have conducted to explain changes in the HAp crystallite and crystal structure upon Se incorporation. The results indicate that well-incorporated selenite ions in HAp mostly accommodate near very top surface of HAp (1-2 nm). Also, position of Se ions in HAp crystal structure were estimated to be inside phosphate tetrahedral with limited extend of Se ions. B-type carbonation (3-5 wt. %), nanocrystalline structure and low crystalline surface of HAp:Se particles are believed to lead to high biocompatibility and increased solubility of these particles. Also, anti-cancer effect of Se ion incorporates in HAp nanoparticles are associated with two-step release of Se ionic species; first surface release of them in high extents and subsequently release from HAp:Se crystallites in low extends; therefore, initial release kinetics of Se ions are believed to be critical in biological tests.

Key words: Bone graft, Therapeutic agent, Metallic ion, Selenium

ÖZ

SELENYUM KATKILANMIŞ HİDROKSİAPATİTİN KİMYASAL VE YAPISAL KARAKTERIZASYONU

Alkan, Barış
Yüksek Lisans, Metalurji ve Malzeme Mühendiliği Bölümü
Tez Yöneticisi: Prof. Dr. Caner Durucan

Temmuz 2015, 82 sayfa

Kemikteki ciddi derecede hasar ve kırılmalarda, doğal kemik dokusunun yerini alabilecek sentetik kemik greftleri uzun süredir uygulanmaktadır. Bu alandaki son ilerlemeler, sentetik sert doku analoglarının yüksek biyolojik uyumluğu dışında, tedavi edici ve iyileştirici özellikler kazandırılmasını öngörmektedir. Özellikle, yüksek fizyolojik dengesi, kolay bulunabilirliği ve düşük maliyetinden dolayı metal iyonları, rekombinant protein, iyileştirici nükleik asitler ve kansere karşı geliştirilen ilaçlar gibi tedavi edici ajanlara göre alternatif bir ajan olarak düşünülmektedir. Bu anlamda, uygun dozlarda kullanıldığında gösterdiği başarılı antioksidan ve antikanser etkisinden dolayı selenyum iyonu tedavi edici bir metal ajan olarak kullanılabileceği öngörülmektedir. Bu çalışmada, Se iyonları hidroksiapatit (HAp) parçacıklarına uygun kalsiyum ($Ca(NO_3)_2{\cdot}4H_2O$), fosfat ($(NH_4)_2HPO_4$) ve selenit (Na_2SeO_3) tuzları kullanılarak sulu çökeltme yöntemiyle katkılanmıştır. Farklı miktarlardaki Se katkısının HAp parçacıklarının kimyasal, fiziksel ve yapısal özelliklerine etkisi araştırılmıştır. Parçacıklar kimyasal analizi enerji yayılım speckrosposi, kızıl ötesi spektroskopisi ve x-ışını fotoelektron spektroskopisi kullanılarak tamamlanmıştır. Yüksek çözünürlüklü geçirimli elektron mikroskopisinde elde edilen parçaçık morfolojisi temel alınarak Se katkılanmış HAp parçacıklarının yapısal analizi, X-ışını kırınım analizi ve Rietveld yöntemiyle çalışılmıştır. Elde edilen kimyasal sonuçlara göre, Se iyonu HAp parçacıklarına büyük ölçüde katkılandığı görülmüş ve özellikle

HAp nanoparçacıklarının yüzeyinde önemli oranda selenit iyonu tespit edilmiştir. Bunun yanısıra, Se iyonlarının HAp kristal yapısı içinde fosfat dörtyüzlüsünde içerisinde yer aldığı düşünülmektedir. Elde edilen sonuçlara göre B tipi karbonat iyonuna sahip olması, nanoboyutlardaki kristal yapısı ve düşük kristalliğe sahip bir yüzeyinin bulunması, Se katkılanmış HAp parçacıklarının yüksek biyouyumluluğa ve artan çözünebilirlik değerleri göstereceğine dair bulgulardır. Ayrıca Se iyonunun yüzeydeki yüksek konsantrasyonu ve HAp kristali içerisindeki görece düşük konsantrasyonu, bu iyonun HAp parçacıklarında salınım davranışı aydınlatıcı olduğu düşünülmektedir.

Anahtar Kelimeler: Biyoseramikler, Hidroksiapatit, Selenyum, Nanokristaller.

To my family

ACKNOWLEDGEMENTS

I would like to express my sincere appreciation to Prof. Dr. Caner Durucan for his supervision, guidance and support throughout the study and providing excellent laboratory facilities.

I am grateful to Assoc. Prof. Y. Eren Kalay for his contributions on Rietveld refinement method and encouragement in the progress of this study. I would also like to thank Prof. Gilberto Artioli and Marco Sommariva for their invaluable crystallographic trainings within PANalytical Open Lab Turkey. I am indebted to Prof. Yuri Dekhtyar to establish a good collaboration environment with the other researchers and for his contribution on the publishment of my first article. I also count myself very lucky to have relationship with Dr. Şafak Doğu for his professional support and guidance and friendship throughout my master's education.

In the context of this thesis, I particularly want to thank to Mustafacan Kutsal for providing very useful synchrotron data, and to Serkan Yılmaz for both teaching electron microscopy techniques as well as providing TEM image data. Also, I want to thank to İlker Yıldız for his contribution on obtaining XPS data.

I am surely grateful to all my colleges in the lab; Onur Rauf Bingöl, Dr. Özlem Yıldırım, Merve Güldiken, Gözde Alkan and B. Ekim Saraç as well as the ones out of lab; Dr. Mehmet Yıldırım, M. Buğra Açan, M. Hazar Şeren and all other distinguished people in the department of Metallurgical and Materials Engineering.

I sincerely want to dedicate this thesis to my dear family for their unlimited support and unconditional love.

TABLE OF CONTENT

LIST OF TABLES

TABLES

LIST OF FIGURES

FIGURES

CHAPTER 1

INTRODUCTION AND LITERATURE REVIEW

1.1 General introduction and rationale of the thesis

Bioceramics are one of the most important classes of biomaterials used for treatment of natural bone fractures and traumas. They have been long applied as hard tissue analogs for repairing bone fractures by synthetic grafts or implants, filling the bone defects and recently used for promoting bone regeneration. Main motivation for utilizing these materials in biomedical applications is that they are highly biocompatible with natural bone and can be physiologically stable in biological environment when their cell response, surface and interfacial characteristics are properly controlled by chemical, mechanical and structural properties of synthetic substitutes. Thus, important consideration about designing and preparing these materials are basically associated with their material characteristics.

Among different bioceramics, calcium orthophosphates (CPs) have been widely used as bone analogs due to their chemical and structural similarity to mineral component in natural bone and teeth. Specifically, natural bone mineral or apatite has nanocrystalline hydroxyapatite structure ($Ca_{10}(PO_4)_6(OH)_2$, HAp) with small deficiency in calcium while different ionic species can be incorporated in its hexagonal structure. Thus, relating to natural apatite structure, two critical aspects, namely the small amount of incorporated ionic species and nanocrystalline structure of the apatites, have been commonly considered to enhance biomimicry of bone analogs and to alter the bone formation and resorption as well as surface interactions with bone cells.

Calcium orthophosphates have been recently incorporated with the metallic ions for promoting bone formation and stimulating therapeutic performance against bone cancerous cells and formation of biofilms. It is known that different ion incorporations can alter cell regulation and signaling; however, metallic ion-substituted systems are able to exhibit therapeutic effects when contained in proper doses not leading to any toxicity to surrounding cells. The ionic species of selenium, in respect, are promising since they are the constitutes of selenoproteins which are essential to human immune systems with their antioxidant function, catalyst role in producing active thyroid hormone and cell proliferation. Therefore, different inorganic selenium species have been lately employed in anticancer orthopedic applications including the coating of elemental selenium on titanium surfaces, use of nanostructured selenium compacts, selenite substituted HAp powders. Structural modifications during the processing of selenium coatings and the synthesis of Se incorporated powders appreciably affect biological response of cells, thereby emphasizing a detailed analysis of structural properties of such analogs.

In this thesis, selenium-incorporated HAp particles have been synthesized by the aqueous precipitation, the most widely used technique for preparation of HAp particles. Although there are several reports on determination of ion exchange mechanism in HAp and investigations on structural parameters in HAp lattice due to selenium substitution, there is not any through and in-depth chemical and structural analyses, elucidating the changes in HAp crystal structure upon Se incorporation. Thus, in this study, a complete structural refinement has performed both using analytical data and computational tools and approach. These findings may provide insights in establishing a link between selenium regulated anti-cancerous cell response and structural properties of HAp achieved with varying extent and amount of selenium incorporation.

1.2 Background and literature review

1.2.1 Composition and structure of natural bone

Bone is a hierarchically organized tissue that function as a lever connected to one another by movable joints in the skeletal system so that load carrying and transmission is maintained through its structure[1,2]. It contains both living and non-living components. Living components are osteoblast (bone-growing cells), osteoclast (bone resorbing cells) and the mature bone cells (osteocytes) while the non-living inorganic and organics components consisted mostly include hydroxyapatite, collagen type I, water and muco-polysaccharides[1]. Overall composition of non-living part forms about 98 wt % of total weight that includes 69 wt % of calcium phosphate mineral, 20 wt % of collagen type-I and 9 wt % of water[2].

Figure 1-1 shows hierarchical components of bone from level 7 (macroscopic scale) to level 1 (nanoscopic scale). Recently, the microscale investigation of Weiner et al.[3], has shown that there are two distinct constitutes in human lamellar bone and termed as ordered and disordered materials. Ordered materials forms majority of the lamellar bone and mainly represents mineralized collagen fibrils in the form of ordered arrays with associated macromolecules. In contrast, disorder materials are in minor amounts and mostly composed of disorientated collagen fibrils including the mineralized crystals inside or between. Remaining part of disordered materials is made of non-collagenous proteins as well as small amount of water[3].

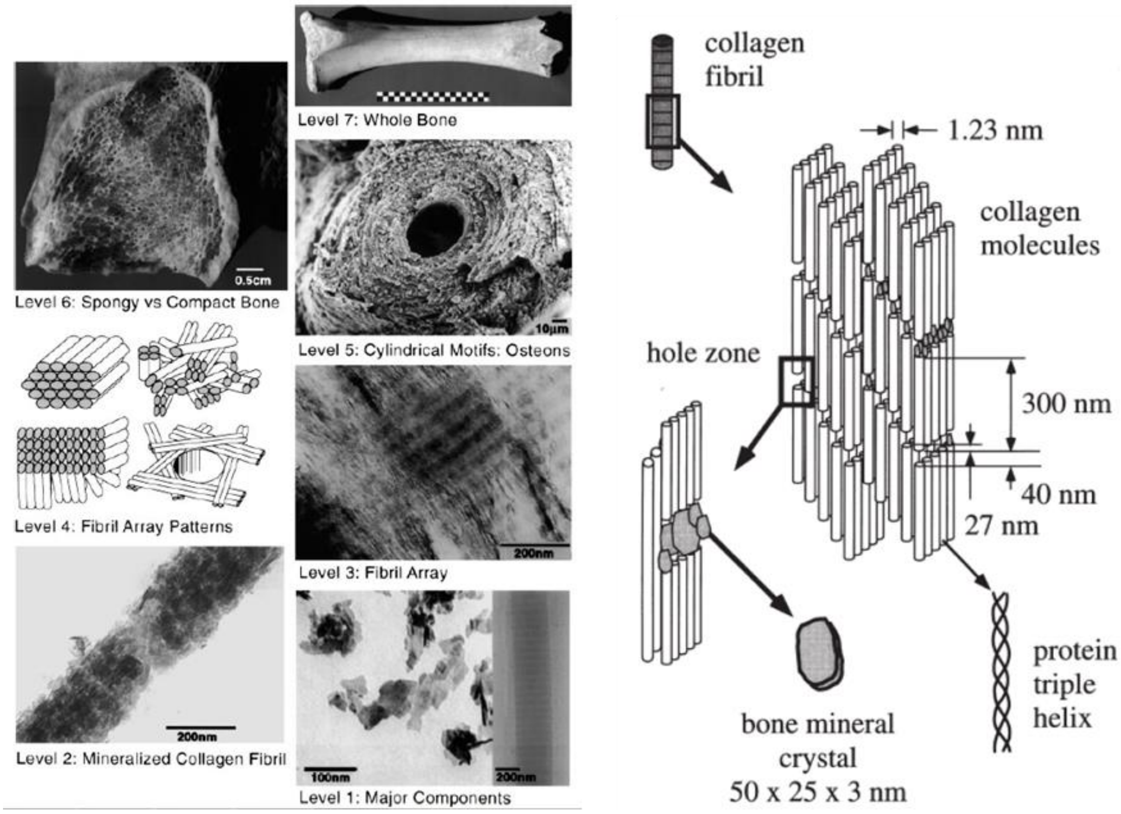

Figure 1-1 Schematic view of hierarchic components of bone from macroscopic regime to nanoscopic regime (left) and nanoscale structure of bone (right)[4,5].

Organic part of natural bone and its extracellular matrix are largely formed by collagen type-I (90 %), that is very crucial protein abundantly present in the human body[6,7]. At molecular level, structure of collagen type-I are formed by the assembly of collagen triple helices which has unique fibril structure repeating in 67 nm[5]. Representative illustration of collagen molecules with their dimensions is given in Figure 1-1. Such structures of collagen molecules basically allow the spaces between the fibrils where mineralization can consistently occur by surrounding biological fuilds[6]. In fact, there are minor amounts of non-collagenous proteins in the bone matrix and bonded to structural proteins of collagen type-I[7]. These proteins, such as proteoglycans and glycoproteins molecules, are also considered to trigger the nucleation of bone mineral[7].

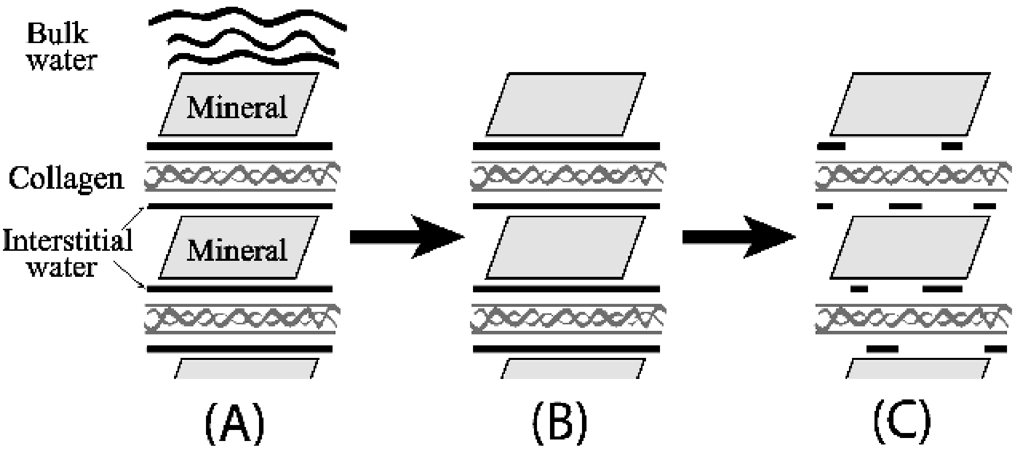

Figure 1-2 Schematic models showing position of hydrated water and its dehydration in bone with temperature[8].

Water is another important constituent of bone and mainly present in the surface of bone mineral. Wilson et al.[8] show that the closest water layer near surface of bone mineral is structured and can be protective against the mechanical deformations between bone mineral and collagen fibrils. Under high stress conditions, mobility of this water between collagen and mineral layers provides structural stability of bone. The movement of this water can also diminish deformation of collagen fibrils under uniaxial stresses[9]. In addition, the interactions between collagen fibrils and mineral phase are more likely mediated through water molecules. Representative view of the structured water (interstitial water) layers between collagen and mineral are indicated in Figure 1-2.

Mineral part of natural bone is comprised of hydroxyapatite crystals (HAp), the shape of which are plate-like with the average dimension of 50 nm in long, 25 nm in width and 1.5-4 nm in thickness[3,4]. Arrangement of these crystals within collagen fibrils basically forms the composite structure of bone that gives superior properties such as high toughness and lightweight[10]. Also, these crystals are the ion reservoir of bone and responsible for the regulation of numerous physiological functions as well as biochemical interactions[10].

Table 1-1 Bone mineral composition[10–12]

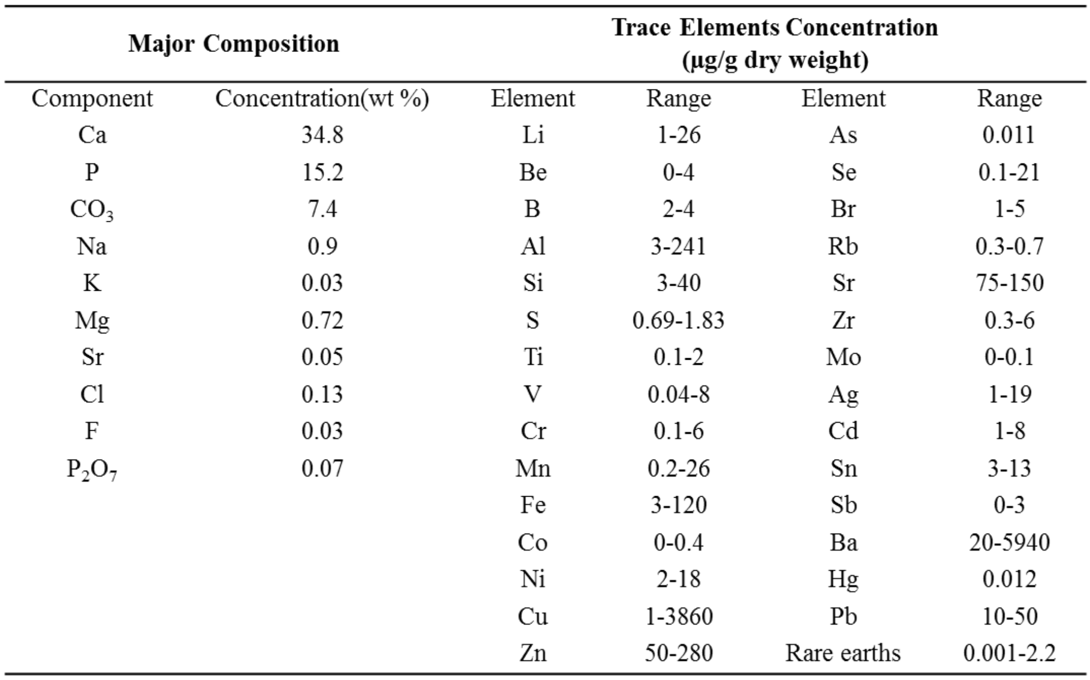

Major Composition		**Trace Elements Concentration (µg/g dry weight)**			
Component	Concentration(wt %)	Element	Range	Element	Range
Ca	34.8	Li	1-26	As	0.011
P	15.2	Be	0-4	Se	0.1-21
CO_3	7.4	B	2-4	Br	1-5
Na	0.9	Al	3-241	Rb	0.3-0.7
K	0.03	Si	3-40	Sr	75-150
Mg	0.72	S	0.69-1.83	Zr	0.3-6
Sr	0.05	Ti	0.1-2	Mo	0-0.1
Cl	0.13	V	0.04-8	Ag	1-19
F	0.03	Cr	0.1-6	Cd	1-8
P_2O_7	0.07	Mn	0.2-26	Sn	3-13
		Fe	3-120	Sb	0-3
		Co	0-0.4	Ba	20-5940
		Ni	2-18	Hg	0.012
		Cu	1-3860	Pb	10-50
		Zn	50-280	Rare earths	0.001-2.2

Although chemical formulation of bone mineral is commonly associated with stoichiometric form of HAp ($Ca_{10}(PO_4)_6(OH)_2$), presence of trace ions as well as the carbonate content modifies the formula to a more common form as $(Ca,X)_{10}(PO_4, CO_3,Y)_6(OH,Z)_2$ where X represents the cationic substitutions while Y and Z represent the anionic substitutions[10,13]. The approximate concentrations of related ionic compositions are shown in Table 1-1. Especially, the carbonate content of HAp in bone mineral is important as it enhances the reactivity of the mineral by distorting the structural order of the apatite crystals[14]. Roughly half of these carbonate ions is found near PO_4 position while other half locates at HAp crystal surfaces[15]. In addition, even though the concentration of trace ions is about 2 wt % of bone mineral, their effect on biochemical reactions and bone metabolism can be very critical[10]. As bone mineral is mainly composed of Ca and PO_4 ions, calcium phosphates compounds-based materials obtained by synthetic methods are widely studied and basic characteristics of them are presented in the next part.

1.2.2 Calcium phosphate bioceramics

Chemical and structural similarity of calcium phosphate bioceramics to natural bone mineral is the major motivation on large amount of studies in this field[16]. With these similarities, calcium phosphates are known to be non-toxic, biocompatible and bioactive (developing a direct, adherent and strong bonding with bone) when interacting with bone tissues[17]. However, due to the inherent properties of being low mechanical properties such as low fatigue resistance and high brittleness, they are mostly restricted to non-load bearing operations[18–21]. Therefore, synthetic calcium phosphate in the forms of particle, granule and scaffolds are mainly used as filling materials for bone cavities[22–24]. Coatings of calcium phosphate on dental implants and metallic prosthesis have been also commonly used[19,23].

Calcium phosphates have different characteristics according to their Ca/P molar ratio and some of their properties are summarized in Table 1-2. The solubility values are basically related to *in vivo* (in living environment) performance of the calcium phosphates while pH stability represents the long-term use of them[25]. Among the present calcium phosphates, those having Ca/P ratio in the range of 1-1.67 are only utilized for long-standing bone replacement material. The remaining calcium phosphates in Table 1-2 are not proper for implantation into body due to their high acidity and solubility (for Ca/P less than 1) and high basicity (for Ca/P higher than 1.67)[26]. Considering all species of calcium phosphates, HAp and CDHAp are the most suitable and used calcium phosphates for bone-related biomedical applications.

Table 1-2 Calcium phosphates and their physical/chemical properties[17].

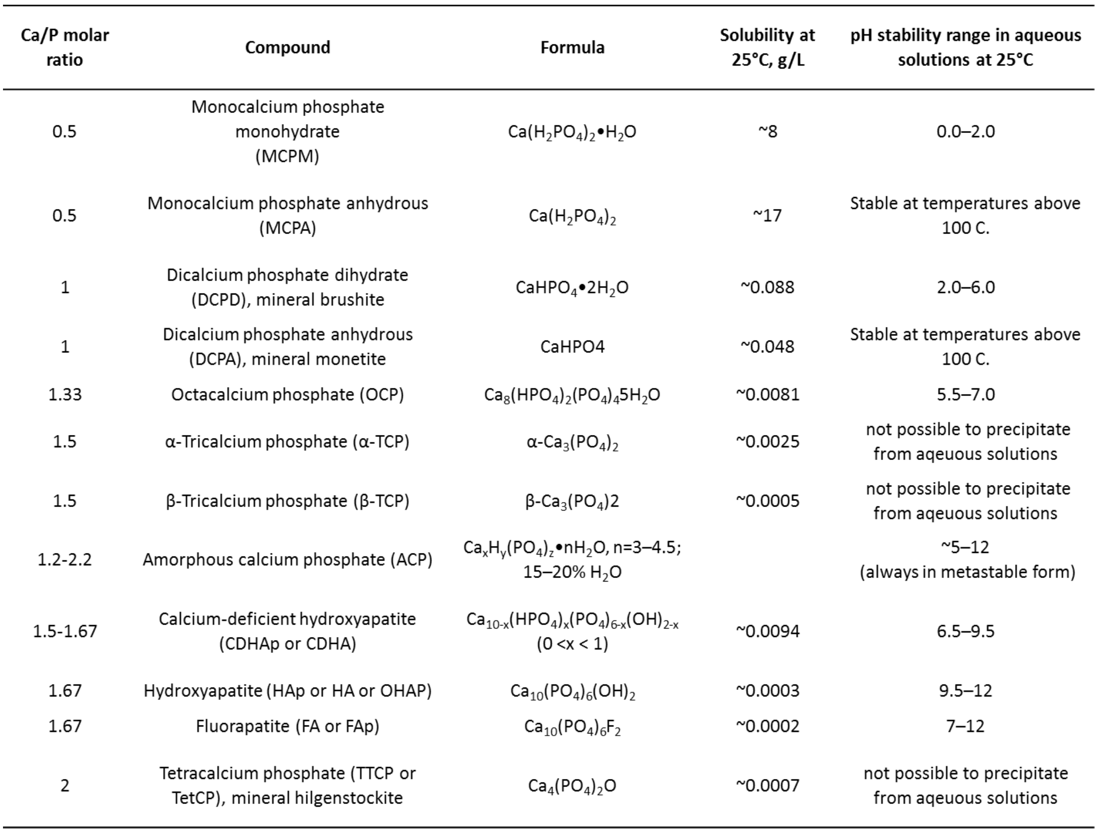

Ca/P molar ratio	Compound	Formula	Solubility at 25°C, g/L	pH stability range in aqueous solutions at 25°C
0.5	Monocalcium phosphate monohydrate (MCPM)	Ca(H$_2$PO$_4$)$_2$•H$_2$O	~8	0.0–2.0
0.5	Monocalcium phosphate anhydrous (MCPA)	Ca(H$_2$PO$_4$)$_2$	~17	Stable at temperatures above 100 C.
1	Dicalcium phosphate dihydrate (DCPD), mineral brushite	CaHPO$_4$•2H$_2$O	~0.088	2.0–6.0
1	Dicalcium phosphate anhydrous (DCPA), mineral monetite	CaHPO4	~0.048	Stable at temperatures above 100 C.
1.33	Octacalcium phosphate (OCP)	Ca$_8$(HPO$_4$)$_2$(PO$_4$)$_4$5H$_2$O	~0.0081	5.5–7.0
1.5	α-Tricalcium phosphate (α-TCP)	α-Ca$_3$(PO$_4$)$_2$	~0.0025	not possible to precipitate from aqeuous solutions
1.5	β-Tricalcium phosphate (β-TCP)	β-Ca$_3$(PO$_4$)2	~0.0005	not possible to precipitate from aqeuous solutions
1.2-2.2	Amorphous calcium phosphate (ACP)	Ca$_x$H$_y$(PO$_4$)$_z$•nH$_2$O, n=3–4.5; 15–20% H$_2$O		~5–12 (always in metastable form)
1.5-1.67	Calcium-deficient hydroxyapatite (CDHAp or CDHA)	Ca$_{10-x}$(HPO$_4$)$_x$(PO$_4$)$_{6-x}$(OH)$_{2-x}$ (0 <x < 1)	~0.0094	6.5–9.5
1.67	Hydroxyapatite (HAp or HA or OHAP)	Ca$_{10}$(PO$_4$)$_6$(OH)$_2$	~0.0003	9.5–12
1.67	Fluorapatite (FA or FAp)	Ca$_{10}$(PO$_4$)$_6$F$_2$	~0.0002	7–12
2	Tetracalcium phosphate (TTCP or TetCP), mineral hilgenstockite	Ca$_4$(PO$_4$)$_2$O	~0.0007	not possible to precipitate from aqeuous solutions

1.2.2.1 Hydroxyapatite

HAp has been long regarded as a gold standard bioceramic of reference among calcium phosphates and in 1980s the commercialization of its applications in dental and surgical field has began[17]. Owing to its similarity to bone mineral, HAp has been mostly utilized as coatings on orthopaedic and dental implant as well as in liquid chromatography of nucleic acids, proteins and various biological compounds. In addition, it is used as a polishing agent in some of the tooth pastes[24].

HAp is basically prepared by solid-state reactions and wet chemical techniques. Solid-state synthesis of pure HAp involves use of other calcium phosphates and reactions of them at temperatures greater than 1200°C[24]. Stoichiometric, high crystalline and homogenous HAp can be produced by this way. The main disadvantages of solidsstate reactions are that the obtained HAp do not well resemble to bone mineral in terms of size and shape of the crystals and high temperatures are needed for this reactions[27]. In wet methods, HAp is generally produced by the precipitation, hydrothermal, sol-gel and emulsion methods as well as hydrolysis of other calcium phosphates[24]. The obtained HAp is more likely to be Ca-deficient and in non-stoichiometric form and resemble to structure of calcium-deficient HAp (CDHAp)[24].

In early 1990's, the synthesis of nano-structured HAp ceramics had been stated. Compared to micron-sized HAp, nano-sized HAp and its role in the composite structures are found to lead to significant improvement in bioactivity and biocompatibility as well as enhancement in mineralization. These features of nano-structured HAp are mainly attributed to increased surface area, roughness and enhanced volume fraction of crystallite boundaries [28,29]. Essentially, nano-dimensional Ca-deficient HAp particles synthesized by wet methods are considered to have more similar physico-chemical characteristics to bone mineral structure. Poorly crystalline nature of these particles have high solubility, bioresorbability *in vivo* and ability to mature in extracellular matrix of bone mineral[29,30]. Therefore, structural and chemical aspects of these structures have been explored extensively.

1.2.3 Crystal structure of HAp

Stoichiometric and pure HAp has monoclinic structure with space group of $P2_1/b$ and with lattice parameters a=9.422(3)Å, b=2a, c=6.880(3)Å, γ=120°[31]. However, hydroxyapatite mostly deviates from its stoichiometry due to incorporated impurity ions that leads to transition of monoclinic structure to hexagonal structure having space groups of $P6_3/m$ with the similar lattice parameters[32]. Even if no impurity is present in HAp structure, this transition spontaneously occurs at the temperatures higher than 250°C[33]. The representative scheme of hexagonal crystal structure of stoichiometric HAp is given in Figure 1-3. In the apatite structure, there are two different sites of Ca atoms, usually termed as Ca(I) and Ca(II). In the unit cell, six Ca atoms in Ca(II) site are present and form staggered triangular structures along the c-axis while four Ca atoms in Ca(I) site locate in a column along z direction parallel to c-axis with a displacement of 0.01 Å. PO_4 tetrahedra locate between these Ca(I) sites linking the columns of Ca(I) ions[34]. The related scheme is demonstrated in Figure 1-4. Also, OH^- ions accommodate directly on c-axis and arrangements of these ions mostly depend on the presence of impurity atom on c-axis. That means there are basically two arrangements of columnar OH^- ions; namely disordered and ordered columns. Disordered columns of OH^- ions refer to the change of ordering in each column separated by the reversal point in c-axis mostly due to presence of impurity atoms such as F^- ions. The ordered model, however, has the same ordering in all OH columns and lose mirror symmetry in hexagonal structure thereby leading to monoclinic structure of HAp in the absence of impurity atoms[31].

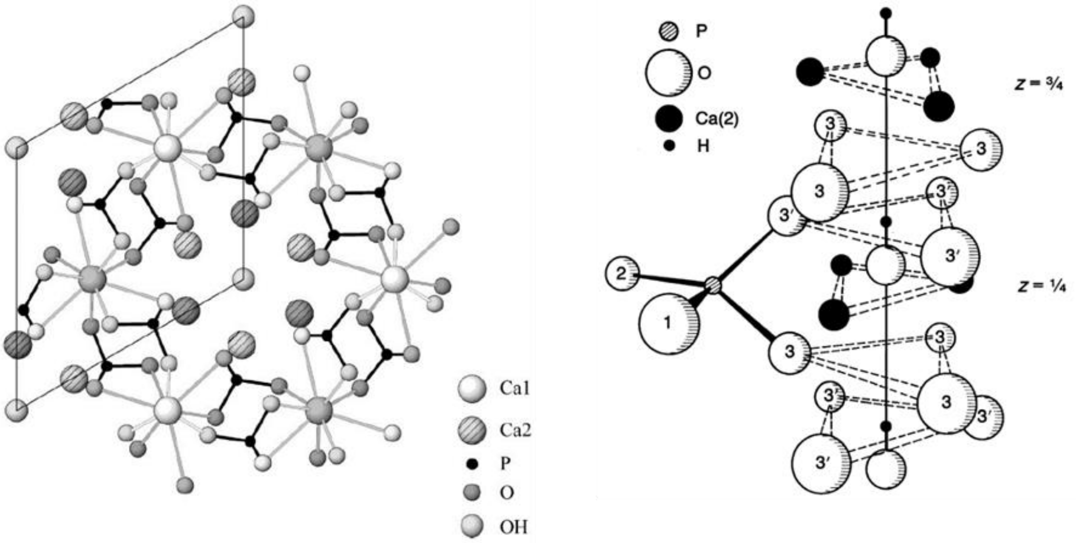

Figure 1-3 Crystal structure of HAp showing projection of (0001) plane (left) and arrangement of the ions around the c-axis (right) in HAp[34,35].

In hydroxyapatite structure, there are two octahedral holes at 0,0,0; $0,0,{}^{1}/_{2}$ on c-axis at and four octahedral holes at ${}^{1}/_{3},{}^{2}/_{3},0;{}^{1}/_{3},{}^{2}/_{3},{}^{1}/_{2};{}^{2}/_{3},{}^{1}/_{3},0$ and ${}^{2}/_{3},{}^{1}/_{3},{}^{1}/_{2}$ between the positions of Ca(I) ions. These holes mainly allows the incorporation of various ions depending on their ionic size. The large ions, like Br^- ions, mainly incorporate into first two positions on c-axis while the other intermediate sized atoms mostly likely accommodate to the octahedral holes between Ca(I)[34].

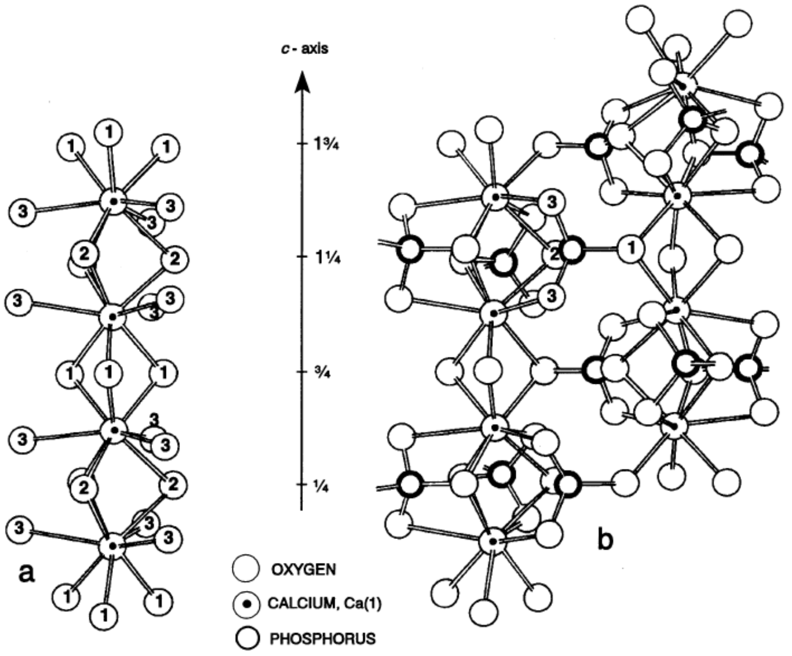

Figure 1-4 (a) Oxygen coordination of columnar Ca(1) ions in apatite. (b) linking of columns via PO_4 tetrahedra. The oxygen atoms in (a) and in one tetrahedron in (b) have been numbered, and positions of the horizontal mirror planes at ¼, ¾ etc. marked on the c-axis[34].

1.2.3.1 A-type and B-type carbonation

HAp is usually in Ca-deficient and carbonated form when synthesized by dry and wet methods, especially for the latter. However, these structures, especially in nanocrsytalline form, are better prototypes for bone mineral compared to stoichiometric HAp; thus, great attention is given to the carbonation mechanism as it can importantly change dissolution behaviour of HAp[31].

There are basically two types of carbonation in HAp structure termed as A-type and B-type. A-type carbonation is attributed to accommodation of carbonate ions in OH channels while B-type carbonate accommodate near the sloping face of phosphate tetrahedra. Fleet et al.[36] has recently investigated that A-type carbonation is consisted of open and closed configuration of carbonate ions in OH channel, the former called A2-type and the latter called A1-type. Structure solution of A1-type carbonate suggest that it either has a new space group, $P\overline{3}$, in the OH channel or obey space group of Pb in monoclinic structure[37–39]. Its orientation is given in Figure 1-5. Type A2 carbonation is mostly related to high temperature and pressure synthesis of carbonated HAp by dry methods and formed by the transformation of A1-type carbonates [36].

Arrangement of B-type carbonate ions has been long studied and recent findings confirm that carbonate atoms locate just near sloping face of phosphate tetrahedra. Elliott et al.[34] show that increasing content of B-type carbonate leads to systematic decrease in bond length of P-O3 in phosphate tetrahedra as well as reduced occupancy of P and O(3) atoms. Ivanova et al.[35] also show that incorporation of B-type carbonate ions lead to vacancy in calcium atoms in Ca(I) sites for charge neutrality. The content of B-type carbonation is known to be in between 10-14 wt. % for Na-free carbonate HAp[40]. The model of its triangular structure is shown in Figure 1-5.

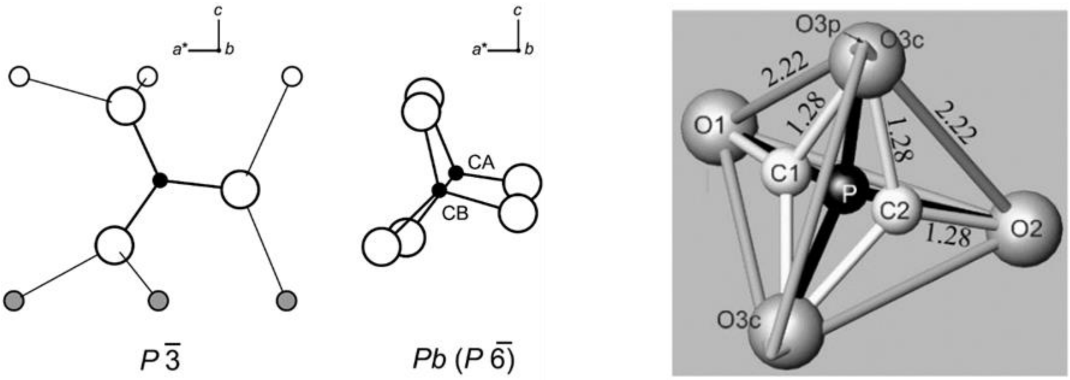

Figure 1-5 Orientation of channel carbonate in in $P\bar{3}$ A-type carbonated HAp and monoclinic *Pb* structure(the models in the left and middle) [37–39], and orientation of B-type carbonate in the sloping faces of phosphate tetrahedradel(models in the right)[35].

1.2.3.2 Surface chemistry and structure of HAp crystals

Surface properties of HAp are critical for the interaction of synthetic bone substitutes with extracellular matrix as well as *in vivo* performance of them in biological fluids[41]. These properties mostly depend on the adsorbed functional groups and distribution of charges that are predominantly determined by so-called potential determining ions, namely lattice Ca^{2+} and PO_4^{3-} ions and their interaction with body fluids[42]. Dry synthesis and solid state reactions of HAp can be useful to obtain pure HAp with minor amount of surface adsorbed ions as the most of them are thermally decomposed and removed from HAp at high temperatures. However, synthesis by wet methods, especially by the precipitation, are problematic as the solution condition such as pH, temperature and concentration, widely change the surface charge and morphology of HAp particles[42,43]. Therefore, particular interest is given to the precipitated HAp structures.

Surface of HAp particles synthesized by the precipitation is CDHAp and usually include hydrogen phosphates, hydrated and adsorbed waters on the crystal surface. Elliott et al.[44] showed that 2 % of total phosphate ions are in the form of hydrogen phosphate and locate on the surface of HAp crystal which has surface area of 37±1 m^2/g. Type of these surface phosphate groups are largely dependent on pH and lead to increase the negative charge on HAp surfaces thereby enhancing cell adhesion and growth of bone-like HAp[41]. Recently, it has been shown by Harding et al.[45] that point of zero charge (PSZ) is at a pH about 7.3 and HAp surface is positively charged above PSZ and negatively charged below it. This study further indicated that the adsorption of hydrogen phosphates to Ca^{2+} ions are the main mechanism under physiological conditions, whereas, in pure water, desorption of Ca ions trigger the presence of underlying hydrogen phosphate on HAp surface[45].

Additionally, Barrios showed the interaction of hydrated water molecules with HAp surface considering the most probable binding surfaces of $(01\bar{1}0)$ and (0001). The computational studies show that hydrated water mostly bind to Ca ions on $(01\bar{1}0)$ surface and exchange with surface OH ions thereby stabilizing this surface[46]. The representative scheme of hydrated water is shown in Figure 1-6.

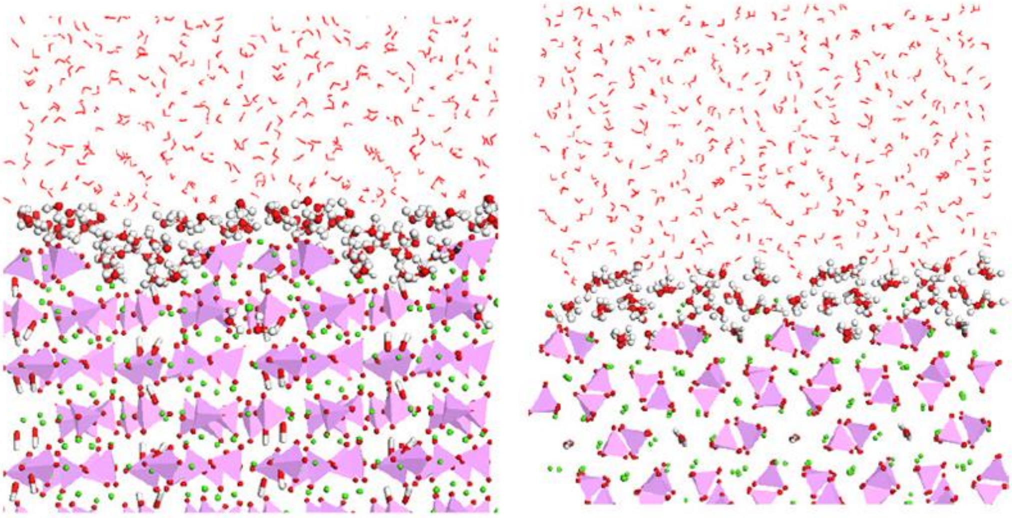

Figure 1-6 The schematic illustration of the hydrated water layer on (0001) plane (left) and $(01\bar{1}0)$ obtained by molecular dynamic simulations. (Calcium= green, oxygen = red, H= white and PO_4 exhibited as tetrahedra, water indicated as small red/white ball and stick model)[46].

Recent analyses of high resolution TEM and NMR results has indicated that although bulk region of nanosized HAp is highly crystalline, its surface has amorphous non-apatitic layer 1-2 nm[47,48]. Therefore, the lowered Ca/P ratios (1.67 to near 1.5) obtained by wet methods are mainly attributed to effect of surface chemistry in this layer and emphasized that bulk and surface of nano HAp crystals have different characteristics[49].

1.2.4 Metallic ion incorporation in HAp for therapeutic purposes

Metallic ions are considered to be promising therapeutic agents for bone tissue engineering. That means metallic ions are incorporated in the porous scaffolding materials that work as a matrix and regulate the release of the incorporated ions in a controlled way within biological environment. Conventionally used organic drugs are not suitable for fabrication of these matrixes as they are more likely to decompose in scaffolds during the processing stage that are mostly exposed to high temperature, pressure as well as free radicals. Therefore, there is a growing interest for use of metallic ions as they are more stable and do not importantly have a risk of decomposition[50]. Also, metallic ions are considered to be capable of interacting with the other ions and bind to macromolecules or activate ion channels or secondary signalling in cellular so that they can change cellular and biological functions[51]. All these functions are closely related to kinetics of release of metallic ions from a matrix material[52]. To illustrate, studies on the bioactive glass show that controlled release of Ca, Si, Na and P ions are influential in the promotion of angiogenesis and enable to increase cell differentiation and osteogenesis (formation of bone tissue). However, extensive release of these ions from can be toxic. Thus, selection of suitable materials and its processing is critical for therapeutic effect of metallic ions[50].

HAp is one of the proper materials that allows the incorporation of metallic ions and releasing of them in biological environments. Therefore, ionic substitution mechanism within bulk and surface of HAp particles as well as therapeutic effect of these substitutes have been extensively studied in recent works. Although many different metallic ions (as therapeutic agents) are doped into HAp, structure-function relationships have been established only for limited ones. Among them, Si^{4+}, Sr^{2+}, Mg^{2+} and Zn^{2+} ionic dopants are basically attributed to enhance bone growth and decrease bone resorption while Ag^{+} and Cu^{2+} ionic dopants are shown to have anti-bacterial effects. Recently, Se oxyanions (SeO_4^{2-} and SeO_3^{2-} ions) doped HAp has been indicated as potential anti-cancer agents. Details about therapeutic performance of the most widely used ions and doping characteristics are given in the followings.

1.2.4.1 Therapeutic ionic incoporation for enhanced bone formation

It is explained by Price et al.[53] that silicon is necessary mineral for the formation of bone and its supplementation leads to increased bone mineral density as well bone strength. Therefore, Si-doped HAp systems has been long studied. Recent *in vivo* performance of these systems has indicated that percent of bone growth and bone/implant coverage for Si-doped HAp particles is considerably greater than pristine HAp particles[54]. Microstructural analysis of Si-doped HAp by Porter et al.[55] indicate that incorporation of silicate ions into HAp enhances the dissolution of Si-doped HAp. With the dissolution, Ca, P and Si ions at the interface of HAp trigger the precipitation of bone mineral and stimulate its growth in successive layers at HAp surface[55].

Strontium is present in bone with considerable amounts and its use in low doses has been known to be influential for the treatment of osteoporosis[32]. Clinical studies have shown that long-term administration of strontium in the form of strontium chloride or strontium ranelate promote bone formation as well as leading to reduction in bone resorption[56]. These promising results of strontium in a number of clinical studies suggest strontium ions as a candidate doping agent for HAp. Structural investigation of Sr-doped HAp particles indicate that strontium ions substitute with Ca ions and preferentially locate at Ca(II) in HAp[57]. Cazalbou et al.[58] also found out that although ionic exchange of strontium at surface of nano HAp is initially high, it decreases with incorporation of more strontium into HAp crystals in long maturation times thereby resulting in high release rate of Sr ions from nano HAp surfaces. Moreover, Capuccini et al.[59] show that Sr-doped nano HAp are successful in the stimulation of osteoblast activity and inhibition of osteoclastic resorption up to near 7 at. % Sr content.

Additionally, Mg and Zn are effectively used as doping agents in HAp. Specifically, implantation of Mg-doped HAp granules in the femoral defects of rabbit has been shown to promote more osteoconductivity and resorption compared to pristine HAp granules[60]. Similarly, implanted zinc-doped hydroxyapatite in femora of white rabbits increase bone formation with the optimum Zn content of f 0.32 wt. %[61]. Although both Mg and Zn dopants substitute with Ca ions in HAp up to 10% and 20% respectively, ion exchange for both dopants is the predominant mechanism at the surface of HAp crystals[32].

1.2.4.2 Major anti-bacterial ionic dopants

Ionic dopants in HAp are also suggested to be used as antibacterial agents. Considering all antibacterial therapeutic ions, Ag^+ ion is highly effective against bacterial cells at very low concentrations of 35 ppb. These concentrations of Ag^+ do not also lead to any toxicity to mammalian cells. In addition, Liau et al.[62] showed that interaction of Ag^+ ions with groups-SH (thiolic) of proteins basically result in the formation of S—Ag bonding that inactivates the bacterial cells by denaturation of the proteins in bacteria[63]. Therefore, Ag-doped HAp has been extensively studied and the antibacterial effect of these systems have been associated with either the interaction of Ag^+ ion at the surface of HAp with cell membrane of bacteria or interaction of Ag^+ ion released from HAp structure with surrounding bacterial cells[63,64]. For not leading any toxicity to healthy human bone-growing cells, Ag^+ doping content has been suggested to be in 2-4 wt. %[65].

Cu^{2+} ion is another potential anti-bacterial agent and has been used as a dopant in HAp. Although recent findings do not fully elaborate the exact mechanism of antibacterial behaviour of Cu^+ dopant in HAp, it is proposed that Cu^+ ions at the surface of HAp changes structural integrity of bacteria by forming strong bond with different organic groups including thiolic, imidazole, amine and carboxylic groups of proteins[63,66]. Stanic et al.[66] also show that Cu-doped HAp are effective against E. coli and C. albicans in vitro tests. However, concentration of Cu^{2+} ion should be less than 0.66 wt. % in Cu-doped HAp to decrease toxic effect of these ions on healthy bone-growing cells.

1.2.4.3 Anti-cancerous ionic dopant: Selenium and its compounds

Selenium is significantly important element and its ionic species are the constitutes of selenoproteins which are essential to human immune systems with their antioxidant function, catalyst role in producing active thyroid hormone and cell proliferation[67,68]. Protective roles of selenium species against cancer cells highly depend on the dose of selenium supplemented and it has been emphasized that the doses of Se higher than dietary intake levels ,that is approximately between 26-34 μg/day, is required in cancer treatment. Specifically, it has been shown that selenium dose of 400 μg/day is the maximum limit for safety while selenium doses of 100-200 μg/day inhibit genetic damage and cancer development in human subjects[69]. Several epidemiological studies have also shown that selenium deficiency may also amplify malignant tumor upturn in prostate, colon, lung, liver and throid pronouncedly[70]. Moreover, low selenium intake cause to increased levels of reactive oxygen species and phosphorylation that lead to inhibitory effect on collagen type-I, alkaline phosphatase expression and differentiation of osteoblasts that are regarded to act in expressing selenoproteins[71].

Selenium and its inorganic compounds have been recently used as coating and dopants against bone cancer. Tran et al.[72] showed that coating of selenium nanoclusters grown on Ti substrate stimulate healthy bone-growing cells while inhibiting the growth of cancerous bone cells. Relevant to Se-doped HAp systems, Wang et al.[73] noticeably showed that incorporation of Se into nano HAp trigger apoptosis of cancerous bone-growing cells and this effect is attributed to the activation of the intrinsic mitochondrial apoptotic pathways. They emphasized by *in vitro* tests (in glass) that Se dopants promote healthy bone-growing cells and possibly inhibit recurrence of cancerous bone cells[73]. Toxicity tests of Kolmas et. al[74] also show Se content for selenite –doped HAp should be less than 1.2 at. % for lowering the toxicity effect while Se content for selenate-doped HAp is non-toxic at doping levels up to 1.6 at. %.

1.3 Objective and structure of the thesis

Main objective of this thesis is to understand surface and crystallite characteristics of Se-incorporated HAp (HAp:Se) nanoparticles and possibly to establish a relationship between enhanced anti-cancer effect of Se ions and structural features of HAp:Se. Using proper calcium, phosphate and selenite precursors, these nanoparticles were synthesized by aqueous precipitation method. It is important to mention that extend of Se incorporation in HAp particles are previously indicated to be effective against osteosarcoma cells (cancerous bone cells) in cell culture tests before. Thus, relative atomic ratio of Se to P was selected as 3 at maximum. Then, surface chemistry and structural refinement of these HAp:Se particles are explored. Determining possible atomic positions of Se ions in HAp:Se structures were especially complicated and a great deal of work on both laboratory and synchrotron based refinements were involved to find out these positions. Overall, most of the characterization results were investigated in a comparative manner.

Structure of this thesis is comprised of two main chapters. *Chapter 2* indicates chemical synthesis protocol and details of the applied analytical techniques. In *Chapter 3,* HAp and HAp:Se nanoparticles synthesized by precipitation methods were investigated to elaborate the changes in their chemical, morphological, structural and thermal properties of HAp nanoparticles upon Se incorporation. By chemical techniques, identification of constituent elements and compounds in bulk and surface of both HAp and HAp:Se and chemical state of Se-related species at the surface of HAp:Se were investigated. These chemical analyses results were further correlated with morphological features of these nanoparticles. Then, whole structure refinement of HAp and HAp:Se were performed and their structural details, e.g. B-type carbonation, were mainly based upon the information obtained by chemical structure analyses. The obtained compositional results by these techniques were compared to thermal decomposition behavior of HAp and HAp:Se nanoparticles to state proper temperature ranges in which Se ions are present in HAp:Se crystal structure.

CHAPTER 2

MATERIALS AND METHODS

The nanocrystalline hydroxyapatite (HAp) and Se-incorporated hydroxyapatite (HAp:Se) powders were synthesized by aqueous precipitation using proper calcium, phosphor and selenium precursors. In this chapter, experimental procedure of the precipitation process and calcination of as-synthesized HAp and HAp:Se powders were described. Material characterization techniques and analyses methods were subsequently explained in this chapter.

2.1 Materials

Pure HAp and selenium-incorporated HAp (HAp:Se) nanoparticles were synthesized using calcium nitrate tetrahydrate ($Ca(NO_3)_2{\bullet}4H_2O$, 99.0%; Sigma-Aldrich), ammonium hydrogenphosphate ($(NH_4)_2HPO_4$, 98%; Sigma-Aldrich), sodium selenite (Na_2SeO_3, Bioreagent, suitable for cell culture, 98%; Sigma-Aldrich), ammonium hydroxide ($NH_4(OH)$, 26% NH_3; Sigma-Aldrich) and ethanol (absolute, 99.8%; Sigma-Aldrich). All reagents were used without further purification. Ultrapure deionized (DI) water was used in all experiments.

2.2 Experimental Procedures

0.25 M calcium nitrate tetrahydrate was first prepared in 600 mL DI water at 25°C. Meanwhile, the required amounts of ammonium hydrogenphosphate (0.1478M, 0.1463M and 0.1449M) and sodium selenite (0.0015 M, 0.0030 M and 0.0045 M) was mixed in a single beaker containing 600 mL DI water to achieve Ca/(P+Se) ratio of 1.67 and to obtain Se/P molar ratios as 1, 2, and 3. Ammonium hydroxide was then added into the mixed solution to sustain the pH at 10. Afterwards, calcium-containing solution was dropwise added into the mixed solution of ammonium hydrogen phosphate and sodium selenite using 20 mL syringes involved in an automated injection pump (Top-5300 model syringe pump) at a rate of 60 mL/h in ambient conditions. Ammonium hydroxide was constantly added during the injection process to keep solution with a pH at approximately 10. During the injection, white precipitates were instantaneously formed via the following solution-based reaction;

$$10Ca(NO_3)_2 + 2(NH_4)HPO_4 + 8NH_4OH \rightarrow Ca_{10}(PO_4)_6(OH)_2 + 20(NH_4)NO_3 + 6H_2O$$

Once injection was completed, the parent solution was heated at 60°C and aged at this temperature for 12 h. Then, the precipitated powders were collected by centrifugation at 8000 rpm [using Eppendorf 5805 model (Eppendorf AG, Hamburg, Germany), with a rotor radius of 115 mm] for 5 min. After that, the centrifuged particles were ultrasonically washed with DI water to remove nitrates and also in ethanol solution for dispersion of agglomerated precipitates (for 30 min at room temperature using Branson 3510 model ultrasonic bath). Following ultrasonic treatments, the precipitates were again collected by centrifugation at 10000 rpm for 5 min. and then dried on a borosilicate glass plate at 105°C overnight. Afterwards, the particle sizes of as-dried solid precipitates were reduced by milling operation adding zirconia balls to the mixture in Nalgene bottles that contain the precipitates covered by acetone solution. The resultant powders were used for the characterization purposes. For comparison, pure HAp was synthesized through the same experimental procedure with a small exception where Ca/P ratio in calcium nitrate tetrahydrate and ammonium hydrogen phosphate aqueous solutions was provided as 1.67.

Some of as-synthesized HAp and HAp:Se powders are calcined between 600-1100 °C with a temperature increment of 100 °C. For each calcination operation, a heating rate of 5 °C/min, delay time of 1h and furnace cooling to room temperature were carried out. The chemical synthesis protocol is described in Figure 2-1 by a summarizing flowchart.

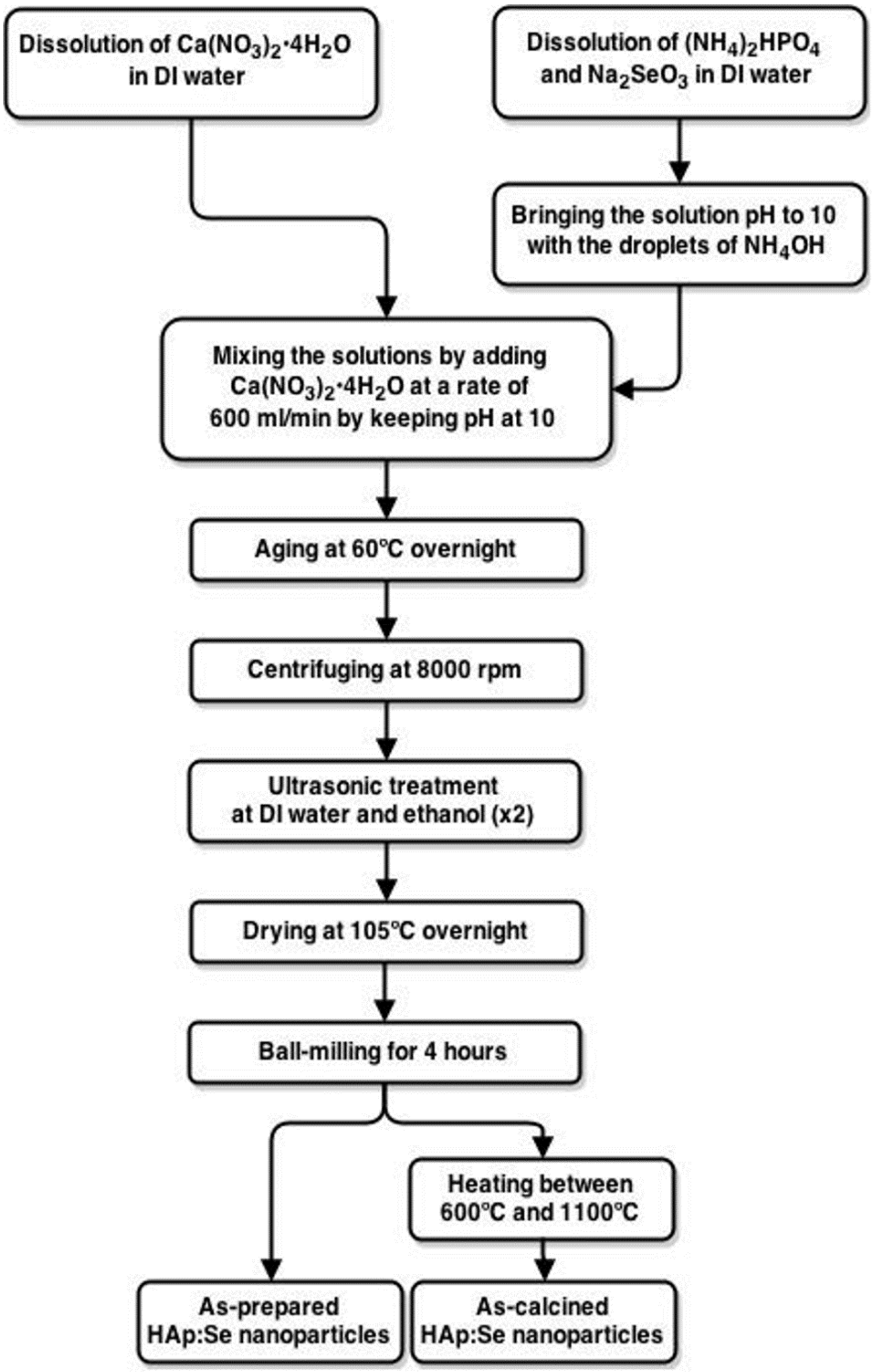

Figure 2-1 Flowchart of the precipitation process of Se incorporated HAp nanoparticles.

2.3 Characterization of as-synthesized and as-calcined HAp and HAp:Se nanoparticles

2.3.1 Energy dispersive X-ray analysis

Energy dispersive X-ray spectroscopy (EDS) was performed for chemical identification and composition of constituent elements. Each EDS spectrum was collected at 30 kV for 90 sec. using EDS detector in JEOL 2100 F model (JEOL Ltd., Tokyo, Japan). EDS analyses were completed according to elemental compositions at 10 different agglomerated nanoparticles. Due to low reliability of compositions of carbon and oxygen atoms for EDS analyses, their compositions were excluded from the computed results. Average at. % of each element was finally computed including standard deviations.

2.3.2 Chemical structure analysis: Infrared Spectroscopy

Fourier transform infrared spectra (FTIR) were used to determine chemical structure of pure and Se-incorporated nanoparticles using a Frontier-PerkinElmer (equipped with PIKE GladiATR Reflection, Specular Reflectance tools). For FTIR analyses, samples were prepared by mixing 3 mg HAp and HAp:Se nanoparticles with 200 mg KBr powders dried at 105°C. The mixture was well pulverized for a minute and filled into a pellet-forming die. A force of roughly 7 tons was applied for 40 sec and 13 mm transparent pellets were obtained. Spectroscopic analyses were then completed in absorbance mode between 4000-400 cm^{-1} with 4 scan-accumulation. For the background, pure KBr pellets formed by 200 mg KBr powders using the same sample preparation procedure was employed. As a supplementary tool, attenuated total reflectance (ATR) scans of all samples were also evaluated and preferentially utilized for identifying absorbed peaks of carbonate groups as well as the nitrate groups. Baseline of all FTIR spectra was finally corrected for comparative analyses.

2.3.3 Surface composition and chemical state analysis: X-ray Photoelectron Analysis

For chemical state evaluation of Se-related species, x-ray photoelectron spectroscopy (XPS) was used to obtain the regional XPS spectra collected by a PHI 5000 VersaProbe spectrometer (Physical Electronics, Chanhassen, MN) operated at 58.7 eV. High resolved scans of C1s and Se3d spectral regions were numerically fitted using the second derivative method in Peak Fit 4.12 software and examined to calculate approximate carbonate content and figure out the chemical state of Se incorporate. According to the calculated carbonate contents, atomic composition of constituent elements are adjusted and examined. The binding energies (BE) and charge corrections were calibrated to the C1s line at 284.8 eV.

2.3.4 Particle size analysis

A few droplet of nonionic surfactant (TWEEN 80) was added to the dispersed slurry and the powders were then exposed to ultrasonic treatment for 5 min. Afterwards, the average particle size of each sample was obtained using Malvern Mastersizer 2000 particle size analyzer.

2.3.5 Thermal Analysis

As-synthesized particles were placed into alumina crucibles and heated between 30°C and 1100°C using EXSTAR TG/DTA 7300. Weight loss (TG), derivative of weight loss (DTG) as well as differential temperature changes (DTA) were measured for revealing possible decomposition mechanism with elevating temperatures.

2.3.6 Morphological investigation: Scanning and Transmission Electron Microscopy

Particle shape, size and size distribution of as-synthesized powders were investigated using FEI NOVA NANO430 model scanning electron microscope (SEM) and JEOL JEM2100F model (JEOL Ltd., Tokyo, Japan) transmission electron microscope (TEM). Both SEM and TEM specimens were prepared by ultrasonic dispersion of agglomerated nanoparticles in ethanol solution for 10 minutes. Then, SEM samples were prepared by using few droplets of dispersed solution while those of TEM are prepared by the suspension of powders on holey carbon-coated copper grids. For analysis of particle size distribution, 50-100 particles from low magnification TEM images were examined to investigate average particle size distribution and standard deviations. High resolution TEM images were used for determining crystallinity and surface feature of HAp and Se-incorporated HAp particles.

2.3.7 Phase identification: X-ray Diffraction Analysis

Secondary phase formation and qualitative evaluation of crystallinity were explored with x-ray diffraction (XRD) analyses using a Rigaku D/Max-2000 PC diffractometer (Rigaku Corporation, Tokyo, Japan). XRD powder pattern was obtained at an operating voltage of 40 kV and the current of 30 mA using Cu $K\alpha$ radiation (λ: 1.5418 Å). XRD pattern was scanned between 2θs of 20°-80° at a rate of 0.5°/min.

2.3.8 Whole pattern structural analysis: Rietveld Refinement

Crystallite size, microstrain, precise lattice constants and detailed structural parameters of HAp were calculated executing full profile refinement with both use of GSAS and GSASII softwares[75,76]. Laboratory-based XRD patterns scanned at a rate of 0.1°/min. was employed for profile and structural refinements. Also, synchrotron-based XRD patterns scanned between 2θ ranges of 3°-30° using wavelength of 0.4133 Å. To obtain the instrumental parameters, standard reference material of LaB6 660b and Si 640c were used for lab and synchrotron based refinement, respectively. The related refinement of both standard sample is shown in Figure 2-2 and Figure 2-3. Shifted chebyschev function with 6-9 terms was used for background fitting depending on complexity of background patterns while peak shape function was selected as convoluted pseudo-Voight to consider anisotropic crystallite size and strain. In particular, as having a better fit than isotropic model, unaxial size and mustrain model with unique axis of 0001 was used to calculate equatorial and axial crystallite sizes. In the final stage of full pattern refinement, structural terms including atomic positions and site occupancies are simultaneously refined. Atomic displacement parameters (ADPs) were directly obtained from single crystal of Holly Springs HAp and not changed during the refinement[77]. Similarly, for carbonate and Se-related ions, ADP of 0.12 and 0.003 values were used respectively without any refinement[78].

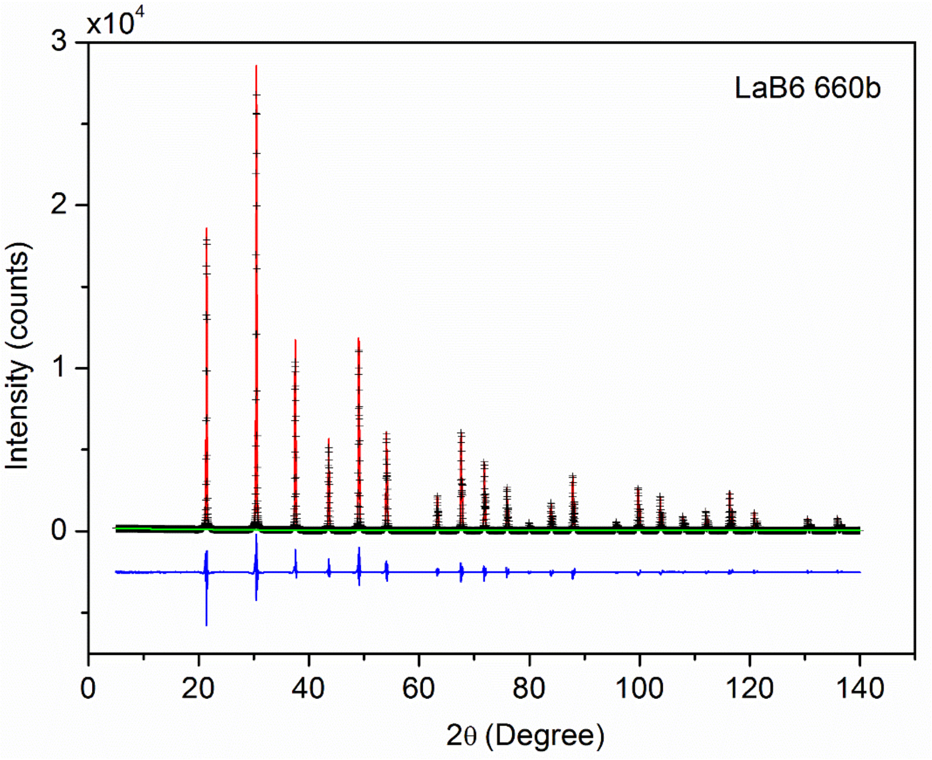

Figure 2-2 Refined XRD pattern of standard LaB6 660b showing observed (plus signs), calculated (red line), difference(blue lines) and background (green lines) data.

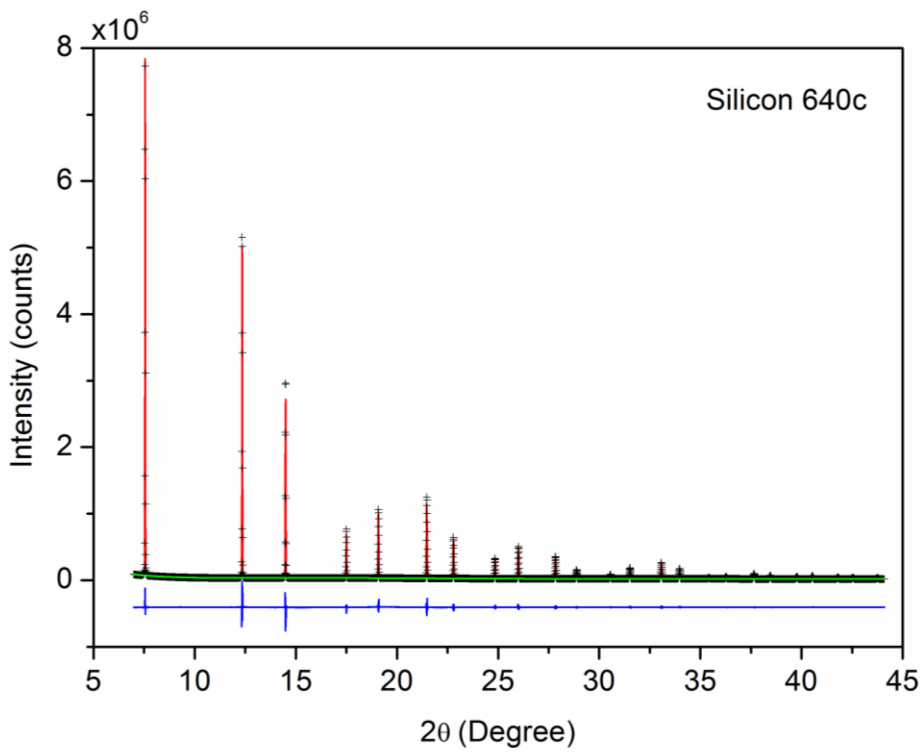

Figure 2-3 Refined plot of XRD pattern of standard Silicon 640c showing observed (+ signs), calculated (red line), difference(blue lines) and background (green lines) data.

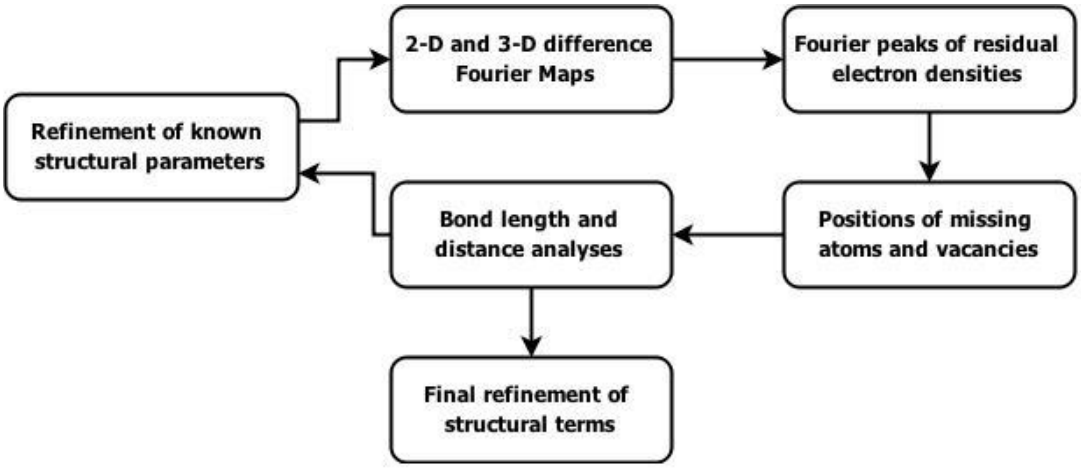

Figure 2-4 Analysis procedure for structural parameters during the whole pattern structural refinement through Rietveld method.

In order to determine the positions of Se-related groups and other incorporated ions, difference Fourier maps (DELF) were used and analyses of bond lengths and angles were completed subsequently. For carbonate impurities in pure HAp structure, bond distances of C—O and O—O were soft restraint to the values of 1.294 and 2.241 and allowed to be refined. As to Se incorporated HAp, the atomic positions of incorporated ions were determined based on residual electron density from the corresponding DELF and satisfying bond length and angles. Procedure of solution of ionic species within HAp was summarized in Figure 2-4. The obtained results were used to reveal nature of ionic incorporates, charge compensation mechanism and structural modifications within HAp lattice.

CHAPTER 3

CHEMICAL AND STRUCTURAL CHARACTERIZATION OF SELENIUM INCORPORATED HAP

In this chapter characterization of HAp and HAp:Se in both as-synthesized and as-calcined form has been presented. Methodologically, the bulk and surface composition of powders were determined through EDS and XPS analyses. For quantitative analyses chemical structure of the as-synthesized particles, infrared absorption bands in transmission mode were investigated. Chemical information obtained by the spectral chemical analyses was attempeted to be confirmed by complete structure analyses through both laboratory and synchrotron based XRD patterns. Crystal structural refinements were also compared to one another to elaborate the extent of Se incorporation, carbonation content and possible chemical state of ionic species in crystalline region of as-synthesized nanocrystalline HAp and HAp:Se particles. Finally, thermal analyses results and infrared spectra analyses of calcined HAp and HAp:Se particles were compared to explain decomposition ranges of incorporated ionic species in HAp crystal structure.

3.1 Elemental Analyses

Elemental compositions and atomic ratios of constituent elements were indicated in Table 3-1. It was clearly observed that the calculated Ca/P and Ca/(P+Se) atomic ratios were lower than their stoichiometric ratio of 1.67. A recent study based on NMR analysis elaborated the variations in calculated Ca/P ratios and indicated that the bulk and surface compositions of HAp in nano-dimensions considerably changes the overall composition and relevant ratios of constituent ions[49]. Hence, agglomeration state of as-synthesized HAp and HAp:Se particles were considered to modify the actual atomic compositions and ratios as both core and surface regions of HAp particles have partial contributions on the calculated compositions.

Nonetheless, the calculated Se/P ratios were reasonably close to the expected ratios in Table 3-1 and imply that Se ions well incorporated into whole HAp particles.

It was additionally observed that the calculated Ca/P ratio of large agglomerated particles (greater than ~10 µm) is in the range of 1.58-1.63, which is more close to the stoichiometric Ca/P ratio of 1.67, while the Ca/P calculated in the small agglomerates (less than ~2 µm) was almost always close to 1.5. Size-dependent changes in Ca/P ratio can be interpreted that higher surface area in the smaller agglomerates directly increases the contribution of ionic composition at the surface to overall compositions for HAp and HAp:Se particles thereby reducing the Ca/P ratio.

Table 3-1 The calculated atomic ratios and the compositions of consituent elements of HAp and HAp:Se powders using standardless EDS analyses.

	HAp	**HAp:Se1**	**HAp:Se2**	**HAp:Se3**
Se(at. %)	0	0.39 ± 0.02	0.73 ± 0.06	0.99 ± 0.07
P (at. %)	40.76 ± 1.78	40.02 ± 1.24	40.50 ± 0.52	40.41 ± 1.03
Ca (at. %)	59.24 ± 1.78	59.59 ± 1.24	58.78 ± 0.56	58.60 ± 1.00
Se/P(expected)	0	1	2	3
Se/P (measured)	0	0.97 ± 0.05	1.79 ± 0.13	2.67 ± 0.27
Ca/(Se+P)	1.50 ± 0.09	1.46 ± 0.08	1.43 ± 0.03	1.41 ± 0.02

It is important to mention that the obtained HAp precipitates mostly include carbonate ions in different amounts. Despite the exclusion of carbon from EDS analyses, relatively increasing signal intensity of carbon in EDS spectrum of each sample in Figure 3-1 also support the carbonation of HAp particles. Thus, both Se ions and carbonate ions were considered to lead to varying Ca/(P+Se) ratios. Moreover, relatively calcium deficient composition of HAp:Se particles , except for HAp:Se1, can be associated with maintaining the charge neutrality destructed by ionic species of C and Se incorporates within both lattice and surface of HAp precipitates. This approach is valid for all HAp:Se particles, as no significant signal intensities assigned to sodium from the precursor chemicals was obtained from their EDS spectra. As a result, the obtained particles can be basically considered in the form of Ca-deficient HAp.

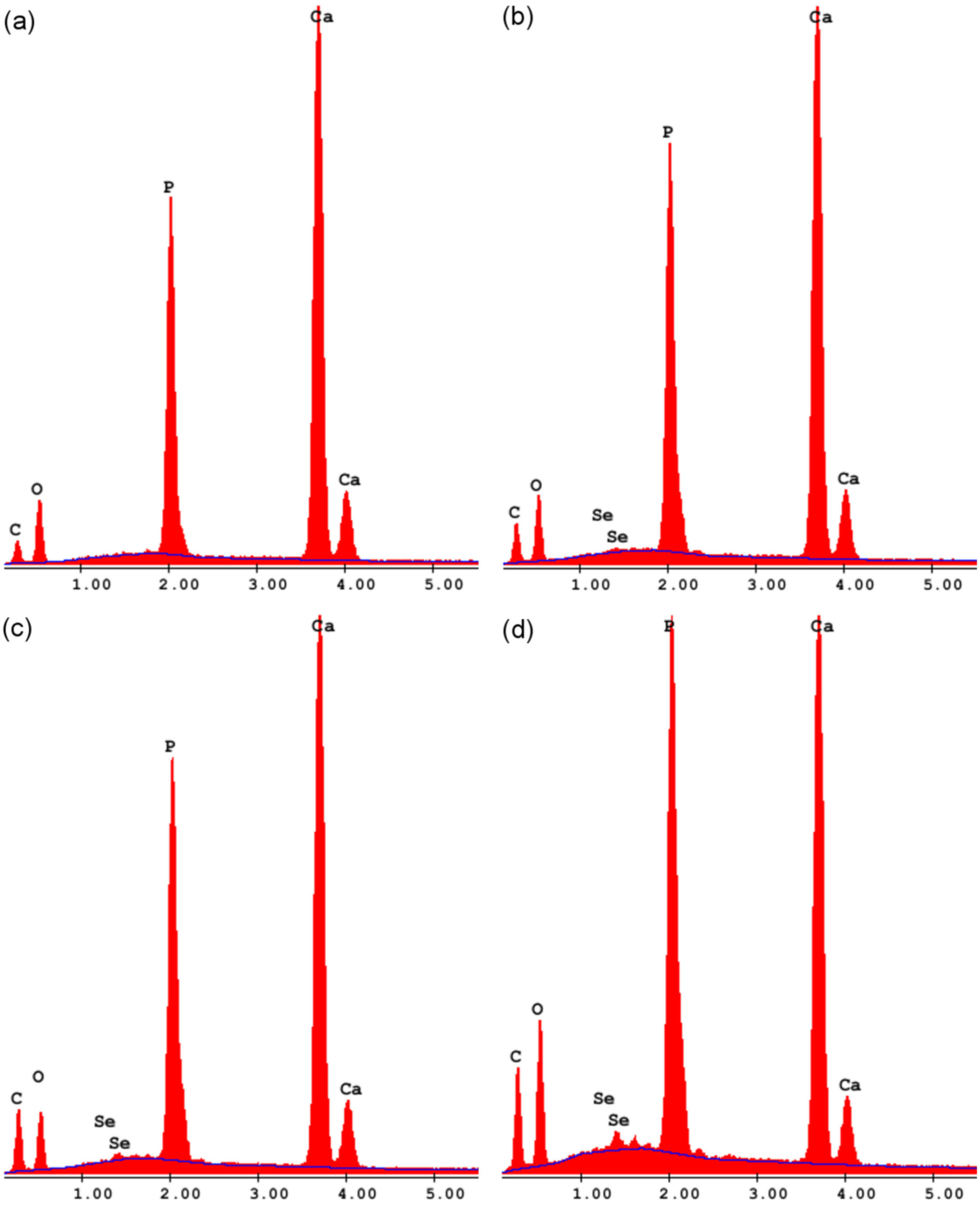

Figure 3-1 EDS spectra of as-prepared nanoparticles of HAp(a), HAp:Se1(b), HAp:Se2(c) and HAp:Se3(c). The x-axes is energy in keV, y axes is intensity in cps.

3.2 Morphological Analyses

Implications deduced from EDS analyses were evaluated by investigating microstructural features of as-synthesized HAp and HAp:Se particles. Highly agglomerated state of HAp and HAp:Se nanoparticles were observed from the SEM images in Figure 3-2. Apparently, the particle size distributions in all agglomerates are observed to be fairly homogenous and the similar average agglomerate sizes (~7-9 µm) were determined by the particle size analyzer and the calculated values are indicated in Table 3-2.

In addition, both HAp and HAp:Se particles were observed to exhibit uniaxial-like form with big dimensions in length (axial) and small dimensions in width (equatorial). The details of particle morphology are shown in TEM micrographs in Figure 3-3. It was also observed that outer surface of all nanoparticles have low crystallinity region that corresponds to 1-2 nm thickness at the surface. These surface regions are mainly attributed to adsorbed and hydrated H_2O, CO_3^{2-} ions as well as HPO_4^{2-} ions[44,47,48]. Also, as regard to the sorption properties of Se oxyanions on HAp surface at basic pH values, great deal of Se ions can be considered to accommodate near crystallite surface of HAp:Se nanoparticles[79].

Moreover, Figure 3-3 show that all particle sizes have single crystalline structures and nano-dimensional sizes, namely less than 100 nm in both abovementioned dimensions. By quantitative measurements, the size distributions of the previously dispersed nanoparticles (about 50-100 nanoparticles) were determined based on low magnification TEM images in Figure 3-3. Calculated average nanoparticle sizes are shown in Table 3-2. It is worth to mention that, the calculated sizes for HAp and HAp:Se crystallites are in good agreement with the dimension of bone mineral[80]. In addition, despite significant deviations from them, the average nanoparticle sizes of HAp:Se systematically decreases with increased content of Se ions when compared to those of HAp nanoparticles. Considering the similar changes in crystallite sizes of Si-doped HAp[32], decreasing particle size of HAp:Se can be associated with increased amount of amorphous region in both bulky and surface of HAp:Se, and more likely due to surface accommodation of Se ions.

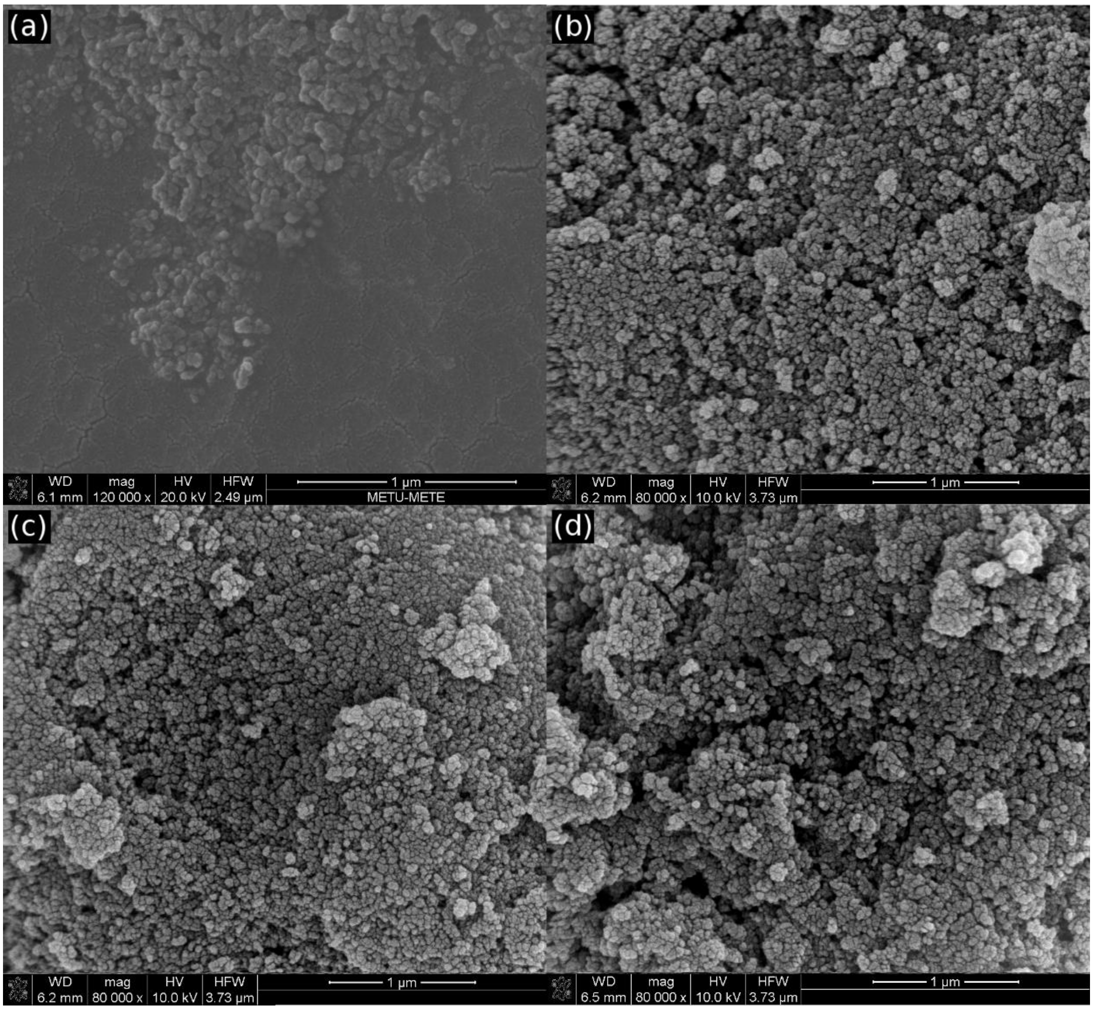

Figure 3-2 SEM micrographs indicating the agglomeration of HAp and HAp:Se nano crystals. HAp(a), HAp:Se1(b), HAp:Se2(c), HAp:Se3(d).

Table 3-2 Average crystallite and agglomerate sizes of HAp and HAp:Se.

		HAp	**HAp:Se1**	**HAp:Se2**	**HAp:Se3**
Average Crystallite Size (nm)	*Eq.*	19.8 ± 4.4	18.5 ± 2.4	13.5 ± 2.6	14.3 ± 2.8
	Ax.	45.9 ± 7.9	39.3 ± 9.4	30.1 ± 6.4	28.9 ± 6.6
Average Agglomerate Size (µm)		7.31	7.71	6.95	8.80

* Equatorial and axial particle sizes are abbreviated.

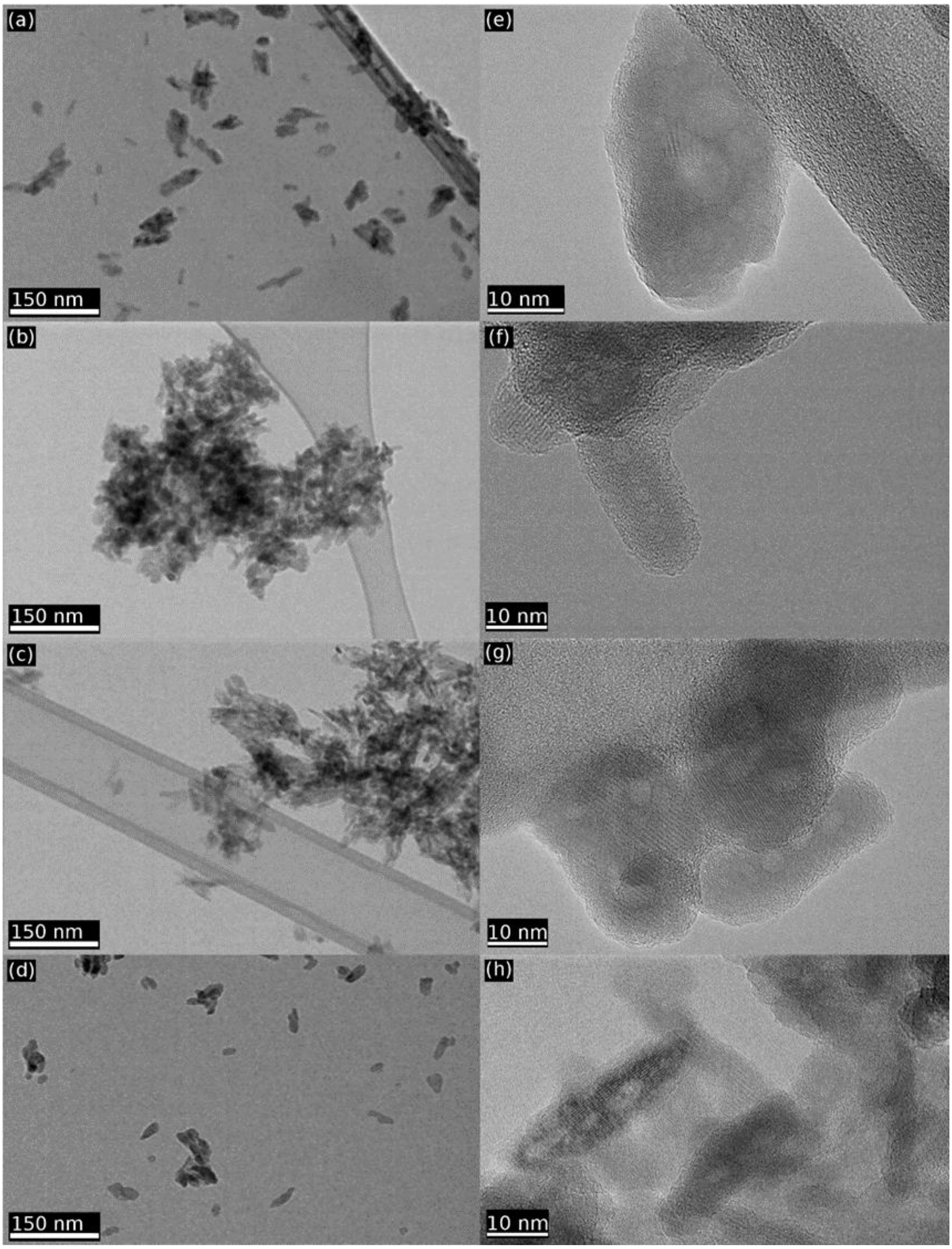

Figure 3-3 Size, shape and size distribution of as-prepared crystallites; HAp (a, e), HAp:Se1 (b, f), HAp:Se2 (c, g) and HAp:Se3(d, h). The left column (a, b, c, d) respresents low magnification images of the respective crystallites while the right column represents high magnification images of them (e, f, g, h).

3.3 Chemical Structure Analyses

Chemical structure analyses were carried out using the following infrared spectra that indicate functional groups in different wavenumber regions of FTIR spectra. 4000-2200 regions in Figure 3-4 revealed distinctive band of OH^- groups at around 3571 cm^{-1} as well as the broad bands of water molecules at 2600-3600 cm^{-1}. It was previously shown that adsorbed water was specifically characterized by the three distinct bands at 3600, 3450 and 3250 cm^{-1} that represents the υ_3, υ_1 and $2\upsilon_2$ modes[81]. According to the obtained results of 4000-2200 cm^{-1} IR region, the υ_3 and υ_1 modes of water molecules were observed for all samples but the selenium incorporated infrared spectra included an extra band shoulders at around 3200 cm^{-1} that can be assigned to the $2\upsilon_2$ mode representing overtone of HOH bending mode[81]. These bands are considered to be associated with poor surface crystallinity of HAp:Se nanoparticles that allows observation of the $2\upsilon_2$ mode of adsorbed water, that is normally observed when the particles are exposed to atmospheric water for long periods[82]. Also, highly intense bands of water molecules can be partially associated with the affinity of KBr powders to adsorb water molecules during the pellet preparation. Moreover, OH^- bands in the infrared spectra of HAp and HAp:Se were observed to position at near 3571 cm^{-1} without any significant shift in their wavenumbers. Clearly, the intensities of absorbance signals of these bands relative to those of the adsorbed water reduces and can be attributed to increased extent of surface selenium incorporation for HAp:Se.

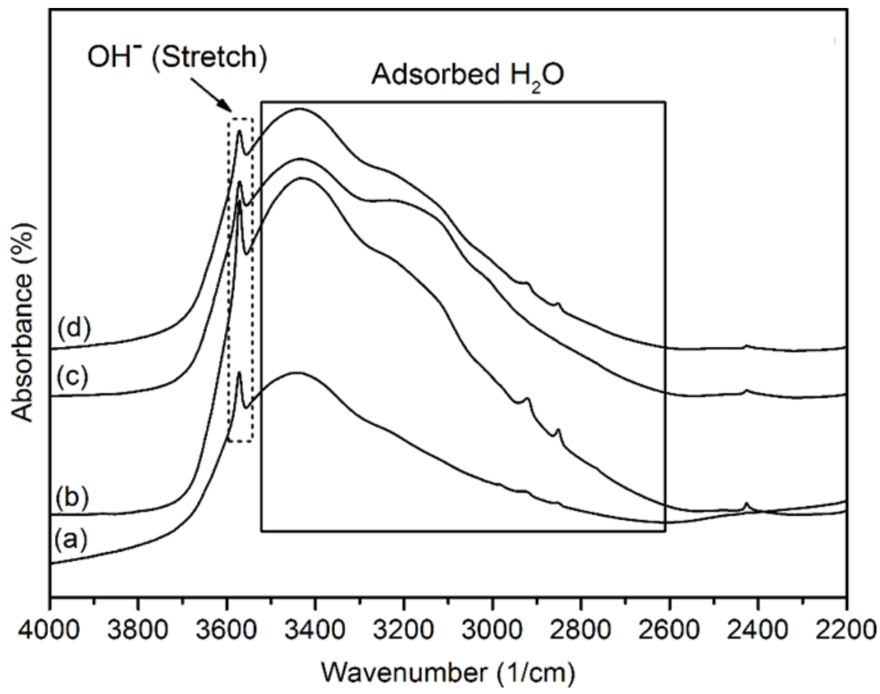

Figure 3-4 Infared spectra of adsorbed water bands and hydroxyl ion peaks of HAp (a), HAp:Se1 (b), HAp:Se2 (c) and HAp:Se3(d)

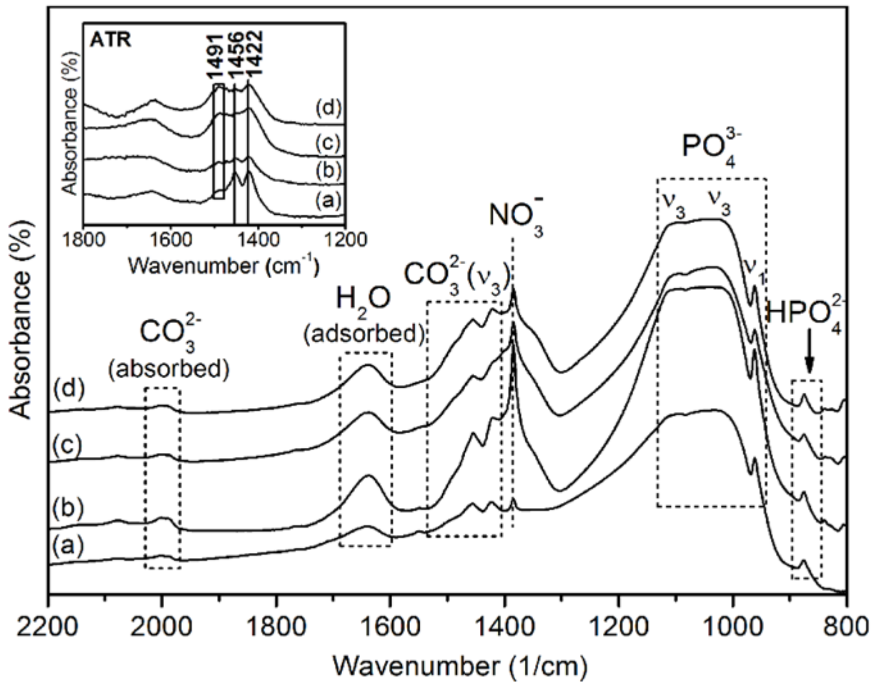

Figure 3-5 FTIR spectra and carbonate, nitrate and phosphate regions (ii). ATR spectra in inset figure showing B-type carbonate bands and lack of nitrate bands; HAp (a), HAp:Se1 (b), HAp:Se2 (c) and HAp:Se3(d).

In the region 2200-800 cm^{-1} in Figure 3-5, the υ_1 mode of PO_4^{3-} was observed at 961 cm^{-1} and well-defined bands associated with the υ_3 mode of PO_4^{3-} were observed at 1031 and 1092 cm^{-1}. The results of ATR analyses as inset figure in 1800-1200 cm^{-1} and the analyses in 2200-800 cm^{-1} revealed that the υ_3 mode of CO_3^{2-} were related to B-type mechanism which has the characteristic bands at 1422, 1456 cm^{-1} [83–85]. Additional bands at 1487 and 1491 cm^{-1} can be related to ionic incorporates of B-type CO_3^{2-} equivalent band intensities of which were qualitatively observed to enhance with more Se content[40,86]. The estimated formula by Featherstone, that shows the relationship between substituted B-type carbonate contents and their infrared absorption bands, was used for lattice carbonate content[10,87]. The standard deviation of the calculated carbonate contents in this formula was described to be less than ± 10 %[10,87].

$$\text{wt\% } CO_3^{2-} = 16.1\,(E_{1415} / E_{575}) - 0.2 \qquad (1)$$

The absorption bands of B-type carbonate ions in Figure 3-5 was used to calculate the extinction coefficients at the bands 1415 cm^{-1} and 575 cm^{-1}. For the calculation of these coefficients, the logarithm of the baseline transmittance to peak transmittance ratios were taken. Consequently, lattice carbonate contents were calculated for HAp, HAp:Se1, HAp:Se2 and HAp:Se3 as 3.99 %, 3.26 %, 5.68 % and 4.86%. Therefore, there is no direct correlation between CO_3^{2-} and Se-related species incorporation; however, the enhanced B-type carbonation was triggered for increasing Se oxyanion content in HAp, mostly for HAp:Se2 and HAp:Se3. Moreover, the bands at 875 cm^{-1} was attributed to those of HPO_4^- that is usually observed to locate near the surface of HAp crsytals[49]. No explicit bands associated with A-type carbonation mechanism were observed in the whole spectra. Moreover, the bending band of adsorbed water was observed at 1640 cm^{-1} [82]. The relatively higher intensity of adsorbed water band for Se substituted samples can be related to more disordered structure of HAp that allows to adsorb the water molecules over the particle surface. Additionally, the bands at 1384 cm^{-1} was attributed to N—O stretching bands absorbed by KBr powders in the prepared pellets as ATR scans of all samples indicated no N—O bands associated with both pure and Se-incorporated HAp particles[88].

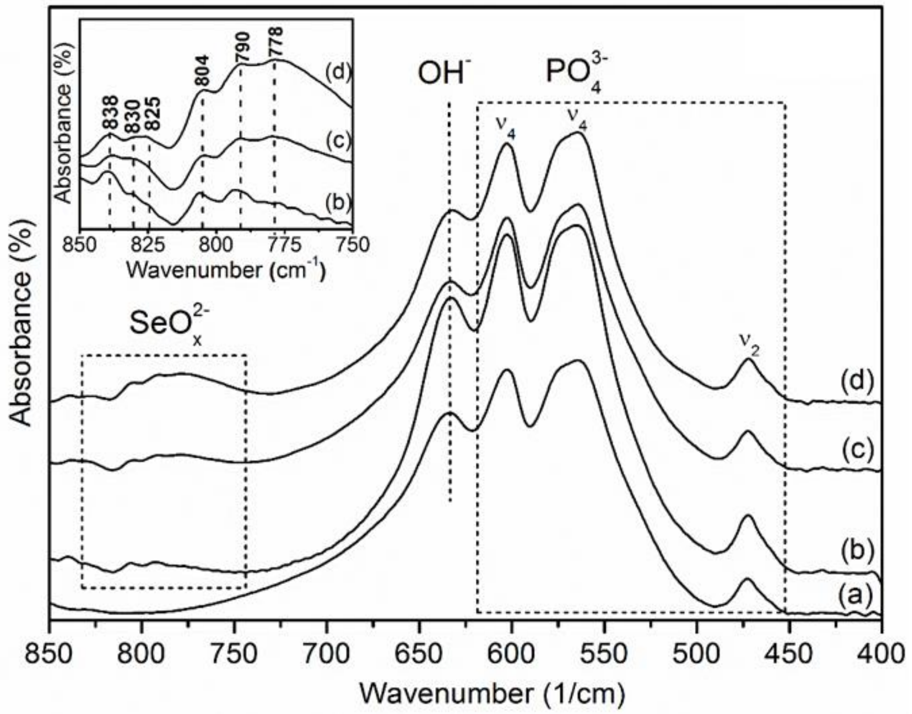

Figure 3-6 Infrared spectra of phosphate and Se oxyanion regions in 850-400 cm^{-1} (iii) and detailed examination of Se-related regions in 850-750 cm^{-1} of the same figure; HAp(a), HAp:Se1(b), HAp:Se2(c) and HAp:Se3(d).

The region 850-400 cm^{-1} in Figure 3-6 shows the IR bands of phosphate and hydroxyl groups as well as selenium-related ionic species. Particularly, highly intense bands related to the υ_4 mode of PO_4^{3-} were assigned at 565, 575 and 602 cm^{-1}. Also, the weak band at 472 cm^{-1} correlated with the υ_2 mode of PO_4^{3-}. Position of the phosphate bands in the region 625-450 cm^{-1} were observed to be appropriate with those of carbonated HAp in previous studies[89,90]. Also, librational mode of OH^- was observe at near 632 cm^{-1}.

Furthermore, the region between 850-750 cm^{-1} indicates the additional peaks in infrared spectra for Se incorporated samples and was thoroughly investigated exhibiting weak absorption signals in the inset plot. The results reveal that the bands at around 778 and 824-825 cm^{-1} can be attributed to $HSeO_3^-$ while those at around 790-793, 830 and 838 cm^{-1} were more likely associated with SeO_3^{2-} [91]. Increased content of Se incorporates were correlated with enhanced signals for $\upsilon_{as}(SeO_2)$ groups of $HSeO_3^-$ specifically observed at around 778 and 824 cm^{-1}. Furthermore, the bands at 830 cm^{-1} can be associated with the monodentate selenite complexes[92].

Additional bands at 804-805 cm^{-1} were not representative for functional groups of Se oxyanions but can be related to free selenite ions considering their approximate absorption frequencies[92]. Thus, these bands can be indirectly interpreted as adsorbed SeO_3^{2-} groups positioning near the surface region of HAp particles.

3.4 Surface Composition and Chemical State Analyses

XPS survey scans in Figure 3-7 indicates the characteristic XPS signals of Ca, P and O as well as presence of the contaminated C and Se. According to the signal positions in Table 3-3, no significant changes in the binding energies were observed for constituent elements but Se-incorporated samples, except for HAp:Se2, show slightly lowered binding energies more likely due to the distorted structure of HAp:Se crystallites. In addition, the resultant Ca/P and Ca/(P+Se) ratios were obtained near 1.33 that is much lower than stoichiometric Ca/(P+Se) ratio of 1.67. Thus, amorphous surface features explored on the surface of HAp and HAp:Se crystallites through TEM imaging were supported by the analyses of surface compositions by XPS regional scans.

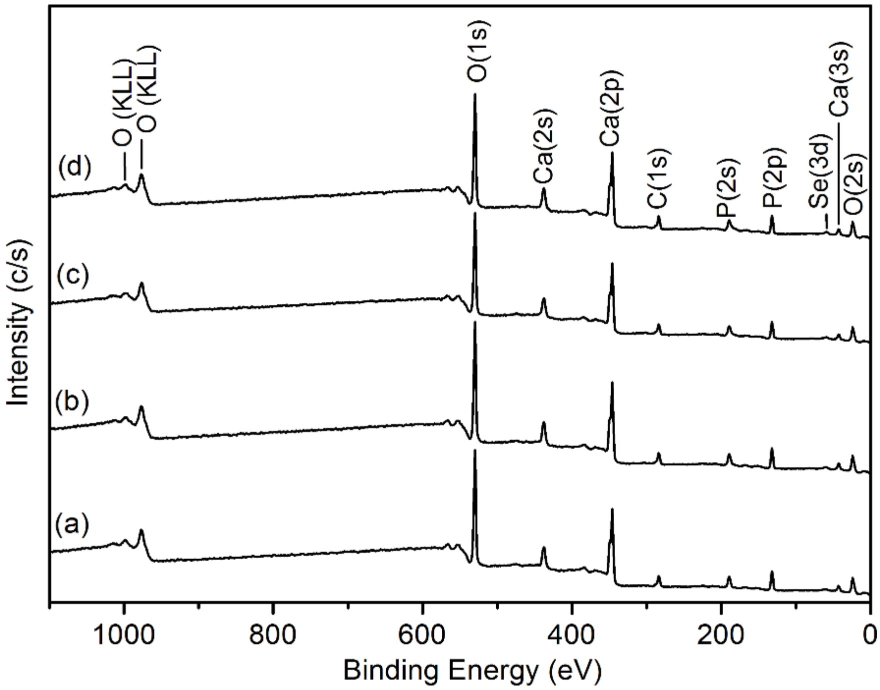

Figure 3-7 Survey XPS spectra of HAp(a), HAp:Se1(b), HAp:Se2(c) and HAp:Se3(d).

Table 3-3 Binding energies and surface compositions (at %.) of the constituent elements of HAp and Hap:Se samples.

Sample		**HAp**	**HAp:Se1**	**HAp:Se2**	**HAp:Se3**
BE (eV)	Ca ($2p_{1/2}$)	350.62(2)	350.50(1)	350.79(9)	350.52(1)
	Ca($2p_{3/2}$)	347.10(1)	346.97(1)	347.19(2)	346.98(1)
	P (2p)	133.13(1)	133.06(1)	133.28(1)	133.05(1)
	O (1s)	530.95(2)	530.84(2)	530.99(3)	530.83(3)
at. %	Ca (2p)	20.38	19.55	19.9	19.83
	P (2p)	15	13.84	12.89	12.56
	O (1s)	62.4	61.4	61.56	61.24
	C (1s)[a]	2.22	3.39	3.34	4.14
	Se (3d)	0	1.83	2.30	2.23

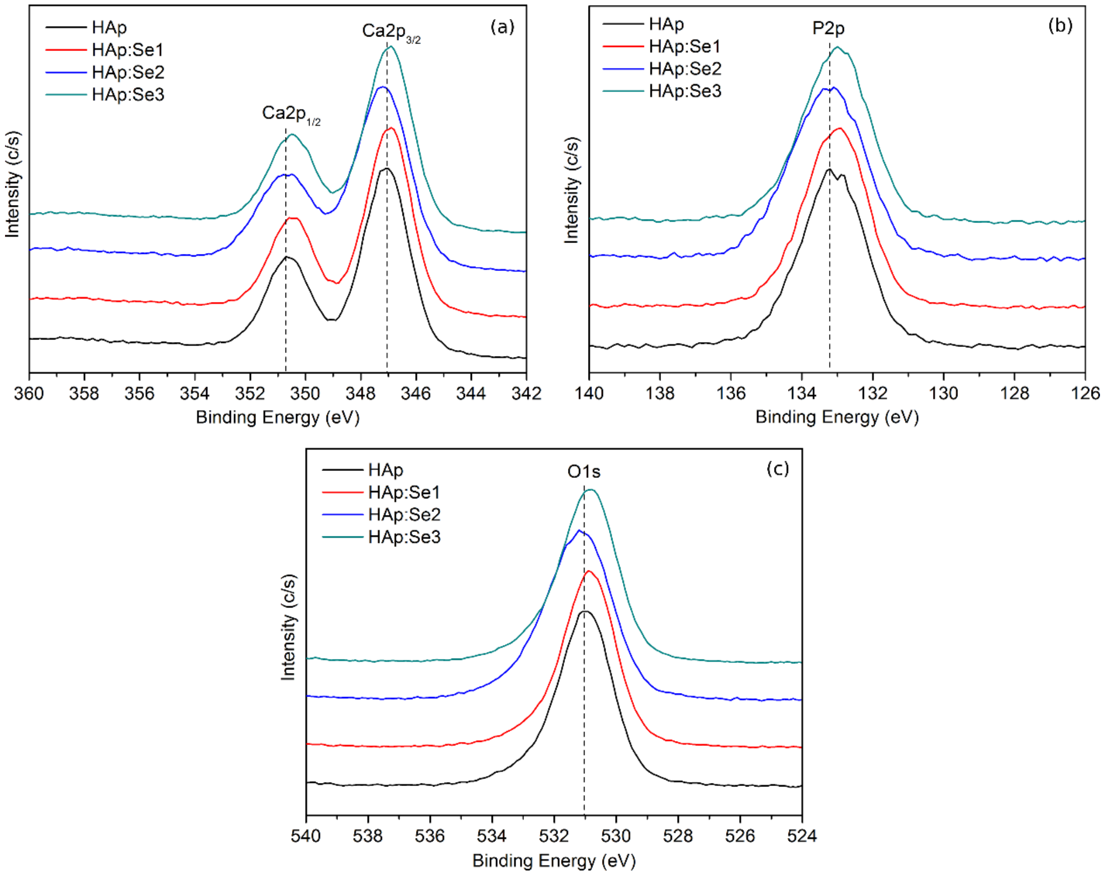

Figure 3-8 Comparative results of regional XPS scans of Ca2*p* (a), P2*p* (b) and O1*s* (c).

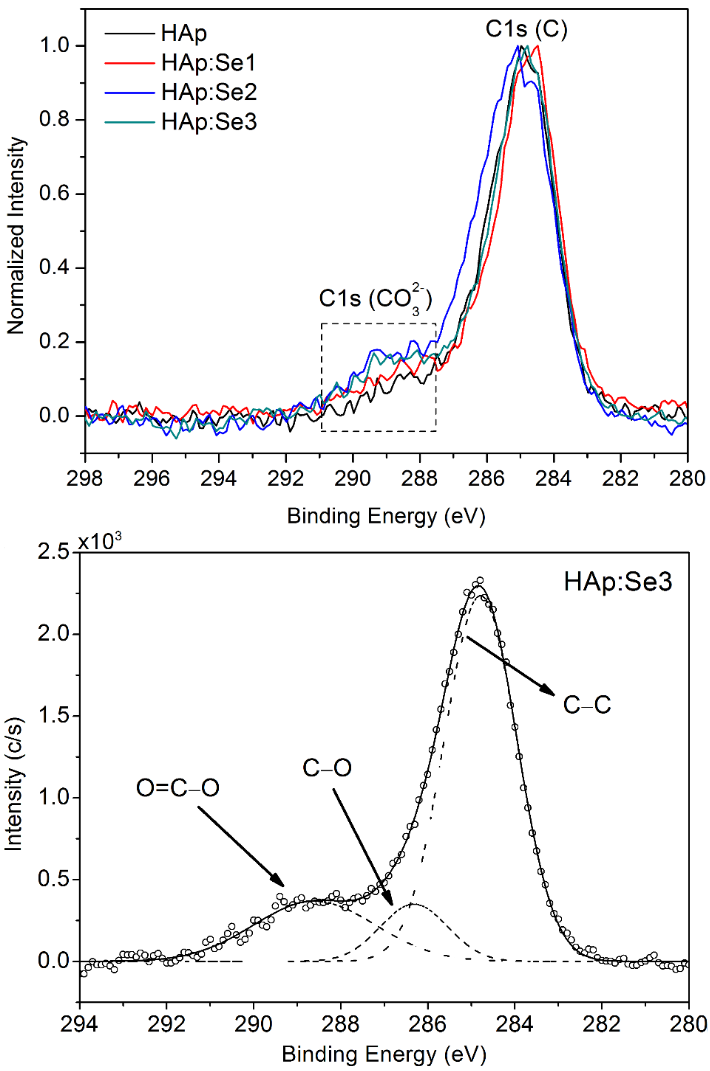

Figure 3-9 XPS regional analyses (left) of HAp:Se3 near C*1s* peaks (294-280 eV).

Characteristic signals of carbon impurities in the region 294-280 eV for both pure and Se-incorporated HAp crystallites were shown in Figure 3-9. Accordingly, the signals at 284.6 eV and 286.3 were attributed to adsorbed hydrocarbon impurities while C*1s* peak near 288.8 eV was assigned to carbonate type carbon[93]. Calculation of carbonate contents in Table 3-4 suggests that Se oxyanion incorporation considerably increased the composition of CO_3^{2-} near surface of HAp crystallites. However, consistent variation in surface CO_3^{2-} composition are not well-matched with inconsistent variation in bulk compositions of B-type CO_3^{2-} within HAp structure, obtained by Featherstone relationships[87]. Thus, it is important to distinguish the surface and bulk compositions of incorporated CO_3^{2-} impurities for all samples.

Table 3-4 Calculation of carbonate content (at. %) as regard to calibrated adventitious peak of C1s.

Samples	Peak	C (total)		C (carbonate)	
		BE (eV)	*% C (total)*	*BE (eV)*	*% C (carbonate)*
HAp	C 1s	284.8	14.7	288.7	1.16
HAp:Se1	C 1s	284.8	15.5	288.7	2.96
HAp:Se2	C 1s	284.8	16.0	289.1	2.90
HAp:Se3	C 1s	284.8	18.2	289.4	3.59

Chemical state of Na and Se incorporates were evaluated in the region 64-56 eV in using the analyses of regional scans of Na*2s* and Se*3d*$_{5/2}$ orbitals for pure and Se incorporated powders. Figure 3-10 shows both comparative experimental and fitted regional spectra of all samples as well as deconvoluted spectrum of Se incorporated powders in the inset plots. Small peak at 62.76 eV can be attributed to Na^+ associated with Na*2s* orbital observed in the portion 64-62 eV[93]. Thus, single peak at 62.76 eV in the highest Se-containing powder can be suggestive for ionic substitution between Ca^{2+} and Na^+.

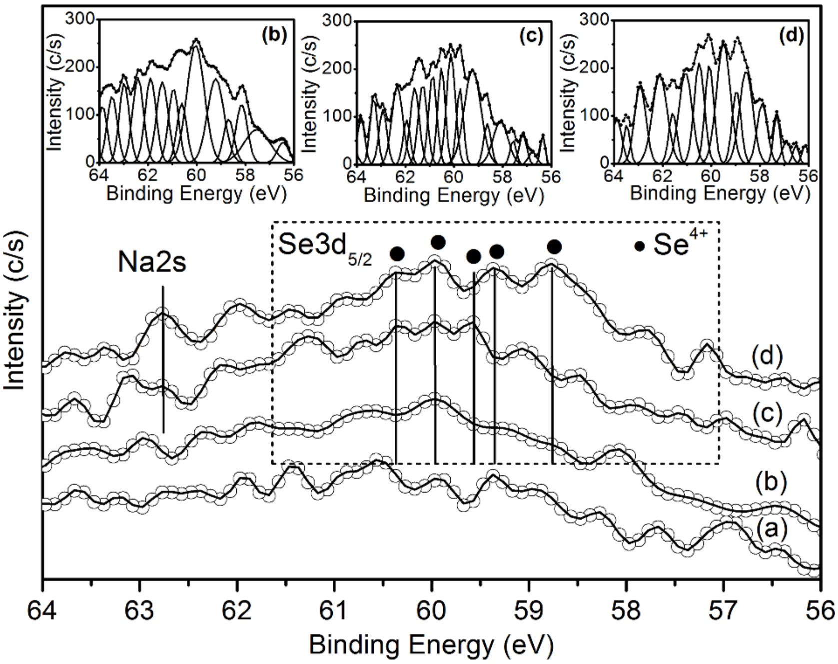

Figure 3-10 Chemical state analyses (right) of the Se3d region (64-56 eV) based upon peak fitting of the obtained data (o) and the simulated data (—). The deconvoluted curves in the both 294-280 eV and 64-56 eV regions also shown as insets for selecting the most intense peaks; HAp(a), HAp:Se1(b), HAp:Se2(c) and HAp:Se3(d).

For Se-related ions, $Se3d_{5/2}$ spectral line of Se^{4+} in different chemical formulations were observed from detailed XPS analysis. Deconvoluted spectra of HAp:Se reveal that distinguishable signals at 59.36, 59.97 and 60.37 eV can be attributed to H_2SeO_3 whereas the signal at 58.76 eV was most likely the characteristics of SeO_2[79,93–97]. Also, Figure 3-11 indicates that the binding energies of Se*3p* are close to 165 eV and well-matched with those of SeO_2[94].According to these results, Se ions in the state of Se^{4+} are suggested to locate at the surface of HAp:Se crystallites. Moreover, it was apparently observed that overlapping of Se*3d* peaks with small background peak near 62-58 eV in all XPS profiles may lead to unreliable identification of constituent elements in HAp as observed in a previous study[98]. However, XPS profile changes associated with Se(LMM) at 300-305 eV and Se (LMM1) peaks at near 180 eV in Figure 3-11 clearly indicates enhancing surface compositions of Se ions. Specifically, the binding energies of the maximum Se (LMM) auger peaks in 300-305 eV decrease from 304 eV to 301 eV for increasing content of Se ions in HAp. Similarly, binding energies of HAp:Se was measured as approximately 182 eV, 181 eV and 180 eV for HAp:Se1, HAp:Se2 and HAp:Se3 respectively.

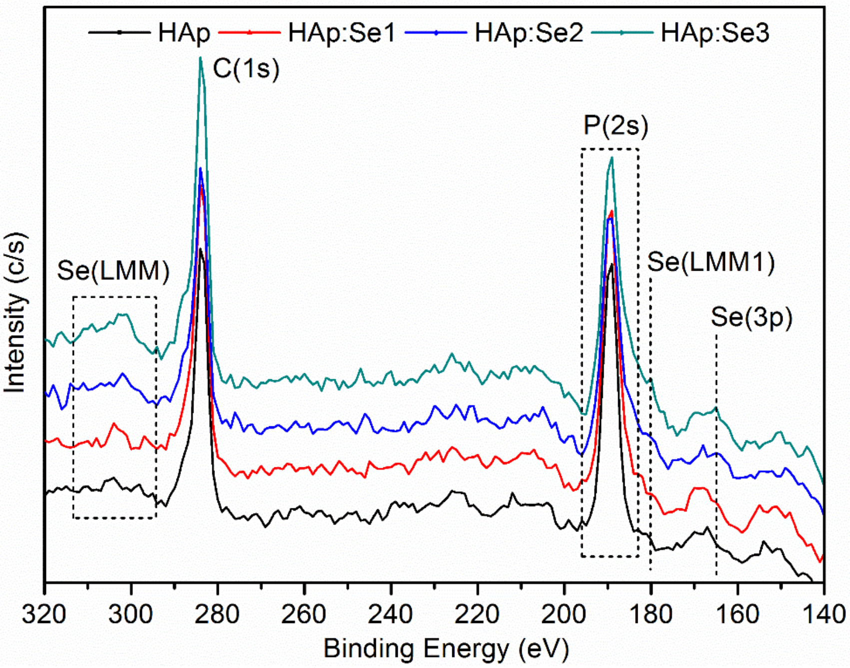

Figure 3-11 The region between 320-140 eV in survey XPS data showing increasing content of Se^{4+} ions at HAp:Se surface according to the relative Auger peaks of Se(LMM) and Se(LMM1) as well as Se(3p).

3.5 Structural analyses of HAp and HAp:Se nanoparticles

3.5.1 Analytical studies on lab-scale XRD patterns

Figure 3-12 shows XRD diffractograms of pure and Se-incorporated HAp. Each diffraction pattern was a single phase, HAp (JCPDS card no: 09-0432), and indicates no other phase observed in each and every case. As a result of Se incorporation into HAp, diffracted peaks were observed to get broadened while their intensity and sharpness decrease with increasing Se content. These changes can be mainly correlated with poorer crystallinity, smaller crystallite size and lattice strains due to Se-incorporation in HAp crystals.

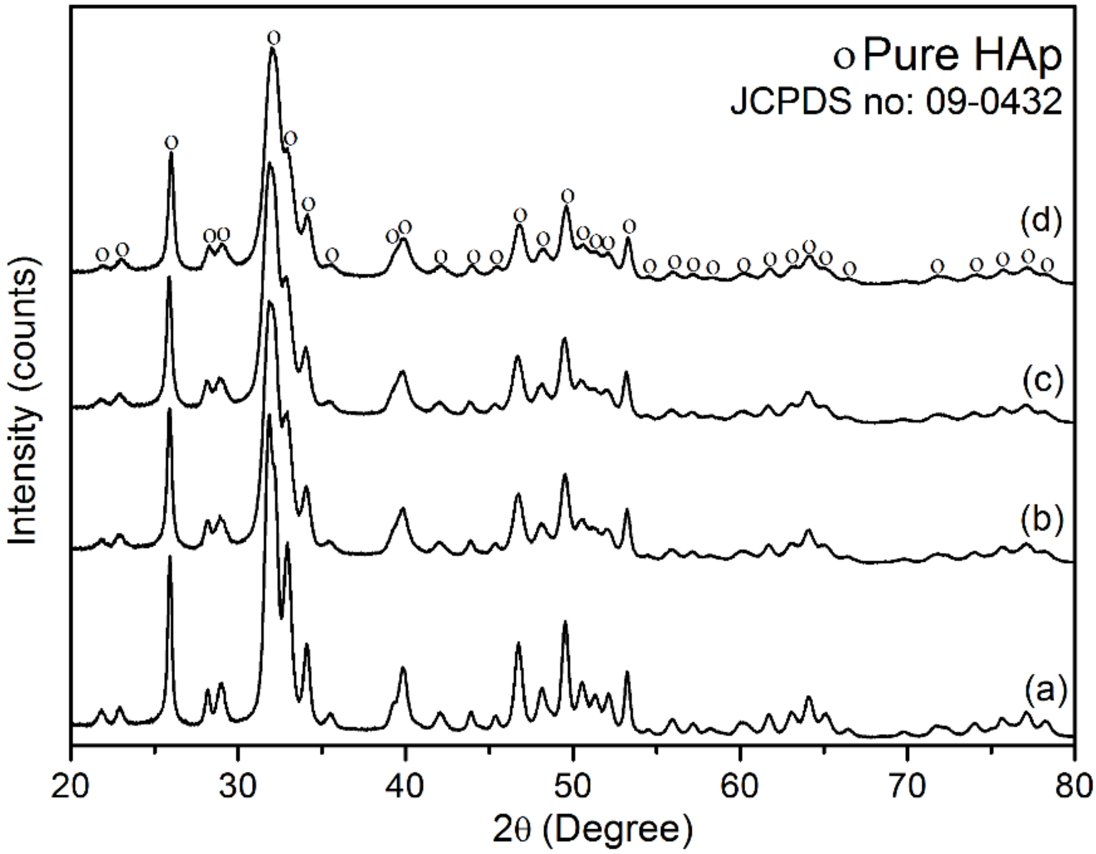

Figure 3-12 Comparative XRD results that indicate the peak profile changes upon Se ion incorporation; HAp(a), HAp:Se1(b), HAp:Se2(c) and HAp:Se3(d).

In addition to the qualitative information obtained from XRD diffractograms, full profile refinements were further carried out through Rietveld analysis for quantitative determination of the modified profile and structural parameters for both HAp and HAp:Se. Following to Rietveld refinement, HAp and HAp:Se crystal structures were explored by the difference Fourier maps to find out the positions of CO_3^{2-} and Se-related species in the respective crystal lattices.

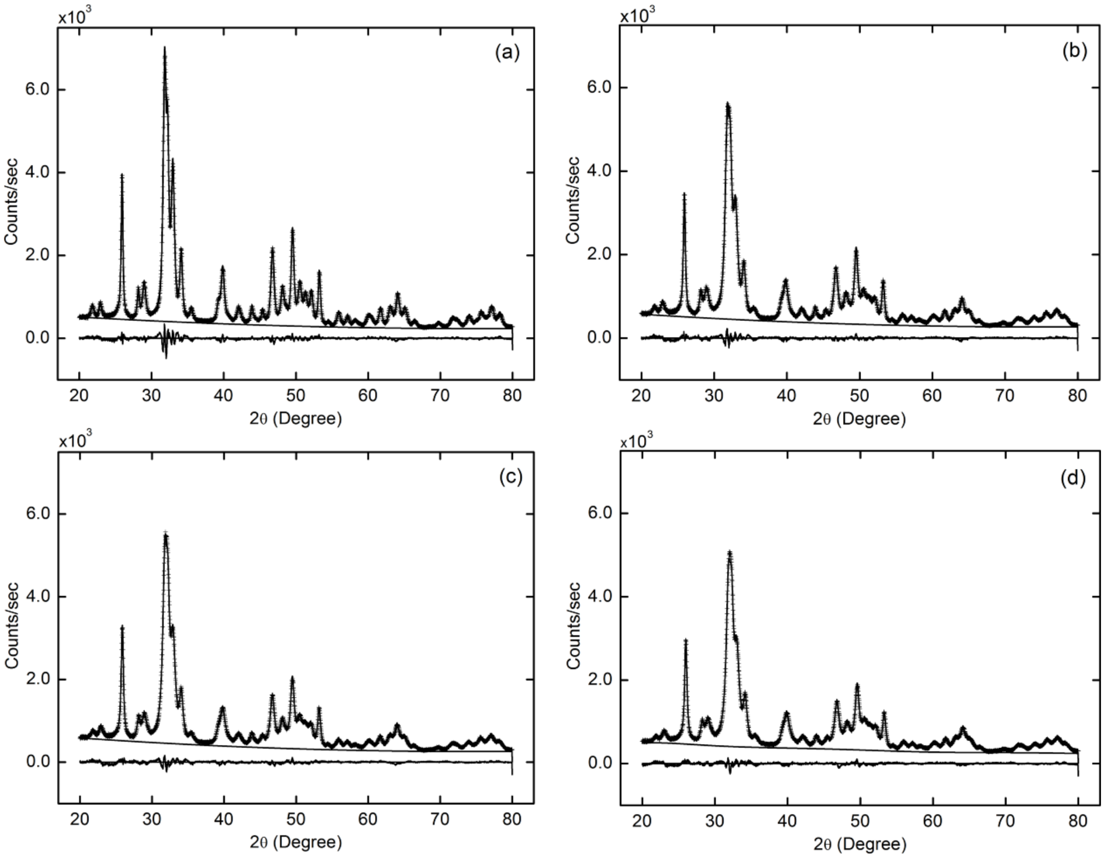

Figure 3-13 The refined profile plots of HAp and HAp:Se3 diffractograms. The observed (+) , calculated (—) intensities in the plots and the difference curve (bottom) indicated; HAp(a), HAp:Se1(b), HAp:Se2(c) and HAp:Se3(d).

Full profile refinement plots using carbonated HAp model (Space Group: $P6_3/m$) were shown in Figure 3-13. Both experimental and simulated plots of all XRD patterns were consistent with one another as it was confirmed by both accurate profile fitting in Figure 3-13 and chi-square values given in Table 3-5. According to the results in Table 3-5, lattice parameters of HAp crystal structure decreases systematically with extent of Se incorporation. The reason for this change in both lattice parameter can be attributed to decreased occupancy of Ca^{2+} ion HAp structure within so-called closepacked sheets[34]. Alternatively, ionic replacement of Ca^{2+} ions with smaller ions were also can be possible reasons for decreasing lattice parameters in a-axis with extend of Se ions[34]. The reduction of lattice parameters in c-axis can also be related to decreasing site occupancy for both oxygen atom in OH^- channel and Ca^{2+} ions which are located parallel to OH channels.

Changes in the lattice parameters were also considered to be relevant to enhanced microstrains in HAp and HAp:Se crystallites. Table 3-5 shows that microstrains calculated in equatorial direction were in reverse relationship with changes in lattice parameters in a-axis. Moreover, for the microstrains in axial direction, structure of HAp:Se crystallites are observed slightly more strained than that of HAp and imply that decreased lattice constants in c-axis can be relevant to this strain behaviour of HAp:Se. Simulation of uniaxial microstrains were shown in Figure 3-14.

Furthermore, the crystallite sizes calculated by Rietveld method are in well agreement with those calculated from low magnifications TEM images in Table 3-5. Reducing pattern of the crystallite sizes with increased extend of Se incorporation were attributed to both poor crystallinity of HAp:Se lattice as well as its surface. Simulation of HAp and HAp:Se crystallites were shown in Figure 3-15.

Table 3-5 The refined peak profile and unit cell parameters as well as reduced chi-square values of the final refinements.

Samples		**HAp**	**HAp:Se1**	**HAp:Se2**	**HAp:Se3**
χ^2		1.38	1.13	1.24	1.28
R_{wd} (%)		4.01	3.29	3.35	3.41
Crystallite Size (nm)	*Equatorial*	22.4(1)	16.6(2)	16.2(1)	14.4(1)
	Axial	45.8(5)	39.0(6)	34.8(4)	31.9(3)
Mustrain (µstrain)	*Equtorial*	2.8(1)e3	4.4(4)e3	5.8(3)e3	6.5(3)e3
	Axial	1.3(1)e3	1.9(2)e3	1.9(1)e3	2.0(1)e3
Lattice parameter (Å)	*a*	9.4228(2)	9.4211(3)	9.4142(3)	9.4152(3)
	c	6.8831(1)	6.8783(2)	6.8754(2)	6.8745(2)

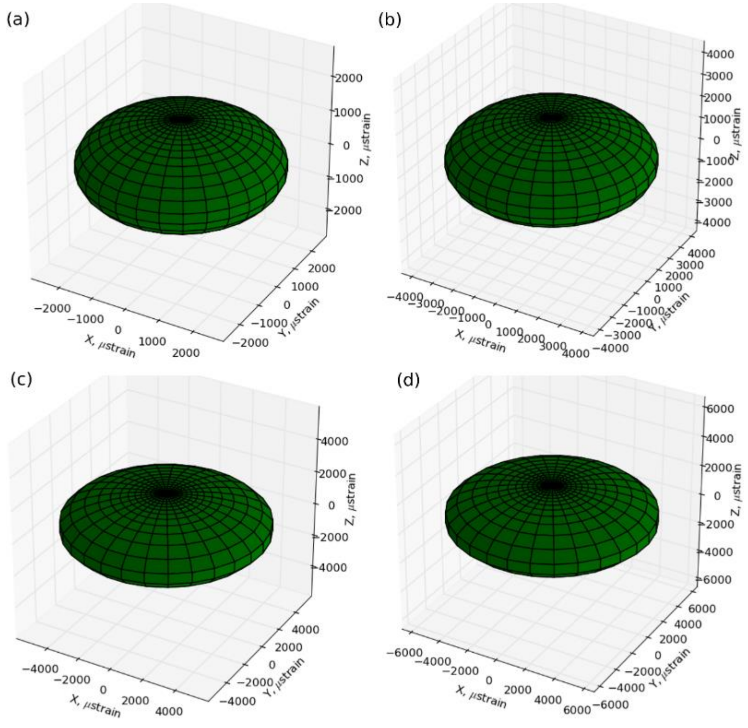

Figure 3-14 Simulated plots of μstrain as regards to Rietveld refinements based on uniaxial model of crystallites; HAp(a), HAp:Se1(b), HAp:Se2(c) and HAp:Se3(d).

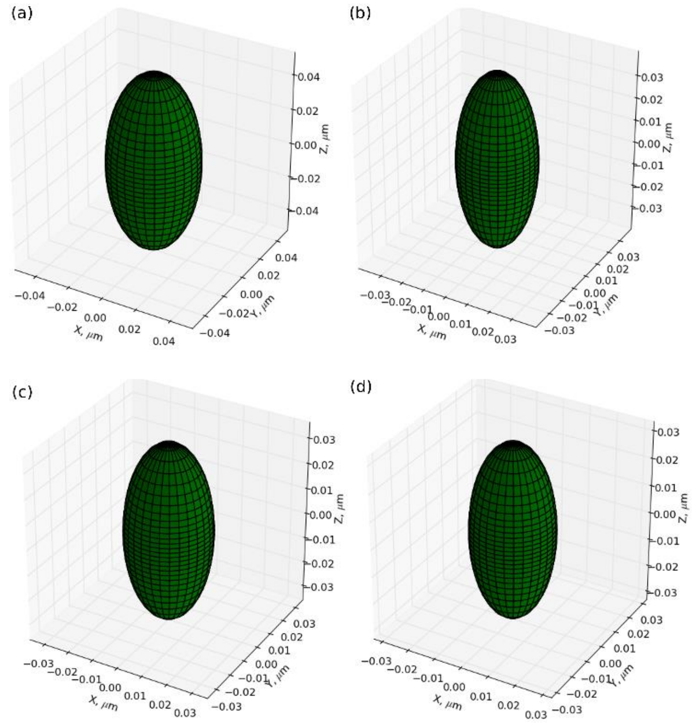

Figure 3-15 Simulated images of HAp and HAp:Se crystallites as regards to the Rietveld refinements based on uniaxial model of crystallites; HAp(a), HAp:Se1(b), HAp:Se2(c) and HAp:Se3(d).

Based on the refined structural and profile parameters, difference Fourier peak positions obtained by XRD diffractogram of HAp crystal structure were tabulated in Table 3-6. According to the indicated peak positions regarding to their residual scattering of electrons, peak 6 in HAp was initially attributed to the positions of oxygen atom in OH^- channel and was shown in Figure 3-16. Consistent with the calculations of bond distances around this oxygen atom, water molecules were considered to be involved in OH^- channels as the calculated bond lengths around this oxygen atom with other residual positions approach to 0.9644 Å. This result was quite similar to the average bond distance attributed to water molecules[99]. Yet, the refinements including these O atoms at peak 6 did not lead to increased convergence in final refinement in HAp. Therefore, position of peak 6 is not involved in structural model of HAp.

Table 3-6 Positive difference Fourier peaks of HAp showing possible positions of incorporated ions as regard to their residual electron densities.

Peak No.	**Pure HAp**			
-	Rho	x	y	z
1	20.2	0.0429	0.3930	0.25
2	20.0	0.1233	0.2701	0.25
3	18.5	0.2319	0.0210	0.1089
4	17.8	0.5618	0.0760	0.1277
5	16.0	0.7581	0.1499	0.0234
6	15.3	0	0	0
7	14.8	0.5067	0.2242	0.25

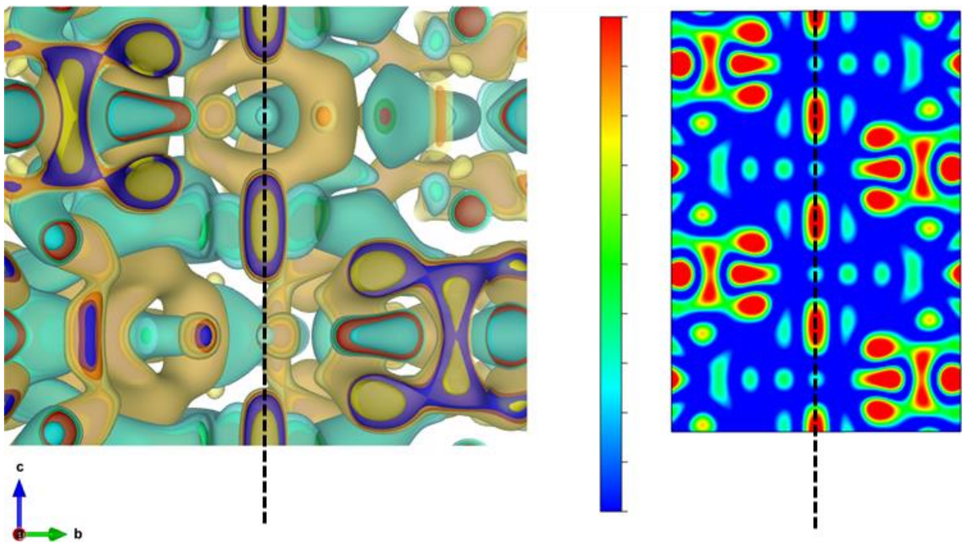

Figure 3-16 3D(left) and 2D(right) difference fourier maps of HAp along z-direction. Estimated position of O ion is indicated along dotted lines.

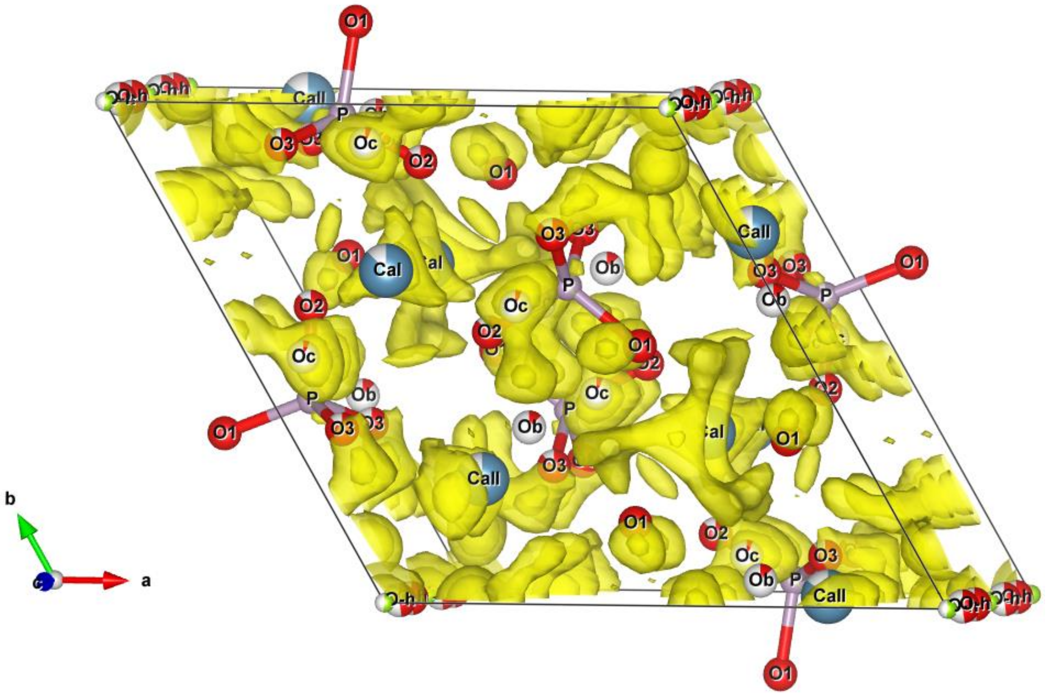

Figure 3-17 Positive difference Fourier peaks of HAp:Se3 obtained by difference fourier maps. Note that there is high electron density just around PO_4^{3-} tetrahedra.

Further investigation of HAp structure through Fourier peaks in Table 3-6 show that most of the peak positions are close to the positions of oxygen atoms in phosphate tetrahedra. Therefore, instead of using residual electron densities, well-established models of Wilson et al.[78] and Fleet et al.[100] on B-type carbonated HAp structures were considered for locating the carbonate ions around the phosphate tetrahedra for pure HAp. Considering these models, total composition of phosphate and carbonate ions were constrained to 6. Also, O—O bond distances in carbonate structure are restrained to 2.241Å with a tolerance of 0.02Å and restraint weight was allowed to refine up to 0.5.

As for determining the position of Se and CO_3^{2-} ions in HAp:Se, DELF maps of HAp:Se3 were investigated. Related DELF maps of HAp:Se3 was shown in Figure 3-17. It is important to mention that DELF calculations of HAp:Se1 and HAp:Se2 were not completed due to complexity of overlapping electron scattering in their crystal structure.

From the obtained residual electron scatterings in HAp:Se3, positions of peak 3 and O1 were considered to be associated with the position of peak 2 in that the bond distances between these positions just near the PO_4^{3-} tetrahedra have similar bond distances of O—O in calcite structure[99]. Specifically, their bond distances were computed as 2.1530(1)Å, 2.2375(1)Å and 2.2893(1)Å while the corresponding bond angles were computed as 60.39(0)°, 62.82(0)° and 56.78(0)° respectively. Since the resultant bond lengths and angles were reasonable with the O—O distances and angles for CO_3^{2-} ions in the previous studies (referring to calcite structure), the atomic position of peak 2 was incorporated into the atomic positions of HAp:Se3[99].

Table 3-7 Fourier peak position of HAp:Se3 based on DELF maps.

Peak No.	**HAp:Se3**			
-	Rho	x	y	z
1	23.9	0	0	0
2	19.4	0.3884	0.3530	0.75
3	18.6	0.5957	0.0924	0.1285
4	18.6	0.4886	0.2246	0.25
5	18.1	0.1981	0.0132	0.1340
6	16.2	0.3333	0.6667	0.8763
7	15.2	0.1193	0.1201	0.25

Moreover, peak 7 at HAp: Se3 was explicitly observed from the difference Fourier maps of HAp:Se3 and distinguished from those of HAp. Residing near OH channel, the position of peak 7 was also considered to be associated with the oxygen atom in CO_3^{2-} structure. In particular, the bond distances between this oxygen and its mirror-symmetry (O3 and O3') in phosphate tetrahedral were computed as 2.2476(1)Å while the distance between the symmetric oxygen atoms were computed as 2.4478(1)Å. Also, the resultant bond angles were obtained as 65.98° and 57.01° indicating that the oxygen atoms connected to the oxygen at peak 7 were just near O3 atoms but no restraint were considered for the further refinement of these oxygen atoms as the bond analyses resulted in approximate distances and angles near the phosphate tetrahedra.

In the crystal structure of HAp:Se3, Se oxyanions were considered to belong to mirror symmetry and site in the octahedral holes between Ca (I) ions. The calculated bond lengths (Se-O) and angles (O-Se-O) are 1.7037(1)Å and 96.26(0)° respectively. These results almost correlates with the average bond lengths and angles of SeO_3^{2-} ions in the previous reports[99,101,102]. Accordingly, the atomic positions of Se can be referred to the positions in peak no. 6 for HAp:Se3.

Finally, the positions of Na^+ ions in the crystal structure of HAp:Se3 were attributed to the estimated position of this atom at Ca(II) site as their residual scatterings at this site were well-matched with the ionic radius of Na^+. However, as the chemical composition analyses indicated no sodium species, the position of Na atom was preferentially not included into the atomic set for HAp:Se3. Accordingly, all site occupancies and atomic positions except hydrogen atom were further refined after implementing the considered modifications for the atomic positions.

The final refinement of atomic parameters was indicated in Table 3-8 and the relevant crystal structure of HAp is given in Figure 3-18. According to the results, the atomic ratios of Ca/P and Ca/(P+Se) for HAp and HAp:Se3 were obtained as 1.73 and 1.66, respectively. However, considering the incorporated CO_3^{2-} extent in HAp, the calculated ratios were adjusted as 1.55 and 1.46 which are rather similar to atomic ratios obtained by the chemical analyses. Evaluating the unit cell contents of ionic species within HAp, it was observed that sum of site occupancy of carbonate and Ca atoms approximately near to 1. Thus, the main reason for Ca^{2+} deficiency in HAp structure can be related to CO_3^{2-} ions accommodated near the phosphate tetrahedra. Also, the calculated atomic positions of C and O atoms in carbonate structure was consistent with the reported results and confirmed B-type carbonation[40,78]. Atomic arrangement of CO_3^{2-} ions around PO_4^{3-} tetrahedral is indicated in Figure 3-19.

Proposed crystal structure of HAp:Se3 and arrangement of SeO_3^{2-} and CO_3^{2-} ions are shown in Figure 3-20 and Figure 3-21 respectively. As for the atomic parameters in HAp:Se3, Ca/(P+Se) ratio of 1.46 can be mainly attributed to highly decreased occupancies at P sites. Unlike HAp, no clear compositional relation was obtained from Rietveld refinement; however, lowered site occupancy in the position of Ca^{2+} ions can be attributed to Ca-deficient structure of synthesized powders itself and related to maintaining charge neutrality due to carbonate and selenite ions. Also, atomic percent of Se/P ratio was obtained close to 1.45 which is roughly half of the average Se/P of 2.67 obtained by the chemical analysis. This result supports that amorphous shells forming on the surface of HAp crystallite also have an effect on composition of Se oxyanions at the surface of HAp crystallites. Although the previous reports upon sorption of selenite ions on HAp claim the ion exchange mechanism occurring upon Se sorption, nanosized crystallites were considered to trigger surface complexation model in this study[79,95].

Table 3-8 Structural parameters of HAp and HAp:Se3. Atomic displacement parameters kept constant during the refinements.

	Equi-point	**F**	**x**	**y**	**z**	U_{iso}
HAp						
Ca1	4f	0.935(4)	0.3333	0.6667	0.0013(4)	0.0053
Ca2	6h	0.926(4)	0.2452(2)	0.9896(3)	0.2500	0.0048
P	6h	0.896(9)	0.3989(4)	0.3696(4)	0.2500	0.0030
O1	6h	0.896(9)	0.3319(5)	0.4898(5)	0.2500	0.0066
O2	6h	0.896(9)	0.5885(6)	0.4682(6)	0.2500	0.0106
O3	12i	0.896(9)	0.3452(4)	0.2601(6)	0.0713(8)	0.0124
O-H	4e	0.496(9)	0	0	0.186(1)	0.0133
H	4e	0.5	0	0	0.0608	0.025
Oa	6h	0.104(9)	0.3303(5)	0.4850(5)	0.2500	0.012
Ob	6h	0.104(9)	0.5561(6)	0.4410(6)	0.2500	0.012
Oc	12i	0.052(4)	0.3266(6)	0.2713(8)	0.0944(7)	0.012
HAp:Se3						
Ca1	4f	0.791(2)	0.3333	0.6667	0.0013(6)	0.0053
Ca2	6h	0.789(2)	0.2410(3)	0.9847(3)	0.2500	0.0048
P	6h	0.781(1)	0.3994(4)	0.3683(3)	0.2500	0.0030
O1	6h	0.825(2)	0.3308(7)	0.4929(7)	0.2500	0.0066
O2	6h	0.825(1)	0.5852(8)	0.4632(8)	0.2500	0.0106
O3	12i	0.825(2)	0.3470(4)	0.2611(5)	0.0754(4)	0.0124
O-H	4e	0.451(2)	0	0	0.181(1)	0.0133
H	4e	0.5	0	0	0.0608	0.025
O-p2	6h	0.061(6)	0.3884(7)	0.3530(7)	0.7500	0.012
O-p9	6h	0.044(5)	0.1193(5)	0.1201(5)	0.2500	0.012
Se	4f	0.017(3)	0.3333	0.6667	0.8763	0.0030

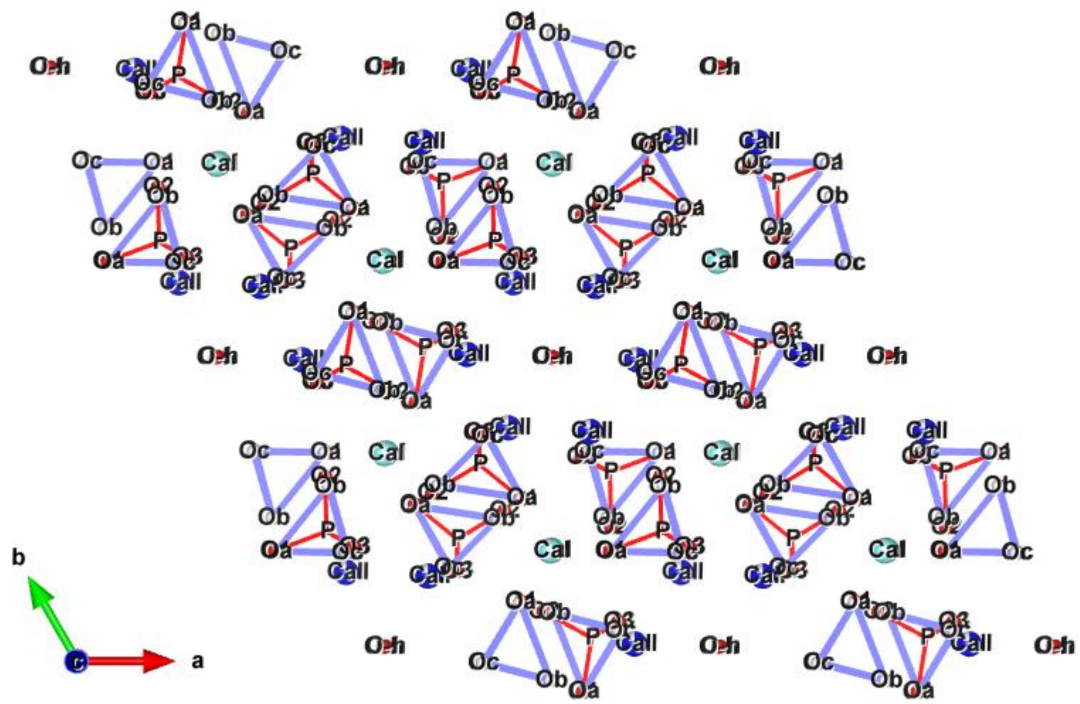

Figure 3-18 Crystal structure of B-type carbonated HAp showing P—O bonds (red lines), and O—O bond in carbonate (blue lines).

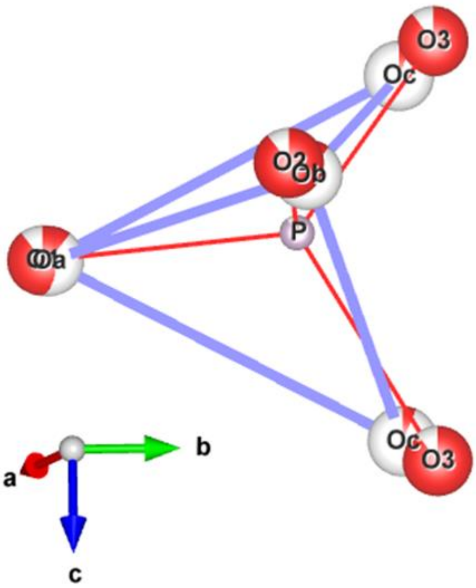

Figure 3-19 Estimated accomodation of the carbonate ions around phosphate tetrahedra in HAp.

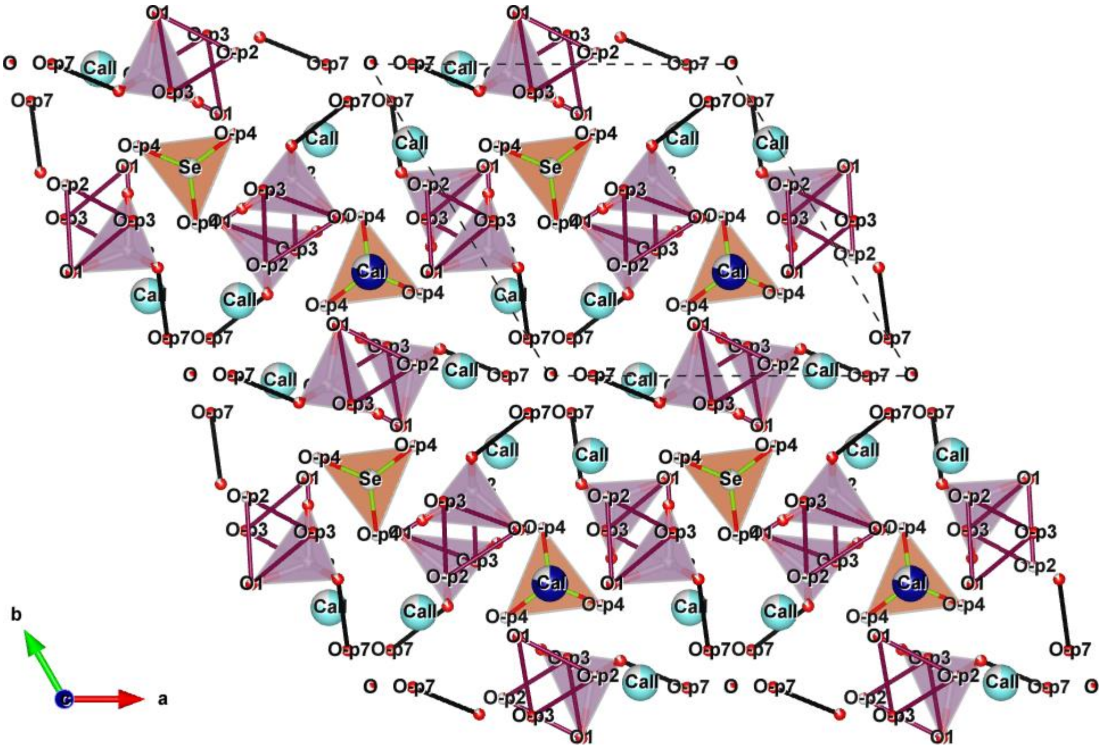

Figure 3-20 Crystal structure of B-type carbonated HAp:Se3.

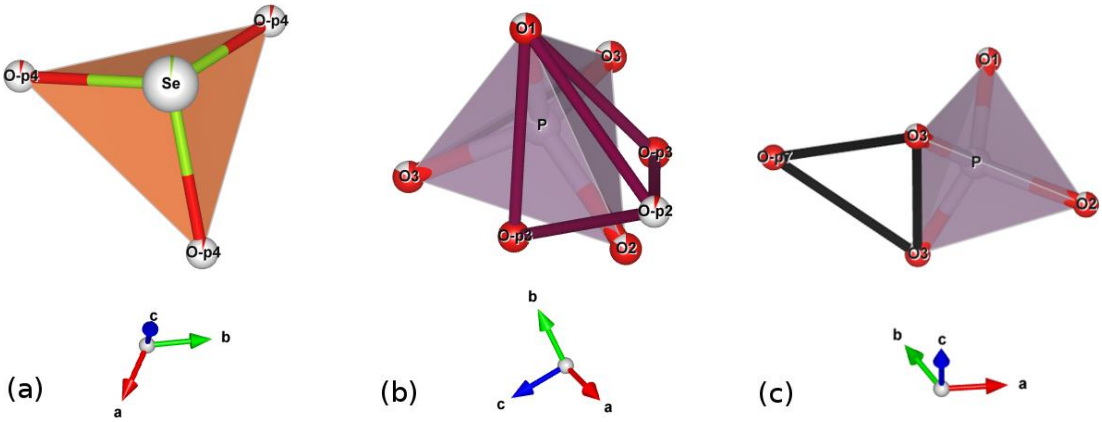

Figure 3-21 Location of B-type CO_3^{2-} ions and SeO_3^{2-} ions in the crystal structure of HAp:Se3.

Furthermore, the weight percent of B-type carbonate ions through the composition of the oxygen ions in carbonate structure were calculated as 4 % and 4.5 % for HAp and HAp:Se3 respectively. These results were compared to the estimated carbonate contents calculated by the following formula described by LeGeros[103]

$$a \text{ (nm)} = (0.9442 \pm 0.0014) - (6.3 \pm 1.0) \text{ x } 10^{-4} \text{ [wt\% } CO_3^{2-}\text{]} \qquad (2)$$

The calculated carbonate contents according to formula (2) resulted in 2.9 % and 4.25 wt. % carbonate ions for HAp and HAp:Se3, respectively. Carbonate content in pure HAp calculated by the composition of atoms and lattice parameter in a-axis can be interpreted close to one another (4% *vs* 2.9%). Similarly, for HAp:Se3, the calculated weight percent of B-type carbonate using the compositions of carbonate oxygen was about 4.5 % that is even closer to the carbonate content of 4.25 wt. % calculated by formula (2). However, ambiguity of Se ion position in HAp:Se3 structure and positions of carbonate ions near O(3) in phosphate tetrahedra needs further confirmation and suggest more detailed analyses on HAp:Se3 crystal structure.

3.5.2 Analytical studies on synchrotron XRD patterns of HAp:Se3

In this part, the structural parameters of HAp:Se3 obtained in Section 3.5.1 extracted from XRD data were further investigated through synchrotron XRD data for comparative analyses of them, meanwhile, additional features in the structural parameters including the residual electron densities in DELF maps have been obtained. Full profile refinement plots of synchrotron XRD diffractograms were indicated for HAp:Se3 in Figure 3-22 and show well-matched observed and calculated plots. Final residuals including wR, Chi**2 and GOF were obtained as 3.784%, 2678.2 and 0.9, respectively. Importantly, the wavelength of 0.4133 Å as synchrotron radiation source enhanced the resolution of the XRD pattern explicitly leading to more distinguishable peaks near the highest diffraction peaks of HAp (JCPDS: 09-0432).

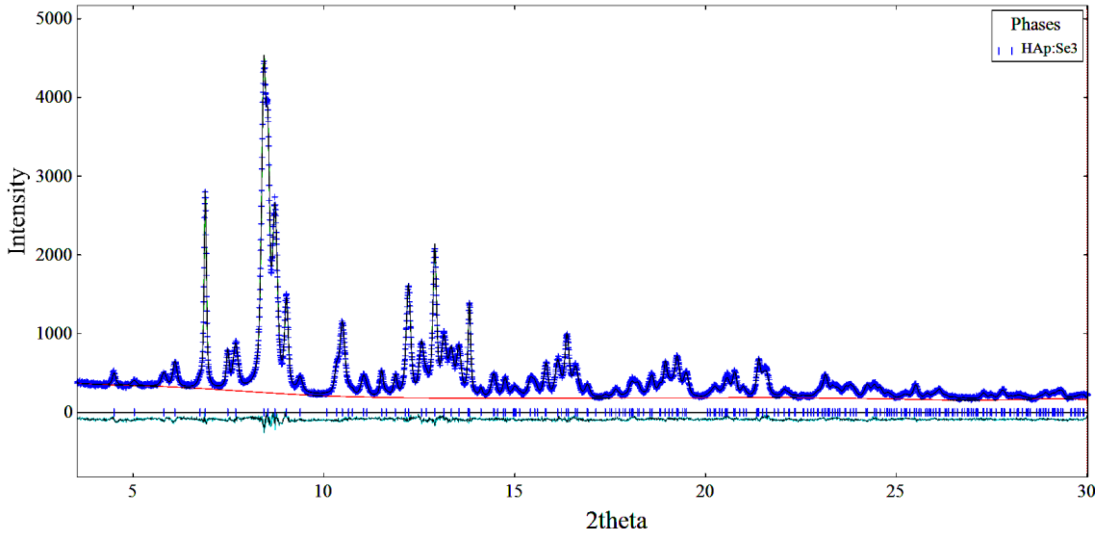

Figure 3-22 X-ray powder diffraction patterns of HAp:Se3 using synchrotron radiation source and whole pattern refinement of corresponding pattern through Rietveld method.

The refined crystallite sizes and microstrains are presented in Table 3-9. The calculated densities and crystallite sizes were almost the same with one another, the microstrain values from synchrotron XRD diffractograms were observed to be slightly different and obey more isotropic model even if the uniaxial model was selected for the refinement. Also, the calculated lattice parameters in Table 3-9 exhibited small differences in a-axis of HAp:Se3. The small changes in lattice parameters and microstrain were considered to be interrelated to one another like in 3.5.1. These changes can be attributed to the differences in the diffraction angle ranges in that the refinements on synchrotron XRPD pattern were completed for much wider diffraction angle ranges using much shorter wavelength sources (λ= 0.4133Å). Consequently, calculations of lattice parameters and cell volumes were considered to be much more reliable due to significantly lowered systematic errors on synchrotron XRD data.

Table 3-9 Comparison of peak profile and cell parameters as well as final residuals for HAp:Se3.

Samples		**HAp:Se3 (Synchotron XRD)**	**HAp:Se3 (conventional XRD)**
R_{wd}		4.10	3.41
Density (g/cm^3)		3.082	3.039
Crystallite Size (nm)	*Equatorial*	15.1(1)	14.4(1)
	Axial	33.4(1)	31.9(3)
Mustrain (μstrain)	*Equtorial*	4.6(1)e3	6.5(3)e3
	Axial	3.3(1)e3	2.0(1)e3
Lattice parameter (Å)	*a*	9.4166(1)	9.4152(3)
	c	6.8744(1)	6.8745(2)

Following the refinement of peak profile terms, structural parameters were individually refined. Based on the initially refined atomic positions and displacement factors, the obtained plot of DELF maps were shown in Figure 3-23. The plots basically showed that high residual electron densities were observed near and between phosphate tetrahedra at high contour levels in DELF maps. Also, some residual electron scatterings near Ca(I) and Ca(II) sites were observed.

Fourier peak positions associated with the highest residual densities were tabulated in Table 3-10. For convenience, peak numbers were denoted as peak 1 to peak 7 in the text. In all fourier peaks analyses, the residual electron densities of C was not considered due to their very low residual densities. Thus, the position of O ions were mainly investigated for determination of incorporated CO_3^{2-} ions. The fourier map peaks of peak 1, peak 2 and peak 6 were all considered to be associated with CO_3^{2-} ions around and between PO_4^{3-} tetrahedra. Specifically, all of these positions were attributed to residuals of O ions as the calculated bond distance and angles related to these positions were well correlated with the geometry of oxygen ions in calcite structure (O—O distance: 2.248Å) reported in the previous studies[78,99,104].

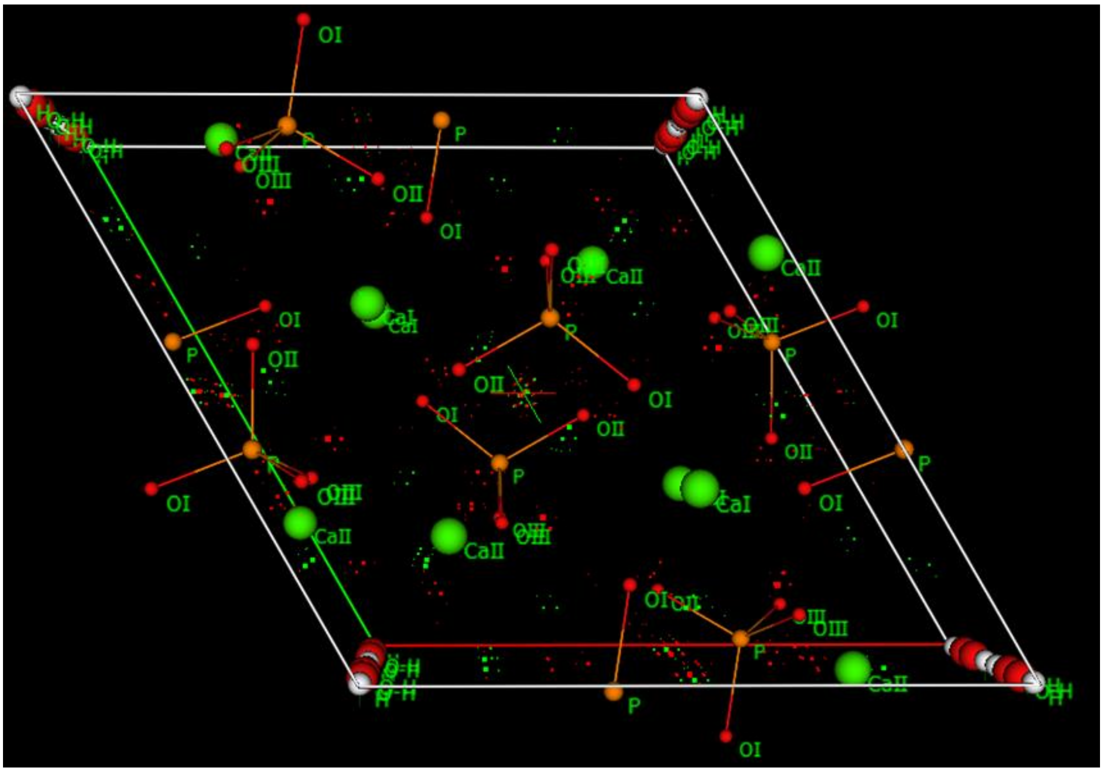

Figure 3-23 Arrangement of the constituent ions (balls), interionic bonds (sticks) and residual electron densities in DELF maps (dotted regions) were shown in HAp:Se3 uint cell. Note that there is low residual electron densities near PO_4^{3-} tetrahedra and Ca^{2+} ions.

Table 3-10 DELF map peaks obtained by the refinement of synchrotron based XRD pattern of HAp:Se3.

Peak No.	**HAp:Se3**			
	Rho	x	y	z
1	0.3007	0.6458	0.8958	0.50
2	0.2713	0	0.50	0.125
3	0.2654	0.1875	0.1875	0.6250
4	0.2463	0.6667	0.3333	0.0938
5	0.2409	0	0	0.3438
6	0.2270	0.2292	0.6250	0
7	0.2256	0.4792	0.25	0.50

The resultant bond length and angle analyses of the fourier peak positions as well as P and O atoms in phosphate tetrahedra were listed in Table 3-11. It was observed that the bond distances between peak1-peak2 were calculated relatively longer than the other bonds in CO_3^{2-}structures. This result can be attributed to the double bonding of C atoms with O ions positioned at peak 6. Important deduction from these bond analyses was that ionic groups of CO_3^{2-} triangles were linked with one another by O atom in peak 2 positions as shown in Figure 3-24 and Figure 3-25 (c, d). Moreover, the bond distances between P and O atoms were in accordance with the reported values[35]. Yet, compared to P—O(I) bond distances in the previous studies (near 1.537Å), the calculated P—O(I) bond distances (1.567Å) were slightly increased. This difference was mainly attributed to the O ions in carbonate structure the positions of which are just around the O(I) thereby affecting the distances between P—O(4) bonds.

Table 3-11 Selected bond distances and angles (Å, °) from the fourier map peaks of the synchrotron XRD diffractograms of HAp:Se3. Carbonate structures were constructed by the positions of p1, p2 and p6 while the bond analyses between p4 and p8 were attributed to selenite structure.

O(p1)—O(p2)	*2.221(1)*	*O(p2)—O(p1)—O(p6)*	*57.63(7)*
O(p1)—O(p6)	*2.039(1)*	*O(p1)—O(p2)—O(p6)*	*56.73(6)*
O(p2)—O(p6)	*2.060(1)*	*O(p1)—O(p6)—O(p2)*	*65.63(7)*
P-O(4)	*1.567(3)*	*Se(p4)-O(p8) (x3)*	*1.662(3)*
P-O(5)	*1.538(3)*	*O(p8)-O(p8)*	*2.653(2)*
P-O(6) (x2)	*1.531(3)*	*O(p8)-Se(p4)-O(p8)*	*105.92(6)*

Further analyses on the positions of the Fourier map peaks suggest that Se ions were most probably locating at peak4 positions and bonded with O ions at the positions of peak 7. These results were also similar to the obtained results through laboratory based XRD patterns in 3.5.1. Important consideration about this selenite structure was that the bond distances between Se and O ions were equal to one another due to the rotational symmetry of peak 7 positions that leads to exactly equal distances from peak 4. Although selenite structure is actually consisted of one double bonds and two single bonds the magnitudes of which show slight differences. Table 3-11 showed that the calculated bond distances and angles associated with the considered selenite structure were well correlated with the reported geometric values[101,102]. Therefore, similar to the addition of Se position in atomic set described in 3.5.1., Se atom was included into atomic position set.

Out of the remaining the Fourier peak positions, peak 3 was considered to locate near Ca(2) but its inclusion did not lead to enhanced convergence in the refinements. Similarly, the position attributed to peak 5 was seen to locate along OH channel and evaluated to be oxygen impurity just near O(O-H) ions. Compositional calculations based on the constraint between O(OH) and peak 5 did not result in any considerable values. Thus, both peak 3 and peak 5 were not included in atomic position set.

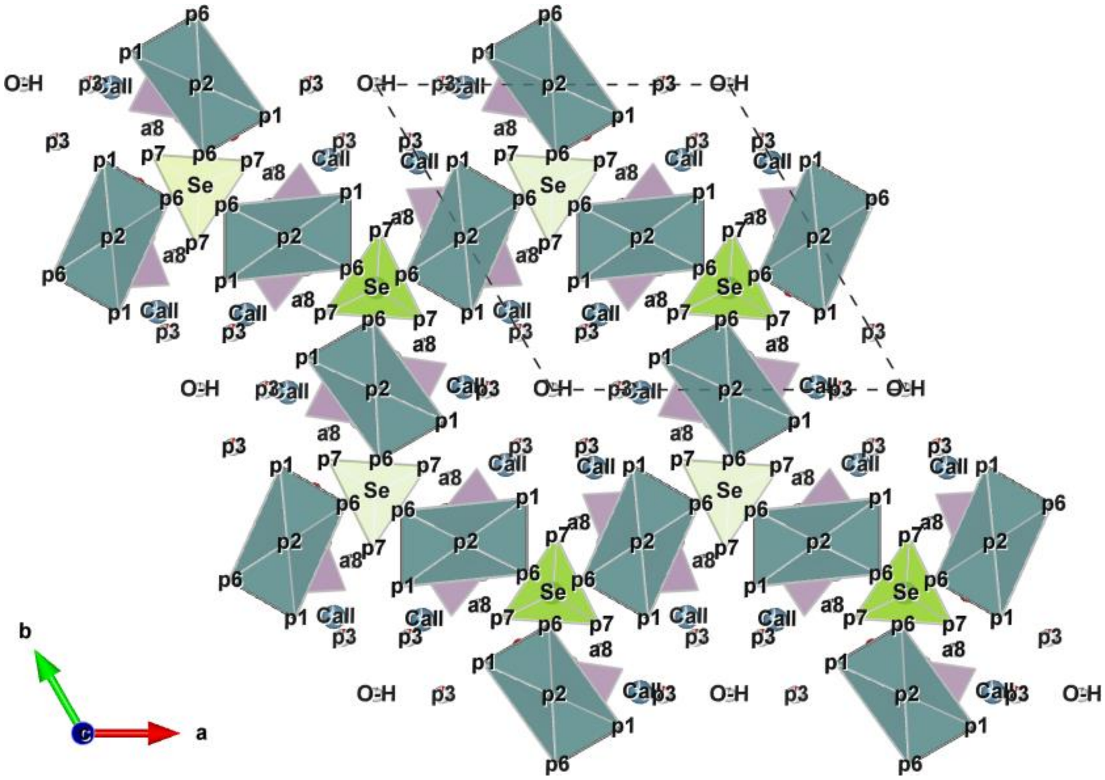

Figure 3-24 Proposed crystal structure and the representative unit cell of HAp:Se3. The fourier peak positions (p1, p2, p6 and p7) were attributed to ionic species of oxygen.

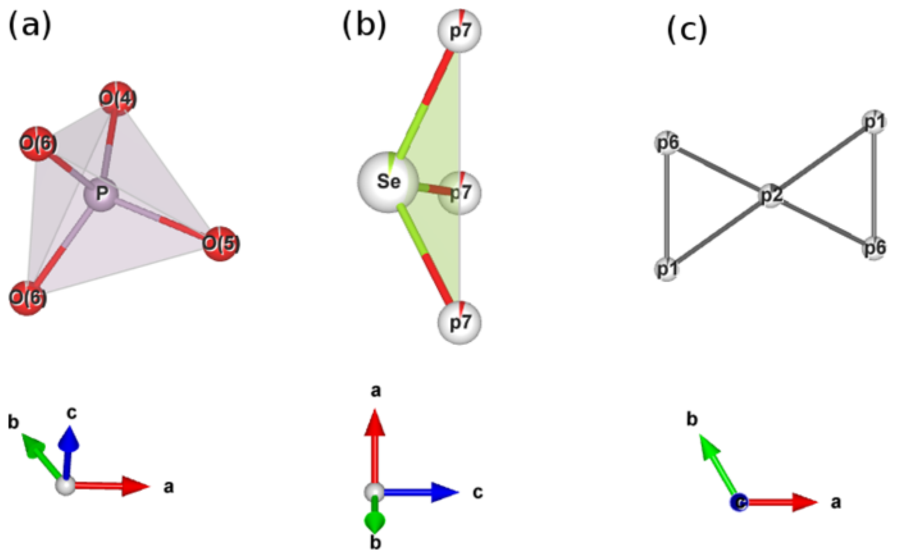

Figure 3-25 Representative images of phosphate tetrahedra (a), estimated selenite structure (b), arrangement of B-type carbonate (c).

It is worth noting that, during the refinement of structural parameters, ADPs of O(p1), O(p2) and O(p6) atoms were not refined and held constant at the values of 0.012. Similary, due to high divergence of the residuals, ADP of Se(p4) ionwas fixed at 0.01 considering the reported ADPs values for Se atoms in selenite and selenate structures[101,105]. The ADPs of the remaining atoms were also held constant as regards to the values of the atoms in holly springs HAp structure[77]. In addition, site occupancy of O(p1), O(p2) and O(p6) ions were constrained to be equivalent as their composition were required to be equal to one another for the suggested carbonate ion structure. Lastly, the positions of O(p1), O(p2) and O(p6) atoms were not refined as their exact position was determined through Fourier maps peaks. None of atomic parameters of H atom was refined as well. After these constraints, the atomic positions and site occupancies were refined individually at the beginning and all refined simultaneously in the end.

Analyses on the final atomic positions show that z-position of O(III) were seen to change slightly when compared to the results of that in section 3.5.1. These changes can be attributed to the suggested carbonate ion model in that the low residual densities near O(III) atom can lead to shifting in the position of O(III). The remaining atomic positions were obtained in reasonable ranges with the ones in section 3.5.1 and reported values in previous studies[35,40]. One of the important result in Table 3-12 is that the atomic percent of Se/P ratio was calculated as 0.76 % that is approximately half of the computationally calculated Se/P ratio (1.45 %) in section 3.5.1 and near one third of the chemically obtained Se/P ratio (2.67 %). This result confirm that relatively low amount of Se ions are present in the crystal structure of HAp:Se3. Also, Ca/(P+Se) ratio was calculated as 1.67 that is very close to stoichiometric HAp. Again, considering extent of B-type CO_3^{2-} in HAp:Se3, adjusted Ca/(P+Se) ratio was obtained as 1.49. Thus, both lab-based and synchrotron based models can be considered to be accurate in description of the crystal structure of HAp:Se3.

Table 3-12 Atomic positions, occupancies and the resultant compositions values of HAp:Se3 structure obtained by synchrotron based XRD pattern refinements.

	Equi-point	**F**	**x**	**y**	**z**	**U_{iso}**
Ca(I)	4f	0.935	0.3333	0.6667	0.0055(3)	0.0053
Ca(II)	6h	0.960	0.2441(2)	0.9906(2)	0.2500	0.0048
P	6h	0.943	0.3983(2)	0.3707(2)	0.2500	0.0030
O(I)	6h	0.943	0.3293(4)	0.4869(4)	0.2500	0.0066
O(II)	6h	0.943	0.5885(4)	0.4642(4)	0.2500	0.0106
O(III)	12i	0.943	0.3427(3)	0.2584(3)	0.0736(3)	0.0124
O(OH)	4e	0.439	0	0	0.198(13)	0.0133
H	4e	0.500	0	0	0.0608	0.025
Se	4f	0.014	0.6667	0.3333	0.0938	0.012
O(p1)	12i	0.057	0.06458	0.8958	0.5	0.012
O(p2)	12i	0.057	0	0.5000	0.1250	0.012
O(p6)	12i	0.057	0.2292	0.6250	0	0.012

The weight percent of CO_3^{2-} ions were also calculated by the proposed formula by LeGeros[103] described at the end of section 3.5.1. Using the composition of O atoms attributed to carbonate structure in Table 3-12, carbonate percent was calculated as 4.11 %. Using the formula (2) in 3.5.1, that shows the relationship between the lattice parameter in a-axis and the carbonate content, weight percent of carbonate ions were also calculated as 4.13 %. Thus, well-matched correlation between these CO_3^{2-} amount suggest that formula (1) can be used for the comparing the relative weight percent of carbonates and indicate that very small effect of Se ions on lattice parameters of HAp.

It is important to point out that that obtaining high accuracy in the carbonate content through structural refinements of HAp:Se3 also leads to more accurate calculation of the selenium composition as well. Therefore, further calculations of carbonate content in HAp and HAp:Se samples through empirical ways will be further discussed within next chapter during the analyses of heat treated HAp and HAp:Se3 samples.

3.6 Analyses on the high temperature stability of Se oxyanions in HAp

High temperature stability of CO_3^{2-} and SeO_3^{2-} ions at the typical calcination temperatures (700°C-1000°C) usually applied for HAp precipitates have been investigated in this part. The experimental procedure explained in section 2.2 was considered for the synthesis of as-calcined HAp and HAp:Se powders. Afterwards, the thermal analyses (TGA) and FTIR analyses were carried out to identify the temperature ranges in which Se-related species remain stable in HAp structure.

Thermal decomposition behavior of the constituent ionic species in HAp and HAp:Se samples were investigated through TGA, DTG and DTA analyses. As for thermal behavior of HAp, Figure 3-26 shows that the decomposition of constituent ions in HAp structure was clearly observed by the distinguishable DTG peaks. Specifically, the DTG peaks at near 110°C indicates the removal of adsorbed water while those at near 210°C and 390°C was mainly attributed to the removal of structural water. Since most of the structural water was eliminated by 400°C, the changes from 400°C to 1100°C can be predominantly attributed to the removal of carbonate species. In particular, close peaks between 390-430°C can be associated with rearrangement of carbonate species from near-tetrahedral sites to OH channels based on the calculated lattice parameter changes declared in a previous study[35]. Therefore, after 430°C, the change in weight loss in TGA curve of HAp was wholly attributed to the removal of carbonate ions for HAp. Also, the removal of carbonate was considered to end at 1025°C that corresponds to the maximum rate of weight loss in DTG.

DTA results indicated the decompositions of HAp:Se samples between 700°C and 1000°C (in Figure 3-27, Figure 3-28 and Figure 3-29). That was not explicitly seen in the thermal analyses curves for HAp in Figure 3-26. Similarly, the TGA curves of HAp:Se samples showing changes in slope of weight loss for this temperature range. These changes can be most likely related to the removal of selenite ions from both surface and bulk of HAp but it was not possible to separate surface and bulk changes. Additionally, small peak observed in DTA curves of HAp:Se after 1025°C can be attributed to the formation of CaO that is generally observed to be a secondary phase between 1000°C -1100°C. Other than these alterations in thermal analyses curves, similar remarks on thermal behavior of HAp:Se and HAp can be made for the temperatures before 700°C.

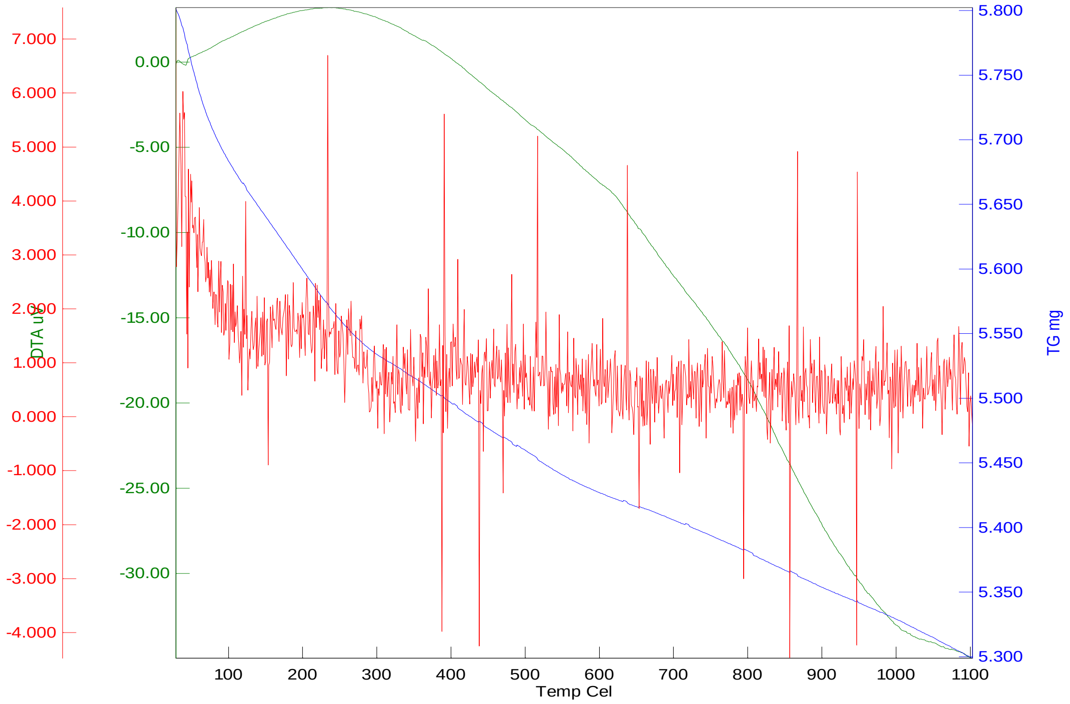

Figure 3-26 TGA, DTA and DTG curves for pure HAp.

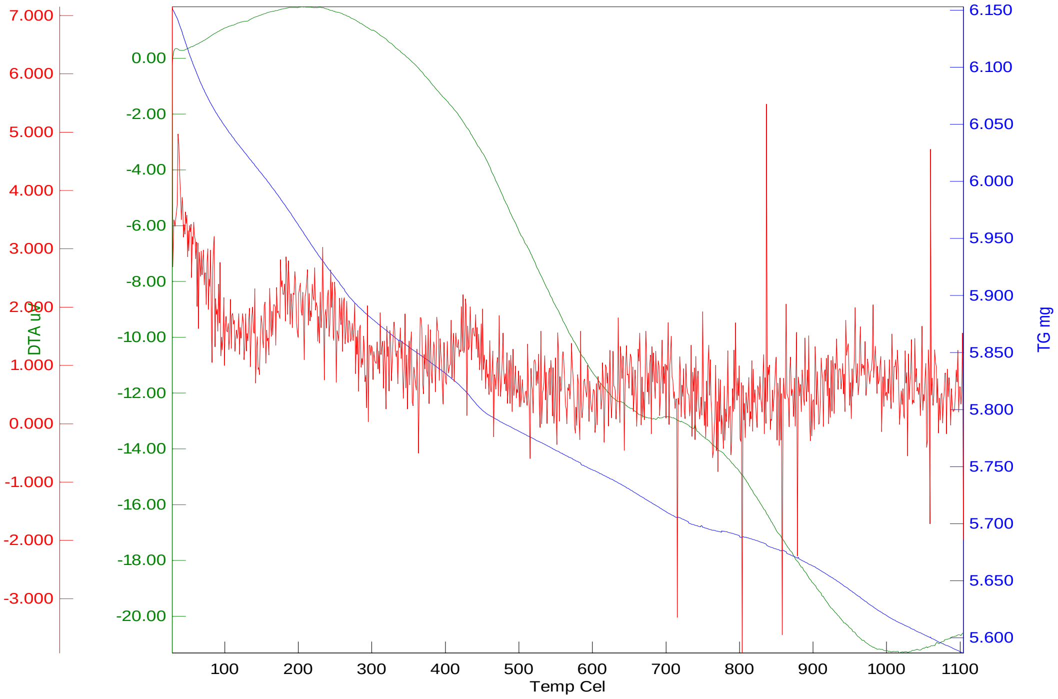

Figure 3-27 TGA, DTA and DTG curves for HAp:Se1.

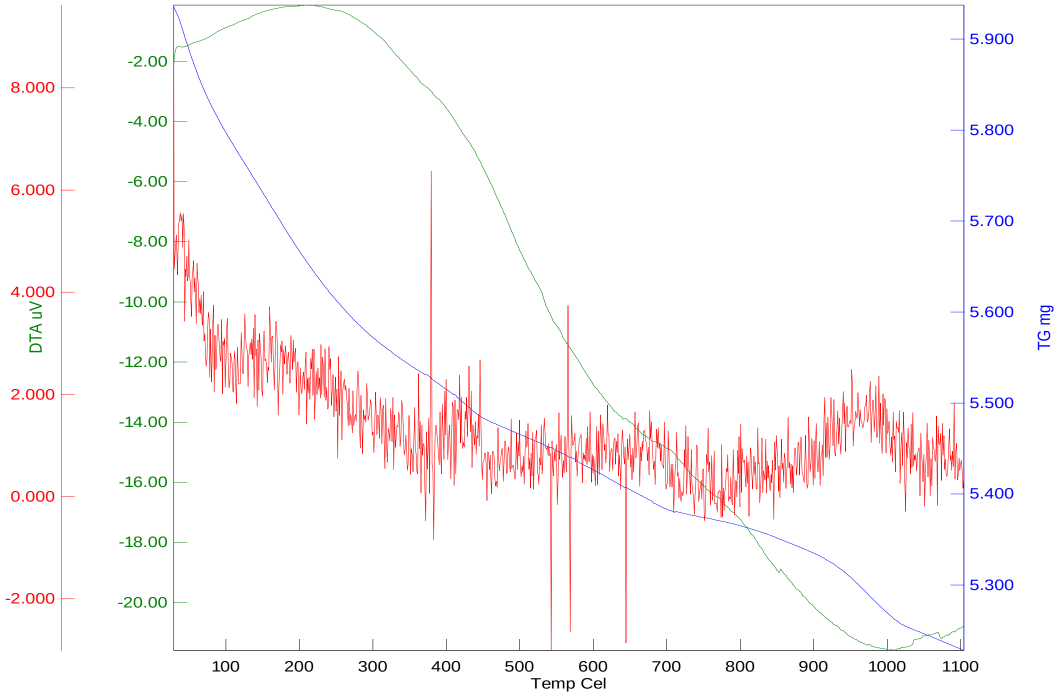

Figure 3-28 TGA, DTA and DTG curves for HAp:Se2.

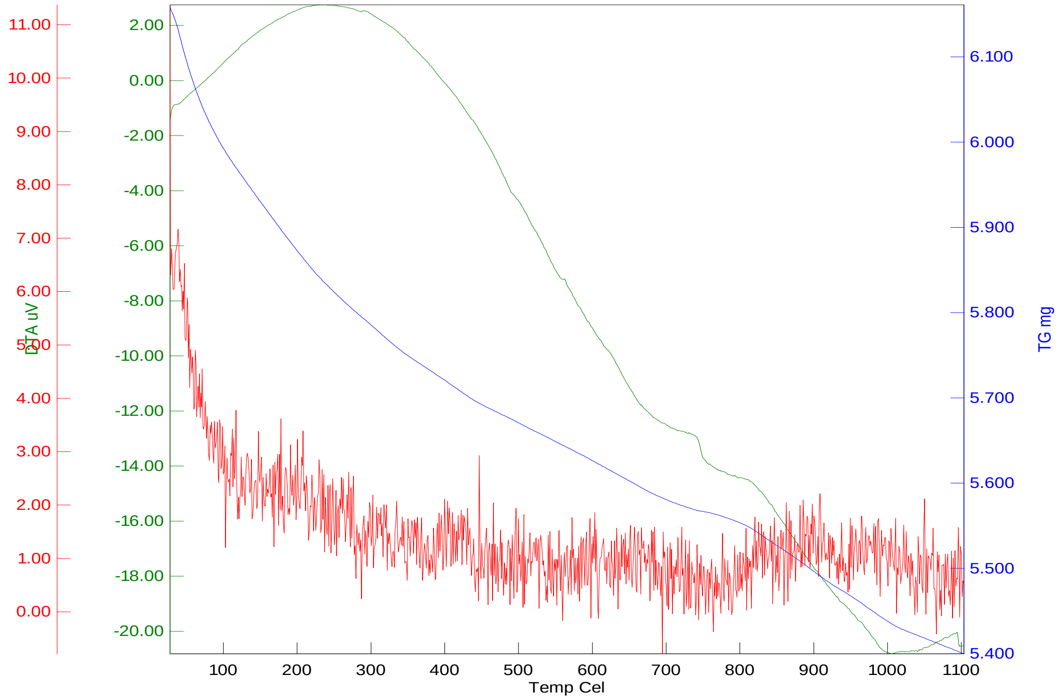

Figure 3-29 TGA, DTA and DTG curves for HAp:Se3.

Total carbonate and selenite contents were quantitatively determined considering that the removal of them occured in the temperature ranges 430°C- 1025°C. Their results as well previously calculated lattice and surface carbonate contents were given in Table 3-13. Clearly, the total weight loss in HAp:Se was observed to be higher than HAp and was attributed to the loss of bulk and surface selenite ions. Although the lattice and surface carbonate content were not consistent with one another, the range of carbonate content near 3-5 % was well-suited with the carbonate content of human dental apatites.

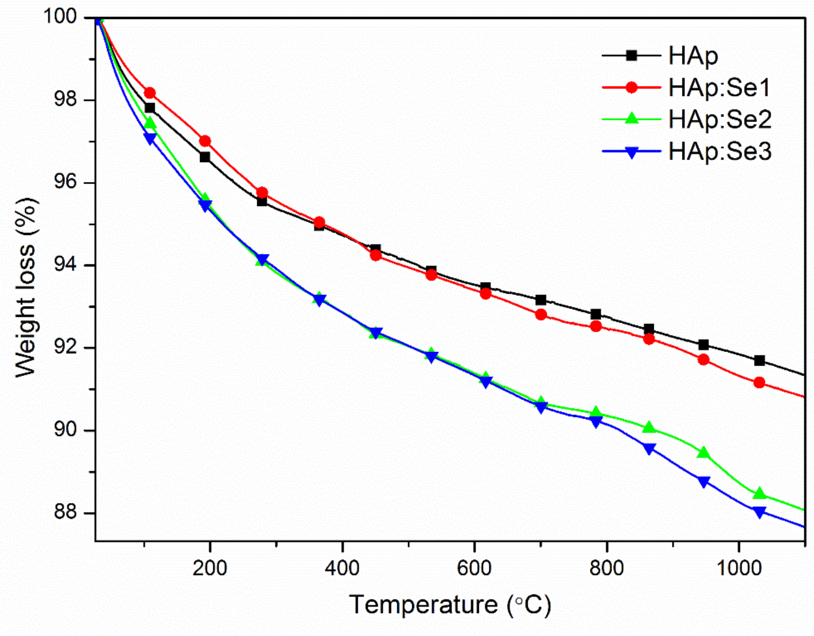

Figure 3-30 Normalized TGA curves indicating the weight loss percent for each sample upon heating up to 1100°C.

Table 3-13 B-type carbonate, surface carbonate and total carbonate, including selenite for HAp:Se as well, contents (430°C-1025°C) as regards to corresponding characterization tecnhniques.

	FTIR	XPS	TGA
	Lattice carbonate (wt %)	Surface carbonate (wt %)	Total carbonate & selenite (wt %)
HAp	3.99	1.16	2.95
HAp:Se1	3.26	1.71	3.49
HAp:Se2	5.68	1.67	4.38
HAp:Se3	4.86	2.08	4.83

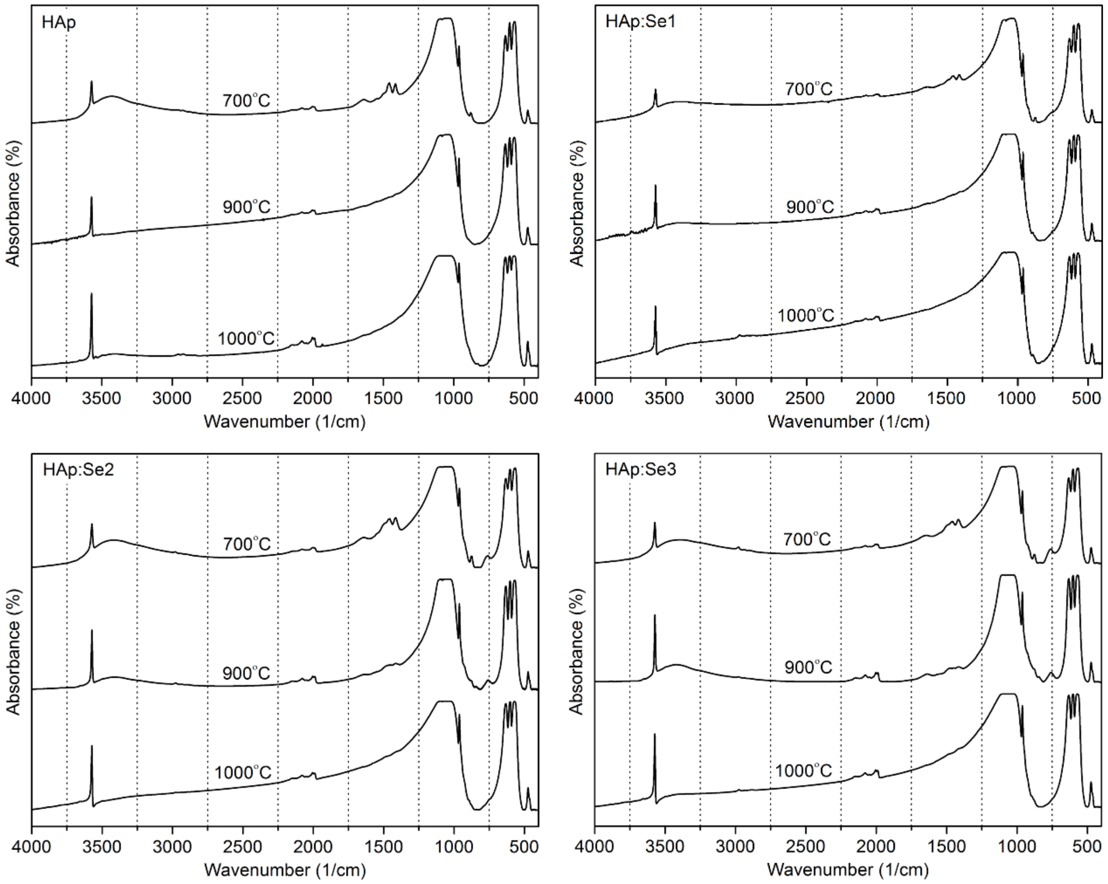

Figure 3-31 Infrared spectra of all samples exhibiting changes in the absorption bands of the functional groups after the calcination process at 700°C, 900°C and 1000°C.

Finally, the temperature ranges where the selenite ions were considered to be removed from HAp:Se were investigated using the infrared spectra data given in Figure 3-31. The most distinguishable changes about infrared spectra were increased intensity of OH$^-$ bands and disappearences of CO$_3^{2-}$ ions upon heating from 700°C to 900°C Specifically, B-type carbonate ions were associated with the peaks near 1415 cm^{-1}, 1457 cm^{-1} and 1467 cm^{-1}[89]. Heating to 1000°C clearly vanishes the abovementioned carbonate peaks.

Furthermore, the very small bands at around 760 cm^{-1} and 842 cm^{-1} were attributed to the selenite structure based on the previous study[92]. In particular, the positive shifts of these two bands, about wavenumber of 2 cm^{-1}, were observed with increased calcination temperatures from 700°C to 1000°C. At around 900°C, most of the selenite-related peaks disappeared although small residual bands for HAp:Se2 an

HAp:Se3 can still be distinguishable at this temperature. These results show that the calcination ranges in 700°C -900°C can be reasonable one for obtaining low carbonate and sufficiently high selenite content in HAp. Therefore, selenite-related therapeutic effect for HAp nanoparticles can be more prouncedly achieved by calcining the particles at the suggested temperatures.

CHAPTER 4

CONCLUSIONS

HAp and HAp:Se nanoparticles were synthesized by the precipitation method using appropriate inorganic precursors. Se-incorporation into HAp was achieved during the synthesis and were analyzed with different complementary characterization techniques in order to comprehend extend and accommodation of Se-related species in the surface and the crystal structure of HAp. The general results of this thesis based on characterization methods can be stated as followings;

Chemical and morphological analyses of HAp and HAp:Se nanoparticles

Chemical analyses through EDS show that Se-related ionic species well incorporated into HAp as Se/P ratios were obtained similar to initial ratio of Se/P. Also, Ca/(P+Se) ratios were generally obtained near 1.5 but HAp:Se particle have slightly decreasing Ca/(P+Se) ratios that are attributed to low crystallinity of HAp:Se particles. Overall, Ca/P ratio of 1.5 indicates that as-synthesized particles have calcium-deficient HAp structure. Chemical structure analyses through FTIR techniques enlightened B-type CO_3^{2-} ions in the crystal structure of HAp. Also, Se-related species were associated with SeO_3^{2-} ions as the absorption band of these ions were observed in the infrared spectrum. Se-incorporation was also related to increasing extend of adsorbed and structural water in HAp.

Surface chemistry of HAp and HAp:Se particles were elaborated in that CO_3^{2-} and SeO_3^{2-} ions accommodate in the top surface of HAp:Se particles. Also, the calculated ratio of Ca/(P+Se) at surface of HAp:Se was significantly lower than those at the bulk region of HAp:Se. Therefore, Se incorporation was considered both in surface and crystalline region of HAp thereby possible affecting release kinetics of Se in HAp:Se particles. In addition, Auger peaks obtained in XPS spectra of HAp:Se suggest that extent of Se at the surface of HAp:Se enhance with increasing concentration of Se precursors used in the synthesis.

Morphological analyses of HAp and HAp:Se were also critical and observed to correlate with the results of chemical analyses. Specifically, the obtained nanoparticles of HAp and HAp:Se were observed to have rather similar dimensions to those of natural bone mineral and have anisotropic crystallite form. Low crystalline surface region (1-2 nm) in HAp:Se was attributed to the region where SeO_3^{2-} ion accommodate at the surface of HAp:Se.

Structural and thermal analyses of HAp and HAp:Se nanoparticles

Whole structural analyses were carried out using both lab-based and synchrotron based XRD diffractograms of HAp and HAp:Se. The findings indicate that Se incorporation decreases crystallite size and increase the strain build-up of HAp nanoparticles. Especially, surface accommodation of SeO_3^{2-} was considered to hinder growth of HAp crystallites leading to extra negative charge on HAp surface. In addition, incorporation of SeO_3^{2-} was shown to trigger decreasing lattice parameters of HAp with increasing extend of Se.

Positions of CO_3^{2-} and SeO_3^{2-} ions in the crystal structure of HAp were then attempted to determine the composition of these ions. The findings show that CO_3^{2-} ions located near PO_4^{3-} tetrahedral in pure HAp and its composition was consistent with the calculated CO_3^{2-} by the formula described by LeGeros[103]. For HAp:Se, HAp with the highest extend of Se was used to reveal the position of SeO_3^{2-} as well as CO_3^{2-}. These analyses were wholly based on the difference Fourier map calculations and bond length and angle analyses. The results suggest that SeO_3^{2-} ions possibly accommodate in near octahedral holes between Ca(I) positions. Also, CO_3^{2-} ions were proposed to locate near PO_4^{3-} tetrahedral almost similar to the location of them in pure HAp. With the considered location of SeO_3^{2-} and CO_3^{2-} ions, the ratio of Se/P in the crystal structure of HAp:Se3 was determined between nearly 0.75-1.5 depending on the model described by lab and synchrotron results. These results imply that Se incorporates mostly locate near surface region of HAp:Se as the calculated ratio of Se/P was significantly lower than the ratios obtained by chemical methods.

Finally, thermal analyses were completed to mainly understand in which temperature ranges Se-related species accommodate in HAp:Se nanoparticles. The result show that calcination between 700-900°C leads to low CO_3^{2-} and sufficiently high SeO_3^{2-} extents in HAp:Se particles. Also, it was clear from FTIR analyses of the calcined HAp:Se particles that calcination temperatures above 1000°C result in the removal of all SeO_3^{2-} and CO_3^{2-} ions and form stoichiometric HAp structure.

In summary, this study basically aimed to elucidate the underlying mechanism of Se oxyanions incorporation in HAp lattice. HAp and HAp:Se powders in as-synthesized condition, the sizes and shapes of which are highly comparable with biological apatite, are uniquely attempted to be characterized by Rietveld analyses. The result of these chemical and structural analyses showed that not only incorporated Se oxyanions within HAp lattice but also surface accommodation of them are considerably important as the surface concentration and release of Se oxyanions can be extensively critical for both healthy and cancerous bone cell responses *in vivo*. Thus, promising material-function relevance of this study should be further supported by biological tests. In addition, the crystal structure analyses with more advanced technique (such as EXAFS, PDF) and a more detailed surface characterization of HAp nanoparticles can be some other technical points that can be further explored in future studies.

REFERENCES

1. Lever, M. J. *Biomaterials, Artificial Organs and Tissue Engineering*. *Biomater. Artif. Organs Tissue Eng.* (2005). doi:10.1533/9781845690861.3.153

2. Park, J. *Hard Tissues: structure, properties, healing, remodeling, and biocompatibility. In Bioceramics: Properties Characterization and Applications. Network: Springer Science Business Media*. (2008).

3. Reznikov, N., Shahar, R. & Weiner, S. Bone hierarchical structure in three dimensions. *Acta Biomater.* 10, 3815–3826 (2014).

4. Weiner, S. & Wagner, H. D. THE MATERIAL BONE: Structure-Mechanical Function Relations. *Annu. Rev. Mater. Sci.* 28, 271–298 (1998).

5. Rho, J. Y., Kuhn-Spearing, L. & Zioupos, P. Mechanical properties and the hierarchical structure of bone. *Med. Eng. Phys.* 20, 92–102 (1998).

6. Wang, Y. *et al.* The predominant role of collagen in the nucleation, growth, structure and orientation of bone apatite. *Nat. Mater.* 11, 724–733 (2012).

7. Bilezikian, J. P., Raisz, L. G., Rodan, G. a. & Robey, P. G. Bone Matrix Proteoglycans and Glycoproteins. *Princ. Bone Biol.* 225–237 (2002). at <http://www.sciencedirect.com/science/article/pii/B9780120986521501165>[Last accessed on 02.07.2015]

8. Wilson, E. E. *et al.* Highly ordered interstitial water observed in bone by nuclear magnetic resonance. *J. Bone Miner. Res.* 20, 625–634 (2005).

9. Wilson, E. E. *et al.* Three structural roles for water in bone observed by solid-state NMR. *Biophys. J.* 90, 3722–3731 (2006).

10. Yusufoglu, Y. Synthesis and characterization of carbonated hydroxyapatite and bioinspired polymer-calcium phosphate nanocomposites. (2009). at <http://adsabs.harvard.edu/abs/2009PhDT........41Y> [Last accessed on 21.07.2015]

11. Dorozhkin, S. V. & Epple, M. Biological and medical significance of calcium phosphates. *Angew. Chemie - Int. Ed.* 41, 3130–3146 (2002).

12. Driessens, F. C. M. & Verbeeck, R. M. H. *Biominerals*. (CRC Press, 1990).

13. Tadic, D., Peters, F. & Epple, M. Continuous synthesis of amorphous carbonated apatites. *Biomaterials* 23, 2553–2559 (2002).

14. Nelson, D. The Influence of Carbonate on the Atomic Structure and Reactivity of Hydroxyapatite. *J Dent Res.* 60, 1621–1629 (1981).

15. Posner, A. S. Crystal chemistry of bone mineral. *Physiol. Rev.* 49, 760–792 (1969).

16. Tran, P. a., Sarin, L., Hurt, R. H. & Webster, T. J. Titanium surfaces with adherent selenium nanoclusters as a novel anticancer orthopedic material. *J. Biomed. Mater. Res. - Part A* 93, 1417–1428 (2010).

17. Dorozhkin, S. V. Calcium Orthophosphates as Bioceramics: State of the Art. *J. Funct. Biomater.* 1, 22–107 (2010).

18. Hench, L. L. Bioceramics: From Concept to Clinic. *J. Am. Ceram. Soc.* 74, 1487–1510 (1991).

19. Hench, L. L. Bioceramics. *J. Am. Ceram. Soc.* 28, 1705–1728 (1998).

20. Cao, W. & Hench, L. L. Bioactive materials. *Ceram. Int.* 22, 493–507 (1996).

21. Suchanek, W. & Yoshimura, M. Processing and properties of hydroxyapatite-based biomaterials for use as hard tissue replacement implants. *J. Mater. Res.* 13, 94–117 (1998).

22. Ben-nissan, B. *Advances in Calcium Phosphate Biomaterials*. 2, (2014).

23. Dorozhkin, S. V. Calcium Orthophosphates in Nature, Biology and Medicine. *Materials (Basel).* 2, 399–498 (2009).

24. Dorozhkin, S. V. Calcium orthophosphates. *J. Mater. Sci.* 42, 1061–1095 (2007).

25. Bohner, M. Calcium orthophosphates in medicine: from ceramics to calcium phosphate cements. *Injury* 4, 37–47 (2000).

26. Dorozhkin, S. Bioceramics of calcium orthophosphates. *Biomaterials* 31, 1465–85 (2010).

27. Sadat-Shojai, M., Khorasani, M. T., Dinpanah-Khoshdargi, E. & Jamshidi, A. Synthesis methods for nanosized hydroxyapatite with diverse structures. *Acta Biomater.* 9, 7591–7621 (2013).

28. Tasker, L., Sparey-Taylor, G. & Nokes, L. Applications of nanotechnology in orthopaedics. *Clin Orthop Relat Res.* 456, 243–249 (2007).

29. Dorozhkin, S. V. Biological and Medical Significance of Nanodimensional and Nanocrystalline Calcium Orthophosphates. *Biomed. Mater. Diagnostic Devices* 2, 19–99 (2012).

30. Rey, C., Hina, A., Tofighi, A. & Glimcher, M. Maturation of poorly crystalline apatites: Chemical and structural aspects in vivo and in vitro. *CELLS Mater.* 5, 345–356 (1995).

31. Schoonman, J. *et al.* Studies in Inorganic Chemistry Other titles in this series.

32. Boanini, E., Gazzano, M. & Bigi, a. Ionic substitutions in calcium phosphates synthesized at low temperature. *Acta Biomater.* 6, 1882–1894 (2010).

33. Dorozhkin, S. V. Calcium orthophosphates: occurrence, properties, biomineralization, pathological calcification and biomimetic applications. *Biomatter* 1, 121–164 (2011).

34. Elliott, J. C., Wilson, R. M. & Dowker, S. E. P. Apatite structures. *Adv. X-ray Anal.* 45, 172–181 (2002).

35. Ivanova, T. I., Frank-Kamenetskaya, O. V., Kol'tsov, a. B. & Ugolkov, V. L. Crystal Structure of Calcium-Deficient Carbonated Hydroxyapatite. Thermal Decomposition. *J. Solid State Chem.* 160, 340–349 (2001).

36. Fleet, M. E., Liu, X. & Liu, X. Orientation of channel carbonate ions in apatite: Effect of pressure and composition. *Am. Mineral.* 96, 1148–1157 (2011).

37. Tonegawa, T., Ikoma, T., Yoshioka, T., Hanagata, N. & Tanaka, J. Crystal structure refinement of A-type carbonate apatite by X-ray powder diffraction. *J. Mater. Sci.* , 45, 2419–2426 (2010).

38. Fleet, M. E. & Liu, X. Carbonate apatite type A synthesized at high pressure: new space group (P3) and orientation of channel carbonate ion. *J. Solid State Chem.* 174, 412–417 (2003).

39. Fleet, M. E. & Liu, X. Local structure of channel ions in carbonate apatite. *Biomaterials* 26, 7548–7554 (2005).

40. Wilson, R. M., Dowker, S. E. P. & Elliott, J. C. Rietveld refinements and spectroscopic structural studies of a Na-free carbonate apatite made by hydrolysis of monetite. *Biomaterials* 27, 4682–4692 (2006).

41. Vandiver, J., Dean, D., Patel, N., Bonfield, W. & Ortiz, C. Nanoscale variation in surface charge of synthetic hydroxyapatite detected by chemically and spatially specific high-resolution force spectroscopy. *Biomaterials* 26, 271–283 (2005).

42. Misra, D. N. *Adsorption on and Surface Chemistry of Hydroxyapatite*. (Springer US, 1984). doi:10.1007/978-1-4757-9012-2

43. Drouet, C. Apatite formation: Why it may not work as planned, and how to conclusively identify apatite compounds. *Biomed Res. Int.* 2013, (2013).

44. Elliott, J. C. *Studies in Inorganic Chemistry: Structure and Chemistry of the Apatites and Other Calcium Orthophosphates*. (Elsevier Science B.V, 1994).

45. Harding, I. S., Rashid, N. & Hing, K. a. Surface charge and the effect of excess calcium ions on the hydroxyapatite surface. *Biomaterials* 26, 6818–6826 (2005).

46. Almora Barrios, N. A computational investigation of the interaction of the collagen molecule with hydroxyapatite. (2010). at <http://eprints.ucl.ac.uk/19313/>[[Last accessed on 13.07.2015]

47. Sakhno, Y. *et al.* Surface hydration and cationic sites of nanohydroxyapatites with amorphous or crystalline surfaces: A comparative study. *J. Phys. Chem. C* 114, 16640–16648 (2010).

48. Bertinetti, L. *et al.* Surface Structure , Hydration , and Cationic Sites of Nanohydroxyapatite : UHR-TEM , IR , and Microgravimetric Studies. *J. Phys. Chem. C* 4027–4035 (2007).

49. Jäger, C., Welzel, T., Meyer-Zaika, W. & Epple, M. A solid-state NMR investigation of the structure of nanocrystalline hydroxyapatite. *Magn. Reson. Chem.* 44, 573–580 (2006).

50. Mourino, V., Cattalini, J. P. & Boccaccini, a. R. Metallic ions as therapeutic agents in tissue engineering scaffolds: an overview of their biological applications and strategies for new developments. *J. R. Soc. Interface* 9, 401–419 (2012).

51. Gielen, M. & Tiekink, E. *Metallotherapeutic drugs and metal-based diagnostic agents: the use of metals in medicine*. (Wiley & Sons, 2005).

52. Habibovic, P. & Barralet, J. E. Bioinorganics and biomaterials: Bone repair. *Acta Biomater.* 7, 3013–3026 (2011).

53. Price, C. T., Koval, K. J. & Langford, J. R. Silicon: A review of its potential role in the prevention and treatment of postmenopausal osteoporosis. *Int. J. Endocrinol.* 2013, (2013).

54. Patel, N. *et al.* A comparative study on the in vivo behavior of hydroxyapatite and silicon substituted hydroxyapatite granules. *J. Mater. Sci. Mater. Med.* 13, 1199–1206 (2002).

55. Porter, a. E., Patel, N., Skepper, J. N., Best, S. M. & Bonfield, W. Comparison of in vivo dissolution processes in hydroxyapatite and silicon-substituted hydroxyapatite bioceramics. *Biomaterials* 24, 4609–4620 (2003).

56. Dahl, S. G. *et al.* Incorporation and distribution of strontium in bone. *Bone* 28, 446–453 (2001).

57. Terra, J. *et al.* The structure of strontium-doped hydroxyapatite: an experimental and theoretical study. *Phys. Chem. Chem. Phys.* 11, 568–577 (2009).

58. Cazalbou, S. *et al.* Ion exchanges in apatites for biomedical application. *J. Mater. Sci. Mater. Med.* 16, 405–409 (2005).

59. Capuccini, C. *et al.* Interaction of Sr-doped hydroxy apatite nanocrystals with osteoclast and osteoblast-like cells. *J. Biomed. Mater. Res. - Part A* 89, 594–600 (2009).

60. Landi, E. *et al.* Biomimetic Mg-substituted hydroxyapatite: From synthesis to in vivo behaviour. *J. Mater. Sci. Mater. Med.* 19, 239–247 (2008).

61. Kawamura, H. *et al.* Stimulatory effect of zinc-releasing calcium phosphate implant on bone formation in rabbit femora. *J. Biomed. Mater. Res.* 50, 184–190 (2000).

62. Liau, S. Y., Read, D. C., Pugh, W. J., Furr, J. R. A. & Russell, D. Interaction of silver nitrate with readily identifiable groups: relationship to the antibacterial action of silver ions. *Lett. Appl. Microbiol.* 25, 279–283 (1997).

63. Kolmas, J., Groszyk, E. & Kwiatkowska-Rózycka, D. Substituted hydroxyapatites with antibacterial properties. *Biomed Res. Int.* 2014, (2014).

64. S, S., SM, H., M, T. & HR, R. In vitro antibacterial evaluation of sol-gel-derived Zn-, Ag-, and (Zn + Ag)-doped hydroxyapatite coatings against methicillin-resistant Staphylococcus aureus. *J Biomed Mater Res A.* 101, 222–30 (2013).

65. Fielding, G. A., Roy, M., Bandyopadhyay, A. & Bose, S. Antibacterial and biological characteristics of plasma sprayed silver and strontium doped hydroxyapatite coatings. *Acta Biomater.* 8, 3144–3152 (2012).

66. Stanić, V. *et al.* Synthesis, characterization and antimicrobial activity of copper and zinc-doped hydroxyapatite nanopowders. *Appl. Surf. Sci.* 256, 6083–6089 (2010).

67. Brozmanová, J., Mániková, D., Vlčková, V. & Chovanec, M. Selenium: A double-edged sword for defense and offence in cancer. *Arch. Toxicol.* 84, 919–938 (2010).

68. Rayman, M. P. The importance of selenium to human health. *Lancet* 356, 233–241 (2000).

69. Whanger, P. D. Selenium and its relationship to cancer: an update. *Br. J. Nutr.* 91, 11–28 (2004).

70. Baile, C. a & Science, D. Dietary Selenium Repletion May Reduce Cancer Incidence in People at High Risk Who Live in Areas with Low Soil Selenium. *Nutr. Rev.* 55, 277–286 (1997).

71. Zeng, H., Cao, J. J. & Combs, G. F. Selenium in bone health: Roles in antioxidant protection and cell proliferation. *Nutrients* 5, 97–110 (2013).

72. Tran, P. a., Sarin, L., Hurt, R. H. & Webster, T. J. Differential effects of nanoselenium doping on healthy and cancerous osteoblasts in coculture on titanium. *Int. J. Nanomedicine* 5, 351–358 (2010).

73. Wang, Y. *et al.* Dual functional selenium-substituted hydroxyapatite. *Interface Focus* 2, 378–386 (2012).

74. Kolmas, J., Oledzka, E., Sobczak, M. & Nałęcz-Jawecki, G. Nanocrystalline hydroxyapatite doped with selenium oxyanions: A new material for potential biomedical applications. *Mater. Sci. Eng. C* 39, 134–142 (2014).

75. Larson, a C. & Von Dreele, R. B. General Structure Analysis System (GSAS). *Structure* 748, 86–748 (2004).

76. Toby, B. H. & Von Dreele, R. B. 'GSAS-II: The Genesis of a Modern Open-Source All-Purpose Crystallography Software Package'. *J. Appl. Cryst.* 46, 544–549 (2013).

77. Sudarsanan, K. & Young, R. a. Significant precision in crystal structural details. Holly Springs hydroxyapatite. *Acta Crystallogr. Sect. B Struct. Crystallogr. Cryst. Chem.* 25, 1534–1543 (1969).

78. Wilson, R. M., Elliott, J. C., Dowker, S. E. P. & Smith, R. I. Rietveld structure refinement of precipitated carbonate apatite using neutron diffraction data. *Biomaterials* 25, 2205–2213 (2004).

79. Monteil-Rivera, F. *et al.* Sorption of Selenite (SeO(3)(2-)) on Hydroxyapatite: An Exchange Process. *J. Colloid Interface Sci.* 221, 291–300 (2000).

80. Dorozhkin, S. V. Nanosized and nanocrystalline calcium orthophosphates. *Acta Biomater.* 6, 715–734 (2010).

81. Wang, S. L., Johnston, C. T., Bish, D. L., White, J. L. & Hem, S. L. Water-vapor adsorption and surface area measurement of poorly crystalline boehmite. *J. Colloid Interface Sci.* 260, 26–35 (2003).

82. Ji, S., Jiang, T., Xu, K. & Li, S. FTIR study of the adsorption of water on ultradispersed diamond powder surface. *Appl. Surf. Sci.* 133, 231–238 (1998).

83. Berzina-Cimdina, L. & Borodajenko, N. Research of Calcium Phosphates Using Fourier Transform Infrared Spectroscopy. *Infrared Spectrosc. – Mater. Sci. Eng. Technol.* 123–148 (2012). doi:10.5772/36942

84. Lefèvre, G. In situ Fourier-transform infrared spectroscopy studies of inorganic ions adsorption on metal oxides and hydroxides. *Adv. Colloid Interface Sci.* 107, 109–123 (2004).

85. Su, C. & Suarez, D. L. IN SITU I N F R A R E D SPECIATION OF A D S O R B E D C A R B O N A T E O N A L U M I N U M A N D IRON OXIDES. 814–825 (1997).

86. Smolen, D. *et al.* Highly biocompatible, nanocrystalline hydroxyapatite synthesized in a solvothermal process driven by high energy density microwave radiation. *Int. J. Nanomedicine* 8, 653–668 (2013).

87. Featherstone, J. D. B., Pearson, S. & Legeros, R. Z. An Infrared Method for Quantification of Carbonate in Carbonated Apatites. *Caries Res.* 18, 63–66 (1984).

88. Smidt, E., Böhm, K. & Schwanninger, M. The application of FT-IR spectroscopy in waste management. *Fourier Transform. - New Anal. Approaches FTIR Strateg.* 405–430 (2011). doi:10.5772/15998

89. Reigner, P., Lasaga, A., Berner, R., Han, O. & Zilm, K. Mechanism of CO 2- 3 substitution in carbonate-fluorapatite: evidence from FTIR spectroscopy, 13C NMR, and quantum mechanical calculations. *Am. Miner.* 79, 809–818 (1994).

90. Rehman, I. & Bonfield, W. Characterization of hydroxyapatite and carbonated apatite by photo acoustic FTIR spectroscopy. *J. Mater. Sci. Mater. Med.* 8, 1–4 (1997).

91. Ebert, M. & Havlíček, D. Magnesium selenites. 34, (1980).

92. Su, C. & Suarez, D. L. Selenate and Selenite Sorption on Iron Oxides. *Soil Sci. Soc. Am. J.* 64, 101 (2000).

93. Moulder, J. F., Stickle, W. F., Sobol, P. E. & Bomben, K. D. Handbool of X-ray Photoelectron Spectroscopy. 255 (1995).

94. Sasaki, K., Blowes, D. W. & Ptacek, C. J. Spectroscopic study of precipitates formed during removal of selenium from mine drainage spiked with selenate using permeable reactive materials. *Geochem. J.* 42, 283–294 (2008).

95. Duc, M. *et al.* Sorption of selenium anionic species on apatites and iron oxides from aqueous solutions. *J. Environ. Radioact.* 70, 61–72 (2003).

96. Duc, M., Lefèvre, G. & Fédoroff, M. Sorption of selenite ions on hematite. *J. Colloid Interface Sci.* 298, 556–563 (2006).

97. Rovira, M. *et al.* Sorption of selenium(IV) and selenium(VI) onto natural iron oxides: Goethite and hematite. *J. Hazard. Mater.* 150, 279–284 (2008).

98. Lu, H. B., Campbell, C. T., Graham, D. J. & Ratner, B. D. Surface characterization of hydroxyapatite and related calcium phosphates by XPS and TOF-SIMS. *Anal. Chem.* 72, 2886–2894 (2000).

99. Sutton, L. . Tables Of Interatomic Distances Supplement. M20 (1965).

100. Fleet, M. E. & Liu, X. Location of type B carbonate ion in type A-B carbonate apatite synthesized at high pressure. *J. Solid State Chem.* 177, 3174–3182 (2004).

101. Mereiter, K. Sodium selenite pentahydrate, Na 2 SeO 3 ·5H 2 O. *Acta Crystallogr. Sect. E Struct. Reports Online* 69, i77–i78 (2013).

102. Chubar, N. EXAFS and FTIR studies of selenite and selenate sorption by alkoxide-free sol–gel generated Mg–Al–CO 3 layered double hydroxide with very labile interlayer anions. *J. Mater. Chem. A* 2, 15995–16007 (2014).

103. LeGeros, R. Z. Effect of carbonate on the lattice parameters of hydroxyapatite. *Nature* 206, 403–404 (1965).

104. Fleet, M. E., Liu, X. & King, P. L. Accommodation of the carbonate ion in apatite: An FTIR and X-ray structure study of crystals synthesized at 2-4 GPa. *Am. Mineral.* 89, 1422–1432 (2004).

105. Fortes, a. D. & Gutmann, M. J. Crystal structure of magnesium selenate heptahydrate, MgSeO 4 ·7H 2 O, from neutron time-of-flight data. *Acta Crystallogr. Sect. E Struct. Reports Online* 70, 134–137 (2014).